Mixed approach for coupled flow and mechanics in a fractured medium

Author: Sólveig Halldóra Stefánsdóttir

Supervisors: Kundan Kumar & Omar Duran

Master thesis in Applied and Computational Mathematics,
Institute of Mathematics,
University of Bergen,
June 2023

Acknowledgements

First and foremost, I want to thank my two supervisors, Kundan Kumar and Omar Duran. Kundan's suggestion of the topic and expertise in analysis have provided me with a solid foundation for this thesis. His insightful feedback and guidance throughout the process have been invaluable. I am also deeply grateful to Omar for his invaluable assistance with the numerical aspects of this thesis. His expertise and willingness to help, even during weekends, have been crucial for me to overcome various challenges. I am beyond grateful for their dedication and mentorship.

I would like to thank the PorePy group for welcoming me into their team and their assistance in overcoming various challenges. Additionally, a special thanks goes to my neighbor, Barbara Wasson, for her kind assistance in proofreading and improving the English writing in my thesis. I would also like to extend my heartfelt thanks to my fellow students for the engaging lunchtime discussions and unforgettable memories that have truly made the past five years enjoyable.

To my family and my better half, Espen, I am deeply grateful for their belief in me. Their love, encouragement, and patience have been invaluable in balancing both my studies and my passion for playing handball. I am truly grateful for their constant support and understanding, as they have been the driving force behind my progress.

Sólveig Halldóra Stefánsdóttir
Bergen, June 2023

Abstract

This thesis presents a mixed finite element method of the Biot system of poroelasticity within a reservoir, coupled with a mixed formulation of flow within a fracture. The fracture is represented as a planar object of one dimension less than the domain of the reservoir. The spatial discretization is combined by a multipoint stress mixed finite element (MSMFE) method for elasticity and the multipoint flux mixed finite element (MFMFE) method for the Darcy flow within the reservoir matrix, coupled with a MFMFE method for the flow within the fracture. In the reservoir matrix, the lowest order Brezzi-Douglas-Marini mixed finite element spaces for the poroelastic stress and Darcy velocity, along with piecewise constant displacement, pressure and rotation are considered. Within the fracture, we consider compatible pairs of element spaces for the fracture pressure and flux, along with piecewise constant mortar displacement. A stability analysis is performed on both the continuous and semi-discrete problem. Furthermore, existence and uniqueness are shown for the semi-discrete and fully-discrete solutions. Different numerical simulations are presented in the end.

Keywords: Poroelasticity · Biot model · Mixed finite elements · Fractured poroelastic medium · Multipoint stress · Multipoint flux

Sammendrag

Denne avhandlingen presenterer en blandet endelig element metode for Biot ligningene for poroelastisitet i et reservoar, sammenkoblet med en blandet formulering av strømning innenfor en sprekk. Sprekken er representert som et flatt objekt av en dimensjon mindre enn domenet til reservoaret. Den romlige diskretiseringen kombinerer en flerpunkts spenning blandet endelig element (MSMFE) metode for elastisitet og en flerpunkts fluks blandet endelig element (MFMFE) metode for Darcy-strømningen innenfor reservoarmatrisen, sammenkoblet med en MFMFE-metode for strømningen innenfor sprekken. I reservoarmatrisen tar vi i betraktning laveste grad Brezzi-Douglas-Marini blandede endelig elementrom for poroelastisk spenning og Darcy-strømning, og stykkevis konstant forskyvning, trykk og rotasjon. Innenfor sprekken betrakter vi de endelige rommene av sprekk-trykket og fluksen til å være to kompatible par, sammen med konstant mørtelforskyvning. En stabilitetsanalyse utføres både for det kontinuerlige og semi-diskrete problemet. Videre vises eksistens og entydighet for de semi-diskrete og fullt-diskrete løsningene. Ulike numeriske simulasjoner er presentert på slutten.

Nøkkelord: Poroelastisitet · Biot ligningene · Blandede endelig elementer · Brukket poroelastistisk medium · Flerpunkts spenning · Flerpunkts fluks

Contents

List of symbols

The symbols in this thesis, together with their respective units are shown in the table below. Symbols in bold letter will represent vectors and tensors.

In this work, ∇ denotes the gradient operator, $\nabla\cdot$ the divergence operator and $\nabla\times$ the curl. The Laplace operator will be denoted Δ, where $\Delta(\cdot) = \nabla \cdot \nabla(\cdot)$. For a variable x, we will have $\frac{\partial}{\partial x} = \partial_x$.

The subscript f will be used for variables concerning the fluid and c for variables within the fracture. The subscript h and superscript n will denote the spatial level and the time level, respectively. The subscript 0 is used to specify a starting value or a reference value for a variable.

Greek letters

α	Biot-Willis coefficient	–
$\boldsymbol{\epsilon}(\cdot)$	Linear strain tensor	–
$\boldsymbol{\kappa}$	Hydraulic conductivity of the medium	$\mathrm{m\,s^{-1}}$
$\boldsymbol{\sigma}$	Poroelastic Cauchy stress tensor	Pa
$\boldsymbol{\sigma}_e$	Linear stress tensor	Pa
χ	Mortar displacement	m
η	Vertical distance	m
γ	Lagrange multiplier for rotation	–
λ	First Lamé parameter	Pa
μ	Second Lamé parameter	Pa
μ_f	Dynamic viscosity	$\mathrm{Pa\,s}$

ν	Poisson ratio	–
ν_f	Kinematic viscosity	$\mathrm{m^2\,s^{-1}}$
Ω	Matrix domain	–
ϕ	Porosity of the medium	–
ϕ^*	Fluid volume content	–
ψ	Source term	$\mathrm{kg\,m^{-3}\,s^{-1}}$
ρ_f	Fluid density	$\mathrm{kg\,m^{-3}}$
ρ_r	Reference density	$\mathrm{kg\,m^{-3}}$

Roman letters

$\boldsymbol{f}$	Body force	$\mathrm{N\,m^{-3}}$
$\boldsymbol{g}$	Gravitational acceleration vector	$\mathrm{m\,s^{-2}}$
$\boldsymbol{k}$	The permeability of the medium	$\mathrm{m^2}$
$\boldsymbol{q}$	Volumetric flux	$\mathrm{m\,s^{-1}}$
$\boldsymbol{u}$	Displacement	m
$\mathbf{w_n}$	Outward normal vector	–
$\mathcal{C}$	Fracture domain	–
$\mathbf{F}$	Mass flux vector	$\mathrm{kg\,m^{-2}\,s^{-1}}$
c_0	Mass storativity	–
c_f	Fluid compressibility	$\mathrm{Pa^{-1}}$
E	Young's modulus	Pa
f_1	Body force	$\mathrm{N\,m^{-3}}$
f_2	Source term	$\mathrm{kg\,m^{-3}\,s^{-1}}$
h	Mesh size	–
h_f	Hydraulic head	m
K_s	Bulk modulus	Pa

K_{nc}	Normal permeability in fracture	m^2
K_{tc}	Tangential permeability in fracture	m^2
M	Biot modulus	Pa
p	Fluid pressure	Pa
p_c	Pressure in the fracture	Pa
q_c	Flux in fracture	$\mathrm{m\,s^{-1}}$
q_d	Darcy's flux	$\mathrm{m^3\,s^{-1}}$
q_L	Unknown leakage	$\mathrm{kg\,m^{-3}\,s^{-1}}$
q_W	Known injection	$\mathrm{kg\,m^{-3}\,s^{-1}}$
T	Final time	s
t	Time	s
z	Height over datum	m

List of figures

List of tables

Introduction

Already in 1510, with his collection of scientific writing Codex Leicester [da Vinci, 1510], Leonardo da Vinci compared the Earth to the human body. He compared soils and rocks to the flesh and bones. What these materials have in common is that they are porous mediums, a solid material containing pores, allowing fluid in different phases to flow through the material. The interaction between this fluid flow and the deformation of the solid is called poroelasticity. In the past years there has been a growing interest in the field of porous media, where coupling of geomechanics and flow in a poroelastic medium has had many important applications in different areas. Some examples are geothermal heat extraction, modelling of the brain and CO_2-storage.

> *"The Earth is a living body. Its soul is its ability to grow. This soul, which also provides the Earth with its bodily warmth, is located in the inner fires of the Earth, which emerge at several places as baths, sulfur mines or volcanoes. Its flesh is the soil, its bones are the strata of rock, its cartilage is the tufa, its blood is the underground streams, the reservoir of blood around its heart is the ocean, the systole and diastole of the blood in the arteries and veins appear on the Earth as the rising and sinking of the oceans."*
>
> Leonardo da Vinci, Codex Leicester (1506-1510)

In recent years, there has been a drastic increase of the amount of carbon dioxide in the air. According to [Friedlingstein et al., 2022], carbon dioxide emissions averaged 35 gigatons per year (Gt CO_2/year) between 2010 and 2020, compared to just 11 Gt CO_2/year in the 1960s. The increase in the amount of greenhouse gas (GHG) emissions, including CO_2, have led to 2022 being identified as the sixth warmest year on record since 1880, as reported by NOAA [NOAA, 2023]. The emission of GHG has had an undesirable consequence on the environment, health, and the economy. A number of these negative effects might be more intense weather extremes, sea-level rise, more respiratory disease caused by smog, and disruption in the food supply chain [Ervik, 2020].

Injection of CO_2 is a potential pathway to decrease the amount of the world's carbon dioxide emission. From the early 1970s the injection of carbon dioxide into subsurface formations has been adopted more and more. In the beginning the purpose of carbon dioxide injection was to increase the oil production rather then for environmental benefits, but in later years it has been seen as an option to reduce the amount of GHG emission [Nordbotten and Celia, 2012].

In carbon capture, storage, and utilization (CCSU) the existence of fractures in a poroelastic medium will affect flow and transport through the medium [Berre et al., 2019]. Therefore, it is important to study coupled flow and geomechanics in a fractured poroelastic medium, as the fractures can have a significant effect on how CO_2 escapes into the atmosphere. Coupled geomechanics and flow problems, both with and without fractures, has been widely studied since the work of K. Terzaghi [Terzaghi and Peck, 1948] and M.A Biot [Biot, 1972, Biot, 1941]. The fractures are the vulnerable regions for mechanical instability. Injection of fluid, such as CO_2, at high pressure may lead to changes in the in-situ stress conditions, potentially resulting in seismic events. It is therefore important to monitor the changes in stress conditions due to the fluid injection [Birkholzer et al., 2009, Cappa, 2011, Castonguay et al., 2013]. Similarly, other subsurface applications, including thermal and hydraulic storage, will have the same challenges. For these reasons, coupled flow and mechanics in a fractured subsurface has attracted attention from the research community [Franceschini et al., 2020, Jha and Juanes, 2014, Stefansson et al., 2020].

In this thesis the quasi-static, linear Biot model, which describes flow in a deformable porous medium, is considered within the reservoir matrix. The flow of the fluid within the fractures embedded in the medium will be described by a lubrication equation. There is a large literature on the numerical solution to the Biot system, where finite difference, finite volume, and finite element methods all have been studied. Schemes for the two-field displacement-pressure formulation have been studied in [Gaspar et al., 2003, Nordbotten, 2016, Murad and Loula, 1992]. A three-field displacement-pressure-Darcy velocity formulation has been studied in [Phillips and Wheeler, 2007, Hu et al., 2017, Phillips and Wheeler, 2008]. Furthermore, fully mixed formulations of the Biot system have been studied in the past few years, where in [Yi, 2014] a five-field stress-displacement-rotation mixed formulation coupled with a velocity-pressure mixed Darcy model is considered. In [Ambartsumyan et al., 2020b], a new fully mixed finite element method for the quasi-static, Biot system of poroelasticity was developed, where they coupled the already developed multipoint stress mixed finite element (MSMFE) method for elasticity [Ambartsumyan et al., 2020a, Ambartsumyan et al., 2021] with weak stress symmetry, and the multipoint flux mixed finite element (MFMFE) method for Darcy flow [Wheeler and Yotov, 2006]. The development of the MSMFE method was motivated by the finite volume multipoint stress approximation (MPSA), whereas the MFMFE method is closely related to the multipoint flux approximation (MPFA) method. These methods have been studied in [Aavatsmark, 2002, Nordbotten and Keilegavlen, 2021].

There are both advantages and disadvantages of such fully mixed approximations. For instance, in the Galerkin finite element method, a phenomenon known as locking occurs in poroelasticity. This phenomenon results in unstable and oscillatory numerical behavior of the pore pressure [Yi, 2014], particularly when the Lamé parameter λ approaches infinity [Yi, 2017]. Fully mixed approximations provide locking-free behaviour. Other advantages are accurate stress and velocity approximations, local mass and momentum conservation, and robustness with respect to the physical parameters [Ambartsumyan et al., 2020b]. Moreover, these fully mixed approximations can handle discontinuous full tensor permeabilites and Lamé coefficients. A drawback of these fully mixed formulations is that they result in large algebraic systems of saddle point type at each time step. In [Ambartsumyan et al., 2020b] they develop a fully mixed method that can be reduced to a positive cell-centered displacement-pressure system, resulting in a method that have all the advantages of fully mixed finite element method, with a significantly reduced computational cost.

In the research a coupled MSMFE-MFMFE method for the Biot system of poroelasticity within the reservoir matrix, coupled with a MFMFE method for the flow within the fracture has been developed. The approach is inspired by the MSMFE-MFMFE method from [Ambartsumyan et al., 2020b] coupled with the mixed formulation for the fracture flow in [Girault et al., 2018]. A mixed variational formulation of our poroelastic system with a fracture embedded in the medium will be derived. Additionally, stability analysis on our coupled mixed variational formulation will be performed, employing the classical Babuška-Brezzi conditions. Furthermore, the semi-discrete scheme will be presented, in which we utilize the lowest order Brezzi-Douglas-Marini spaces for stress and Darcy flow within the reservoir matrix. Additionally, we employ piecewise constant displacement, rotation, and pressure. Existence and uniqueness of the semi-discrete solution will be proven, and stability analysis will be performed. The fully-discrete scheme, based on backward Euler in time discretization, will be presented and the existence and uniqueness of the fully-discrete solution will be proved.

Outline

After this introduction, the thesis is organized as follows:

Chapter 1: Gives an introduction to flow in porous media. First, the main properties of both the porous media and the fluid flowing through it are introduced. The Darcy law and the mass conservation equation are mentioned, before a discussion of fractures in a porous media.

Chapter 2: Covers numerical approximation techniques. It begins with an introduction of the finite element method. The conformal variational formulation is introduced, with an example. The Galerkin finite element is discussed, before the mixed variational formulation is introduced. The chapter ends with an introduction to the MPFA and MPSA methods.

Chapter 3: Introduction to our mathematical model. The derivation of the equations within the reservoir matrix can be found in Section 3.1, while the equations within the fracture are derived in Section 3.2. In the end, the complete model problem is given on the mixed form.

Chapter 4: Begins by giving an introduction to general spaces and notation. The variational formulation of our complete model problem is derived and stability analysis on the continuous case is performed.

Chapter 5: The semi-discrete method is developed, with the reservoir matrix using the lowest order Brezzi-Douglas-Marini spaces for the stress and the Darcy flow, and piecewise constant displacement, rotation and pressure. The existence and uniqueness for the semi-discrete scheme is proven. The chapter ends with a presentation of a stability analysis of the semi-discrete scheme.

Chapter 6: Is devoted to the fully-discrete method. The backward Euler in time method is derived in Section 6.1 and the existence and uniqueness of the fully-discrete scheme is proven in Section 6.3.

Chapter 7: Present numerical solutions. The chapter begins with a presentation of code verification, showing convergence rates for the displacement, pressure, stress, and flux. Furthermore, three different simulations that were studied are presented. First, a single tilted fracture in a homogeneous medium, followed by many fractures in a homogeneous medium. In the end a study of a layered medium is presented and the effect of a fracture network in the different layers is discussed.

Contributions

The contributions of this thesis are as follows:

- The development of a coupled MSMFE-MFMFE method for the Biot system of poroelasticity coupled with a MFMFE method for the flow within a fracture.
- A stability analysis on the continuous and the semi-discrete problem.
- Existence and uniqueness proofs for both the semi-discrete and fully-discrete scheme.

Chapter 1

Flow in porous media

In this chapter, the general theory of flow in porous media is presented. The properties of both the medium and the fluid are covered first, followed by a short introduction of Darcy's law and the conservation of mass. The chapter concludes with a discussion on fractures in a porous medium. The theory is based on [Nordbotten and Celia, 2012] and on literature from the course on porous media at the University of Bergen [Radu, 2021]. For further details we refer to standard textbooks such as [Bear, 1988].

1.1 Characteristics of a porous medium

A porous medium is defined as a solid material, the matrix, containing pores in between, the pore space. Porous media flow refers to the flow inside a porous medium, where the pores can be filled with one or more fluids. A flow consisting of only one fluid through a porous medium is called single phase flow, say water. Two-phase flow is referred to as a flow through a medium with two fluids, for example CO_2 and water. In this thesis we will only consider single phase flow.

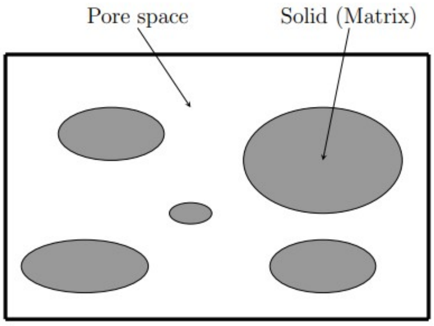

Figure 1.1: An illustration of a porous medium.

Figure 1.1, inspired by [Skoglund, 2019], shows an illustration of a porous medium where the white area illustrates the pore space and the grey area the matrix. Various examples of such mediums are soils, the brain, or even something as simple as sponges. These different porous media have different conditions. To discuss the different conditions of the medium a volume around a point in space, called representative elementary volume, REV, is defined. The REV is large enough so that it always contains the properties of both the pore space and the matrix, but is small enough so that the variations of the parameter from one domain to the next may be approximated by continuous functions.

Porosity, typically represented by the symbol ϕ, is an important concept in the porous media field. It is an indicator of how much void space a material contains and is calculated by dividing the volume of pore space in the REV by the total volume of the REV:

$$\phi = \frac{\text{volume of pore space in REV}}{\text{volume of REV}}$$

Some examples of values of porosities, according to [Huinink, 2016], are the porosity of sand between 0.25-0.50 and fractured basalt between 0.05-0.50.

The permeability of a porous medium is another important quantity, representing how easy a fluid can flow through the material. Higher values of permeability indicate that fluids flow more easily through the medium [Nishiyama and Yokoyama, 2017]. The permeability is given either as a scalar or as a tensor, denoted as $\mathbb{R}^{d,d}$, where d is the dimension. This is a result of that a fluid may flow easier in one direction than another, for example in a layered system [Radu, 2021]. It should be noted that porosity has a strong correlation with permeability, however, the permeability is not necessarily proportional to the porosity. In addition to porosity, pores are also interconnected, affecting the permeability [Aarnes et al., 2007].

1.2 Characteristics of the fluid

In a porous medium the pore space can be filled with one or more fluids, resulting in either a single-phase flow or a multi-phase flow. These fluids have different properties. The first property is the fluid density, denoted ρ_f. Fluid density is defined as the mass per unit volume and generally depends on both pressure and temperature [Radu, 2021]. In situations where the fluid density is not constant, the concept of fluid compressibility, denoted as c_f, is introduced to ensure a solvable system.

A possible model of the fluid compressibility is described as follows:

$$c_f = \frac{1}{\rho_f}\frac{d\rho_f}{dp}$$

Another important property of the fluid is the viscosity, denoted μ_f. The viscosity describes the fluid's resistance to flow, where a lower value signifies fluids that flow more easily than fluids with higher values. This quantity is usually dependent on the temperature, where an increase in temperature results in a decrease of the viscosity [Jennings et al., 1997]. In our research we will maintain a constant viscosity for convenience.

1.3 Darcy's law

Darcy's law provides an explanation of fluid flow through a porous medium. Based on his experiments, Henry Darcy observed that the volumetric flow rate is directly proportional to the difference in heights, denoted as $h_{f,1}$ and $h_{f,2}$, and the cross-sectional area, while inversely proportional to the length [Nordbotten and Celia, 2012]. By introducing the proportionality constant κ, known as the hydraulic conductivity of the medium, the Darcy experiment can be formulated as follows:

$$q_d = -\kappa\frac{A(h_{f,2} - h_{f,1})}{l} \tag{1.1}$$

Extending to three dimensions and defining the volumetric flux, denoted as $\boldsymbol{q}$, as the flow rate per unit area of the medium, the differential form of Darcy's law is obtained by taking the limit as l approaches zero:

$$\boldsymbol{q} = -\boldsymbol{\kappa}\nabla h_f \tag{1.2}$$

In the equation, $\boldsymbol{\kappa}$ represents the hydraulic conductivity tensor, and h_f denotes the hydraulic head. In general, Darcy's law states that fluid within a porous medium flows from regions with higher values of h_f to those with lower values of h_f [Nordbotten and Celia, 2012]. Additionally, Darcy discovered that the hydraulic conductivity, κ, is dependent on the permeability of the medium. The hydraulic conductivity is expressed as a function of permeability $\boldsymbol{k}$, fluid density ρ_f, viscosity μ_f, and gravity g in the following expression:

$$\boldsymbol{\kappa} = \frac{\boldsymbol{k}\rho_f g}{\mu_f} \tag{1.3}$$

To get a deeper understanding of Darcy's law look at the illustration in Figure 1.2, inspired by [Nordbotten and Celia, 2012]. Here a tube is filled with sand (yellow) and two manometers are filled with water (blue).

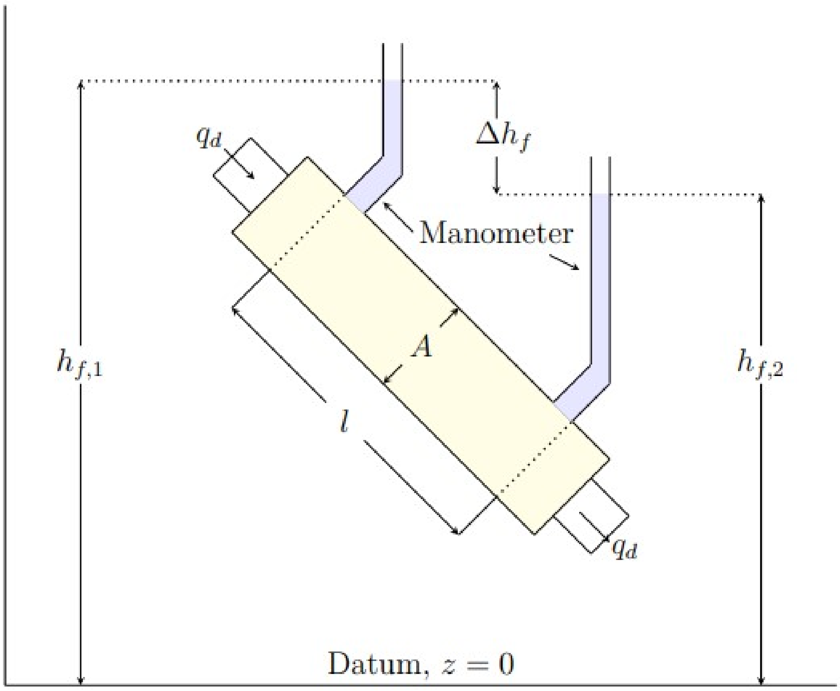

Figure 1.2: An illustration of Darcy's experiment.

Under the assumption of hydrostatic equilibrium, the external gravitational force acting on a fluid is balanced by the gradient force, resulting in the following expression for pressure in the manometer:

$$p_{abs} = p_{atm} + \rho_f g (h_f - z) \tag{1.4}$$

By introducing the gauge pressure, $p = p_{\text{abs}} - p_{\text{atm}}$, in the above equation, the result is the following expression for the hydraulic head:

$$h_f = \frac{p}{\rho_f g} + z \tag{1.5}$$

By incorporating the expressions for hydraulic head and hydraulic conductivity into the differential form of Darcy's law, and considering the gravity vector as $\boldsymbol{g} = -g\boldsymbol{e_z}$, Darcy's equation can be formulated as follows:

$$\boldsymbol{q} = -\frac{\boldsymbol{k}}{\mu_f}(\nabla p - \rho_f \boldsymbol{g}) \tag{1.6}$$

1.4 Conservation of mass

From Darcy's equation it is evident that the pressure, p, is an unknown quantity, as is the flow rate per area, u. Darcy's equation itself is insufficient to solve a flow problem as it does not close the system; another equation is needed to describe the flow through a porous medium. This can be achieved by introducing the principle of mass conservation, which ensures that mass is a conserved quantity that cannot be formed or destroyed.

The principle of mass conservation is based on the concept that the change of mass within a domain, Ω, is equivalent to the mass flowing across the boundaries, in addition to any mass introduced or removed through internal sources or sinks [Nordbotten and Celia, 2012]. This is illustrated with Figure 1.3, inspired by [Skoglund, 2019], where mass is flowing through the boundaries and a source/sink term within the domain. Note, however, that the figure only shows mass flowing through the yz-boundaries.

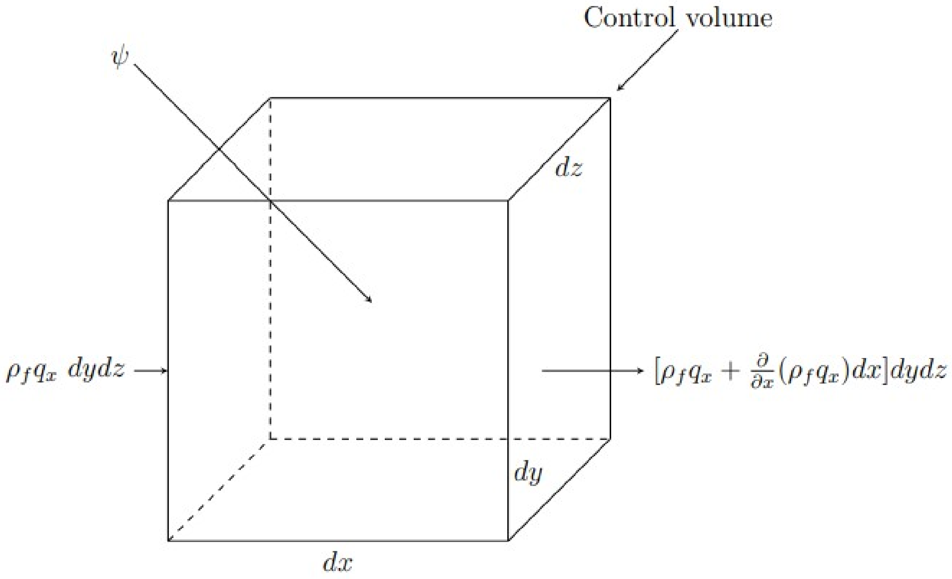

Figure 1.3: A 3D representation of a control volume with fluid and mass fluxes.

By considering a differential volume element $dV = dxdydz$ and a subvolume ω such that $\omega \subseteq \Omega$, where Ω represents the domain, the following statement of conservation of mass on the integral form is as follows:

$$\int_{\omega} \frac{\partial m}{\partial t} dV = - \oint_{\partial \omega} \boldsymbol{F} \cdot \boldsymbol{w_n} dA + \int_{\omega} \psi dV \quad \forall \omega \subseteq \Omega \tag{1.7}$$

In the above equation, $\boldsymbol{F}$ is the mass flux vector, $\boldsymbol{w_n}$ the outward pointing normal vector, and ψ represents the sources and sinks. By letting $m = \rho_f \phi$ and $\boldsymbol{F} = \rho_f \boldsymbol{q}$, and by using the divergence theorem on the surface integral, we get:

$$\int_\omega \frac{\partial \rho_f \phi}{\partial t} + \nabla \cdot (\rho_f \boldsymbol{q}) - \psi dV = 0 \tag{1.8}$$

Equation (1.8) must hold for any closed volume ω and hence the integral kernel must be equal to zero as well. Thus the PDE of mass conservation is:

$$\frac{\partial \rho_f \phi}{\partial t} + \nabla \cdot (\rho_f \boldsymbol{q}) = \psi \tag{1.9}$$

1.5 Fractures in a porous medium

In a porous medium there may exist some discontinuities in a form of restricted zones having clearly different characteristics than the rest of the medium. These zones are fractures, $\mathcal{C}$, within the medium. The length of a fracture can span orders of magnitudes and even be comparable to the size of the domain of interest. Compared to their extension, however, the fractures are generally thin, resulting in a small fracture volume as compared to the volume of the surrounding medium [Berre et al., 2019]. As a consequence, the fractures can be approximated to one dimension less than the matrix, giving a mixed-dimensional domain. These fractures can be empty or filled with a fluid or a filling material. In our research we will have flow through the fracture, moreover it is assumed that the fracture does not propagate, meaning that the front of the crack is stationary.

In this research we study a simply connected, bounded domain Ω of $\mathbb{R}^d$, where $d = 2, 3$, with a Lipschitz continuous boundary $\partial\Omega$. In the domain the fractures will be modeled as an interface $\mathcal{C} \subset \Omega$. The fracture $\mathcal{C}$ is a closed subset of Ω. When $d = 2$, the fracture will be represented by a planar object from $\boldsymbol{a}$ to $\boldsymbol{b}$. The fracture will be represented by a planar surface when $d = 3$.

Figure 1.4, inspired by [Varela et al., 2022], illustrates an one dimensional fracture embedded in a two dimensional domain. The domain is represented by a unit square $Y \subset \mathbb{R}^2$ that is decomposed into a fracture $\mathcal{C}$ (blue) embedded in a 2d matrix Ω. The two sides of the fracture $\mathcal{C}$ are distinguished as $\mathcal{C}^+$ and $\mathcal{C}^-$. A superscript $\star$ is used to denote either $+$ or $-$. The part $\Omega^\star$ denotes the part of Ω that is adjacent to $\mathcal{C}^\star$. The normal vector to $\mathcal{C}$, exterior to $\Omega^\star$, is denoted as $\boldsymbol{n}^\star$, meaning that in Figure 1.4 $\boldsymbol{n}^+$ would point from the fracture towards Ω^-. Consequently, the normal vectors are related by the following relationship:

$$\boldsymbol{n}^+ = -\boldsymbol{n}^-$$

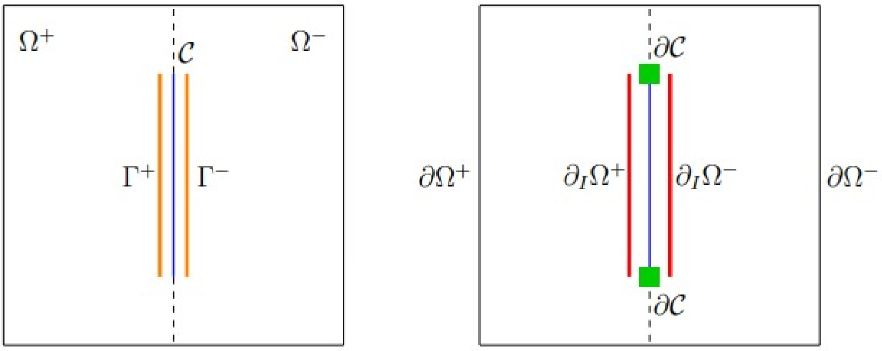

Figure 1.4: A vertical one dimensional fracture embedded in a two dimensional matrix. Left: Subdomains and interfaces. Right: Boundary conditions. Note that $\partial_I\Omega^+$, Γ^+, $\mathcal{C}$, $\partial_I\Omega^-$ and Γ^- all coincide spatially. They are placed in different locations in the figure for illustrative purposes.

The interfaces Γ^+ and Γ^- (depicted in orange) establish the connection between the fracture $\mathcal{C}$ and the reservoir matrix Ω. Spatially, these interfaces, along with the fracture itself, coincide with the internal boundaries $\partial_I\Omega^\star$ (highlighted in red). Furthermore, the fracture has two boundary points (shown in green), where these conditions can either be Dirichlet, Neumann or Robin. At the fracture tips, this thesis consider the Neumann condition.

Chapter 2

Numerical Approximation Techniques

In this chapter the methods used for solving our complete problem statement given by Problem 1 in Section 3.4 are presented. Our aim is to solve the problem over the spatial domain Ω and the time interval $(0, T)$, where T represents the final time. For the spatial discretization, we combine a multipoint stress mixed finite element (MSMFE) method for elasticity and the multipoint flux mixed finite element (MFMFE) method for the Darcy flow in the reservoir, coupled with a MFMFE method for the flow within the fracture.

The chapter begins with an introduction to the finite element method, where the conformal variational formulation and the Galerkin finite element method are introduced. This is followed by a short introduction of the mixed finite element method, as used in the research, where we consider a mixed variational formulation for both the mechanics equation and the flow in the reservoir, as well as a mixed variational formulation for the fracture flow. Finally, an introduction is given to the multipoint flux approximation (MPFA) and multipoint stress approximation (MPSA), as they are closely related to the MFMFE and the MSFME methods, respectively.

2.1 The finite element method

The finite element method is a method used to solve partial differential equations numerically. The method is based on dividing the domain Ω into a finite number of smaller elements and approximating the solution on this discretized domain. First the conformal variational formulation and the Galerkin finite element method are explained, followed by an introduction to the mixed variational formulation, which will be applied for both the mechanics equation and the flow equations in the reservoir, as well as the flow equation in the fracture.

2.1.1 Conformal variational formulation

Using the finite element method, the model problem is expressed in a variational or weak form such that the finite element method can solve the problem numerically. To illustrate the process of formulating a problem as a conformal variational formulation, an example with the Poisson equation is considered. The example is inspired by [Storvik, 2018] and the literature in the course of finite elements at the University of Bergen [Knabner and Angermann, 2003].

Example 1. (The Poisson equation with Dirichlet boundary conditions)
Find u such that:

$$\begin{cases} -\Delta u = f & \text{in } \Omega, \\ u = 0 & \text{on } \partial\Omega \end{cases} \tag{2.1}$$

with Ω being a connected, bounded domain in $\mathbb{R}^n$ having a boundary $\partial\Omega$ and $f \in C(\Omega)$. The Poisson equation is multiplied by a test function v chosen from the given test space:

$$V = \{v \in C_0^\infty(\Omega)\}$$

This leads to the following problem, obtained by integrating over the domain:
Find u such that

$$-\int_\Omega (\Delta u) v dx = \int_\Omega f v dx \quad \forall v \in V$$

By employing Gauss' theorem and integration by parts the problem is reduced to:
Find $u \in V$ such that

$$\int_\Omega \nabla u \cdot \nabla v dx - \int_{\partial\Omega} v(\nabla_{\boldsymbol{n}} u) ds = \int_\Omega f v dx \quad \forall v \in V$$

with $\boldsymbol{n}$ being the outward pointing normal vector. The integral term over the boundaries will vanish as $v = 0$ on the boundary $\partial\Omega$. Thus, the problem can be reformulated as:
Find $u \in V$ such that

$$\int_\Omega \nabla u \cdot \nabla v dx = \int_\Omega f v dx \quad \forall v \in V \tag{2.2}$$

If u solves Equation (2.1) then u will also solve Equation (2.2) as well, however, the converse is not necessarily true, as a solution of Equation (2.2) may require less smoothness compared to a solution of Equation (2.1). Equation (2.2) is known as the variational formulation of the problem. Additionally, the integral in the variational formulation defines an inner product, denoted by $\langle\cdot,\cdot\rangle$, on the space of functions $C^1(\Omega)$. Thus, problem (2.2) can be written as:

$$\langle \nabla u, \nabla v\rangle = \langle f, v\rangle \quad \forall v \in V \tag{2.3}$$

The problem (2.3) can also be expressed as an abstract variational formulation and reads as follows:

$$\text{Find } u \in V \quad \text{such that} \quad a(u,v) = b(v) \quad \forall v \in V \tag{2.4}$$

where $a(\cdot,\cdot)$ is a bilinear form and $b(\cdot)$ is a linear functional. Specifically, for the Poisson problem, the bilinear form is defined as $a(u,v) = \langle \nabla u, \nabla v\rangle$ and the linear functional is defined as $b(v) = \langle f, v\rangle$.

2.1.2 Existence and uniqueness

Before proceeding with solving a partial differential equation (PDE), it is crucial to determine whether a unique solution exists. In this section, two fundamental results, namely the Riesz-Fréchet representation theorem and the Lax-Milgram theorem, which establish the existence and uniqueness of solutions are presented. Before introducing these theorems, some important properties are defined.

Definition 1 ([Knabner and Angermann, 2003] Chapter 2).
Let $a(\cdot,\cdot)$ be a bilinear form on some vector space V,

- *$a(\cdot,\cdot)$ is continuous (or bounded) w.r.t $\|\cdot\|_V$ if there exists a $M > 0$ such that:*

$$|a(u,v)| \le M\|u\|_V\|v\|_V \quad \forall\, u, v \in V \tag{2.5}$$

- *$a(\cdot,\cdot)$ is coercive w.r.t $\|\cdot\|_V$ if there exists an $\alpha > 0$ such that:*

$$a(u,u) \ge \alpha\|u\|_V^2 \tag{2.6}$$

Theorem 2.1.1 ([Cheney, 2001] Chapter 2).
Let Y be the closed subspace of the Hilbert space X, then $X = Y \oplus Y^\perp$, where $Y^\perp$ is the orthogonal complement of Y:

$$Y^\perp = \{x \in X \,:\, \langle x, y\rangle = 0 \textit{ for all } y \in Y\}$$

Theorem 2.1.2 (Riez-Fréchet Representation theorem, [Cheney, 2001] Chapter 2).
For every continuous and linear functional ϕ defined on a Hilbert space X, there exists a unique $v_\phi \in X$ such that:

$$\phi(x) = \langle x, v_\phi\rangle, \quad \forall x \in X$$

Proof. The proof is inspired by the literature in the course of functional analysis at the University of Bergen [Radu, 2022].

To demonstrate the existence, we start by considering a continuous linear functional ϕ in the Hilbert space X, with $Y = \ker(\phi)$.

$$\ker(\phi) = \{x \in X \mid \phi(x) = 0\}.$$

Since ϕ is continuous Y is closed. Moreover, if $Y = X$, then $\phi(x) = 0$ which implies $\phi(x) = \langle x, 0\rangle \, \forall x$. If $Y \neq X$, we can utilize the fact that Y is closed to write $X = Y \oplus Y^{\perp}$ and $Y^{\perp} \neq \{0\}$. We let $u \neq 0$, $u \in Y^{\perp}$ meaning that $\langle y, u\rangle = 0 \, \forall y \in Y$ and $u \notin Y$ giving us $\phi(u) \neq 0$. Then for any $x \in X$ we will have $x - u\frac{\phi(x)}{\phi(u)} \in \ker(\phi) = Y$, resulting in $x = x - u\frac{\phi(x)}{\phi(u)} + u\frac{\phi(x)}{\phi(u)}$ with the first two terms together being in $\ker(\phi) = Y$ and the last in $Y^{\perp}$. Then $X = Y \oplus \langle u\rangle$. Therefore, we can for any $x \in X$ write $x = y + \lambda u$ with $y \in Y$, $\lambda \in \mathbb{C}$. This gives us $\phi(x) = \phi(y) + \lambda\phi(u) = \lambda\phi(u)$.

On the other hand, for $x = y + \lambda u$ we have $\langle x, u\rangle = \langle y, u\rangle + \langle \lambda u, u\rangle = \lambda\|u\|^2$. Thus, we obtain $\phi(x) = \frac{\langle x,u\rangle\phi(u)}{\|u\|^2} = \langle x, \frac{u\overline{\phi(u)}}{\|u\|^2}\rangle$. Therefore, we can choose $v = \frac{u\overline{\phi(u)}}{\|u\|^2}$, and existence follows.

To prove uniqueness, assume that there exists $v_1, v_2 \in X$ such that $\phi(x) = \langle x, v_1\rangle = \langle x, v_2\rangle \, \forall x$. This implies $\langle x, v_1 - v_2\rangle = 0 \, \forall x \in X$ resulting in $v_1 = v_2$.

□

Before introducing and proving the Lax-Milgram theorem, a definition of dual spaces is given and the Banach fixed point theorem is introduced; having these results simplify our proof of the Lax-Milgram theorem.

Definition 2 (Dual space, [Radu, 2022]).
The dual vector space to a real vector space V is the vector space of all linear bounded functionals $f : V \to \mathbb{R}$, denoted V'. The dual norm on V' is given by

$$\|u\|_{V'} = \sup\{\langle u, v\rangle \, : \, v \in V, \, \|u\|_V \leq 1\}$$

Theorem 2.1.3 (Banach fixed point theorem, [Cheney, 2001] Chapter 8).
Let X be a Banach space, $U \subseteq X$ a subset and $f : U \to X$ a function. If

- *U is closed*
- *$f(\cdot)$ is a contraction with a Lipschitz constant $L < 1$*
- *$f[U] \subseteq U$*

Then there exists a unique $x^* \in U$ *such that* $f(x^*) = x^*$*. This* x^* *is called a fixed point.*

Proof. See page 345 in [Cheney, 2001] for proof ☐

Theorem 2.1.4 (Lax-Milgram theorem, [Knabner and Angermann, 2003], Chapter 3)**.**
Let V *be a Hilbert space. Furthermore, let* $a(\cdot,\cdot)$ *be bilinear, continuous and coercive and* $b(\cdot)$ *continuous. Then the variational equation (2.4) has a unique solution* $u \in V$ *such that:*

$$a(u, v) = b(v), \quad \forall v \in V \tag{2.7}$$

Proof. The proof is inspired by [Moholt, 2021]
Based on the assumptions of $a(\cdot,\cdot)$, we define the map $a_u(v) = a(u, v)$, which is a linear continuous functional. According to Riesz-Fréchet representation theorem $a_u(\cdot)$ uniquely determines an element $Au \in V$ such that $a_u(v) = \langle Au, v\rangle$. The map

$$\begin{aligned} A:\, V &\to V \\ w &\mapsto Aw \end{aligned}$$

is both linear and bounded, following from:
Linear:

$$\begin{aligned} \langle A(x+y), v\rangle = \langle Ax, v\rangle + \langle Ax, v\rangle, \quad \forall v \in V \\ \Rightarrow A(x+y) = A(x) + A(y) \end{aligned}$$

Bounded:

$$\|Ax\| = \|a_x\| = \sup\{a(x, v)\ :\ \|v\| = 1\} \leq M\|x\|$$

Furthermore, the Riesz-Fréchet representation theorem is used on the right hand-side, giving $b(\cdot) = \langle f, \cdot\rangle$, and a reformulation of (2.7) as:
Find u such that

$$Au = f$$

Next we prove that this formulation has a unique solution u. To prove this, the Banach fixed-point theorem is used. We let $\epsilon > 0$, and define the operator:

$$\begin{aligned} T:\, V &\to V \\ u &\mapsto u - \epsilon(Au - f) \end{aligned}$$

We need to show that T is a contraction. Let $u_1, u_2 \in V$. By utilizing the linearity of A and considering $u = u_1 - u_2$, we obtain the following expression:

$$\|Tu_1 - Tu_2\|^2 = \|u - \epsilon(Au)\|^2 = \|u\|^2 - 2\epsilon\langle u, Au\rangle + \epsilon^2\langle Au, Au\rangle$$

With $a(u, u) = \langle Au, u\rangle$ and $\langle Au, Au\rangle = a_u(Au) = a(u, Au)$, we obtain the following result:

$$\|Tu_1 - Tu_2\|^2 = \|u\|^2 - 2\epsilon a(u, u) + \epsilon^2 a(u, Au)$$

We use the coercivity and boundedness of $a(\cdot, \cdot)$ and boundedness of A to get:

$$\|Tu_1 - Tu_2\|^2 \leq \|u\|^2 - 2\epsilon\alpha\|u\|^2 + \epsilon^2 M^2\|u\|^2$$

Giving:

$$\|Tu_1 - Tu_2\|^2 \leq \|u\|^2(1 - 2\epsilon\alpha + \epsilon^2 M^2)$$

We choose $\epsilon < \frac{2\alpha}{M^2}$ such that $(1 - 2\epsilon\alpha + \epsilon^2 M^2) < 1$ and T becomes a contraction. Furthermore, if T has a fixed point u^* then $u^* - \epsilon(Au^* - f) = u^*$ resulting in $Au^* = f$. By the Banach fixed point theorem we have proven both existence and uniqueness. □

2.1.3 Galerkin finite element method

To solve problems such as (2.4), the space V can be approximated by a finite-dimensional space $V_h \subset V$. When both the trial function u_h and the test function v_h belong to the same finite-dimensional space V_h, it is referred to as the Galerkin method. The problem now reads:

$$\text{Find } u_h \in V_h \quad \text{such that} \quad a(u_h, v_h) = b(v_h) \quad \forall v_h \in V_h \tag{2.8}$$

If (2.8) holds for the basis functions of V_h , it holds for all elements in V_h due to the bilinearity of $a(\cdot, \cdot)$ and linearity of $b(\cdot)$. In this research, for simplicity, we assume that our domain Ω is a polygonal domain, meaning that the boundary $\partial\Omega$ consists of a finite number of straight lines [Knabner and Angermann, 2003]. Furthermore, we define $\mathcal{T}_h$ as a partition of our domain Ω into closed elements E, which can be triangles and/or quadrilaterals in two dimensions, and tetrahedra in three dimensions. Moreover, we consider:

$$h := \max\{\text{diam}(E) \mid E \in \mathcal{T}_h\}$$

In the case of a two-dimensional domain, the following definition, as given by [Knabner and Angermann, 2003], must hold.

Definition 3 (Triangulation of Ω in 2D [Knabner and Angermann, 2003]). *The partition of Ω into closed triangles E must have the following properties;*

(1) $\overline{\Omega} = \cup_{E \in \mathcal{T}_h} E$

(2) For E_1 *and* $E_2 \in \mathcal{T}_h$, $E_1 \neq E_2$

$$int(E_1) \cap int(E_2) = \emptyset$$

where int(E_1) denotes the interior of the triangle E_1.

(3) If $E_1 \neq E_2$ but $E_1 \cap E_2 \neq \emptyset$, then the intersection of the two elements is either a point or a common edge of the elements.

Having the triangulation, the finite-dimensional subspace V_h of V, consisting of piece-wise linear functions, is defined as follows:

$$V_h := \{u \in C(\overline{\Omega}) \mid u|_E \in \mathcal{P}_1(E)\ \forall\ E \in \mathcal{T}_h\}$$

where $\mathcal{P}_1(E)$ is the space of linear polynomials of first degree in 2 variables on the element $E \subset \mathbb{R}^2$. Furthermore, a basis for the vector space, V_h must be found. Having the discrete variational formulation given by (2.8) a basis for V_h can be represented by $\{\varphi_i\}_{i=1}^N$. Based on this formulation, we can write $u_h = \sum_{i=1}^N \eta_i \varphi_i$. By substituting this in (2.8) and testing with $v = \varphi_j$, the resulting system of N equations is given by:

$$\sum_{i=1}^{N} \eta_i a(\varphi_i, \varphi_j) = b(\varphi_j) \quad \forall j = 1, ..., N$$

By finding $a(\varphi_i, \varphi_j)$ and $b(\varphi_j)$ we obtain a solvable system of N equations and N unknowns η_i. In matrix form, this system can be expressed as:

$$\boldsymbol{A}\boldsymbol{\eta} = \boldsymbol{b} \tag{2.9}$$

with $\boldsymbol{A}_{j,i} = a(\varphi_i, \varphi_j)$, $\boldsymbol{\eta}_i = \eta_i$ and $\boldsymbol{b}_j = b(\varphi_j)$. In the finite element method we define the basis on a reference element $\hat{E}$ and establish a linear transformation from each element E to the reference element. This allows us to inherit the basis functions of $\hat{E}$, where each basis function is defined as $\varphi_i|_E$. For triangular elements a convenient reference element to choose is a triangle with vertices located at $(0,0)$, $(1,0)$ and $(0,1)$. Figure 2.1, inspired by [Ambartsumyan et al., 2021], illustrates the mapping from the reference element $\hat{E}$ to the element E.

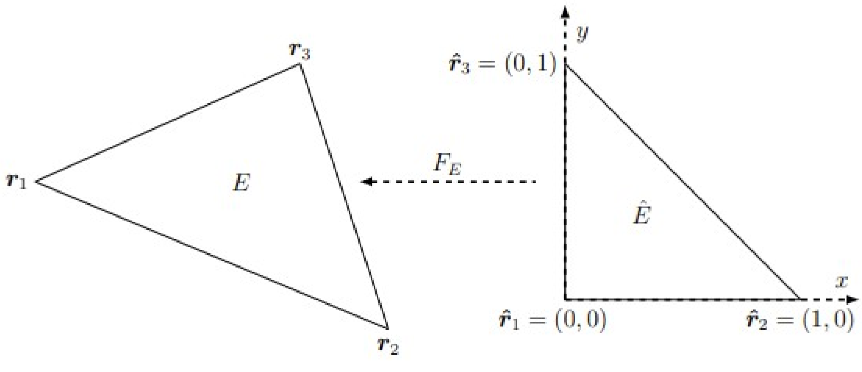

Figure 2.1: Mapping in the case of a triangle. The map F_E from the reference element $\hat{E}$ to element E.

Looking back at our system (2.9), we observe that the selection of basis leads to a sparse matrix $\boldsymbol{A}_{i,j} = a(\varphi_i, \varphi_j)$, meaning that only a subset of the matrix entries are nonzero. This sparsity property is an important property that leads to computational efficiency, particularly in terms of computational memory requirements.

2.1.4 The mixed varational formulation

The choice of mixed finite elements is motivated by their ability to provide accurate approximations of fluxes (stress and velocity) along with local linear momentum and mass conservation. In the mixed finite element method extra fields, which are constrained by using Lagrange multiplier fields, are introduced. Different quantities needs to be approximated simultaneously, resulting in a mixed finite element method. To explain the mixed finite element method, we use the Poisson problem in Example 1 from Section 2.1.1. The example is inspired by [Thomée, 1984], and the system (2.1) is reformulated to:

$$\begin{cases} -\nabla \cdot \theta = f & \text{in } \Omega, \\ \theta = \nabla u & \text{in } \Omega, \\ u = 0 & \text{on } \partial\Omega \end{cases} \tag{2.10}$$

The mixed variational formulation of the Poisson problem can then be written as:

Find $(\theta, u) \in H(\text{div}, \Omega) \times L^2(\Omega)$ such that:

$$\langle \theta, \tau \rangle + \langle u, \nabla \cdot \tau \rangle = 0 \quad \forall\, \tau \in H(\text{div}, \Omega), \tag{2.11a}$$

$$\langle \nabla \cdot \theta, v \rangle + \langle f, v \rangle = 0 \quad \forall\, v \in L^2(\Omega) \tag{2.11b}$$

2.1.5 Convergence of FEM

In the finite element method the question is whether the finite element solution u_h is a good approximation of the solution u to the variational formulation. Céa's lemma is introduced by employing the definitions provided in Definition 1.

Lemma 2.1.5 (Céa's lemma, [Knabner and Angermann, 2003] Chapter 2)**.**
Let $a(\cdot,\cdot)$ be continuous (2.5) and coercive (2.6), u the solution of (2.4) and u_h the Galerkin solution of (2.8), then the following error estimate holds:

$$\|u - u_h\| \leq \frac{M}{\alpha} \inf\{\|u - v\| \mid v \in V_h\} \tag{2.12}$$

Proof.
Note that both u and u_h solves the variational problem in V_h, resulting in:

$$a(u - u_h, v) = a(u, v) - a(u_h, v) = b(v) - b(v) = 0$$

This means that the error $u - u_h$ is orthogonal to the space V_h, referred to as Galerkin orthogonality. Furthermore, we have $u - u_h \in V_h$ resulting in $a(u - u_h, u_h - v) = 0$. Then since $a(\cdot, \cdot)$ is continuous and bounded we have:

$$\alpha \|u - u_h\|^2 \leq a(u - u_h, u - u_h) = \\ a(u - u_h, u - u_h) + a(u - u_h, u_h - v) = a(u - u_h, u - v)$$

Furthermore:

$$\alpha \|u - u_h\|^2 \leq a(u - u_h, u - v) \leq M\|u - u_h\|\|u - v\|$$

Dividing by $\alpha\|u - u_h\|$ on both sides we obtain:

$$\|u - u_h\| \leq \frac{M}{\alpha}\|u - v\|$$

The error estimate (2.12) follows by taking the infimum over $v \in V_h$. □

2.2 The MPFA and MPSA finite volume methods

In this research we develop and analyse a coupled multipoint stress-multipoint flux mixed finite element (MSMFE-MFMFE) method for the Biot system, coupled with a MFMFE method for the flow within the fracture. By providing a variational formulation of the finite volume multipoint flux approximation (MPFA), the MFMFE method allows us to apply mixed finite element tools during the analysis [Ambartsumyan et al., 2020b]. While the MPFA method considers fluxes at the sub-edge (sub-face in 3D) to enable local flux elimination and reduction to a cell-centered pressure scheme, the MFMFE method achieves a similar elimination by utilizing appropriate finite element spaces and a suitable quadrature rule. As a result, the MFMFE method achieves local elimination of velocity, leading to a cell-centered pressure system [Arrarás and Portero, 2019, Wheeler et al., 2012]. In a similar way, the MPSA method is based on local stress elimination around the vertices [Ambartsumyan et al., 2020a]. The development of the MFMFE method was motivated by the close relationship it shares with the MPFA method, while the development of the MSMFE method was driven by the MPSA method.

The implementation of the code in this research utilizes the simulation tool PorePy [Keilegavlen et al., 2021] with the use of inheritance, and it incorporates both the MPFA and MPSA methods. This implementation is a direct outcome of the close relationships these methods share with the MFMFE and MSMFE methods. A short introduction to the MPFA and MPSA methods are given in this section based on [Nordbotten and Keilegavlen, 2021, Aavatsmark, 2002, Nilsen et al., 2018].

To get a deeper understanding of the finite volume methods, consider the conservation equation:

$$\int_{\omega_k} \frac{\partial \eta}{\partial t} dV + \oint_{\partial \omega_k} \boldsymbol{f} \cdot \boldsymbol{n} dA = \int_{\omega_k} r dV \tag{2.13}$$

where $\omega_i \subset \Omega$ are control volumes that are non-overlapping. Within each control volume $\omega_i \subset \Omega$, we examine the impact of the flux term $\boldsymbol{f}$, the outward normal vector $\boldsymbol{n}$, and the internal source/sink terms r on the quantity. As at the moment we are only interested in the spatial discretization, the rest of the section disregards the temporal term. The general idea behind finite volume methods is to ensure that the conservation law holds throughout the domain, with the flux being computed across the boundaries of control volumes. When considering two control volumes, ω_{k_1} and ω_{k_2}, the intersection of their boundaries is referred to as a face, denoted e. The collection of these faces is denoted as $\mathcal{F}$, with $\mathcal{F}_k$ representing the collection of faces belonging to ω_k. With these definitions the steady-state equation of (2.13) is rewritten to:

$$\sum_{e \in \mathcal{F}_k} \int_e \boldsymbol{f} \cdot \boldsymbol{n}_{e,k} = \int_{\omega_k} r dV \tag{2.14}$$

By observing that the left-hand side is equivalent to the summation of fluxes across all control volumes ω_k along the cell faces ω, any finite volume method can be expressed in the following form:

$$\sum_{e \in \mathcal{F}_k} q_{e,k} = \int_{\omega_k} r dV \tag{2.15}$$

with $q_{e,k}$ being the integrated fluxes of ω_k over the cell face e. This will hold for any control volume in the partition of Ω. Additionally, if for any $e = \partial \omega_{k_1} \bigcap \partial \omega_{k_2}$ it holds that:

$$q_{e,k_1} = -q_{e,k_2} \tag{2.16}$$

then the finite volume method has local flux balance. Thus far we have shown the main building blocks of finite volume methods; the rest of the section will briefly discuss the MPFA and MPSA methods.

The flux can be approximated in different ways. Different examples are the two-point flux approximation (TPFA) and the multipoint flux approximation (MPFA). MPFA methods are designed to provide accurate discretization of flow equations in non-orthogonal grids, as noted by Aavatsmark [Aavatsmark, 2002]. In Porepy, the O-method for multipoint flux approximation is implemented, and thus it will be the method discussed in this context.

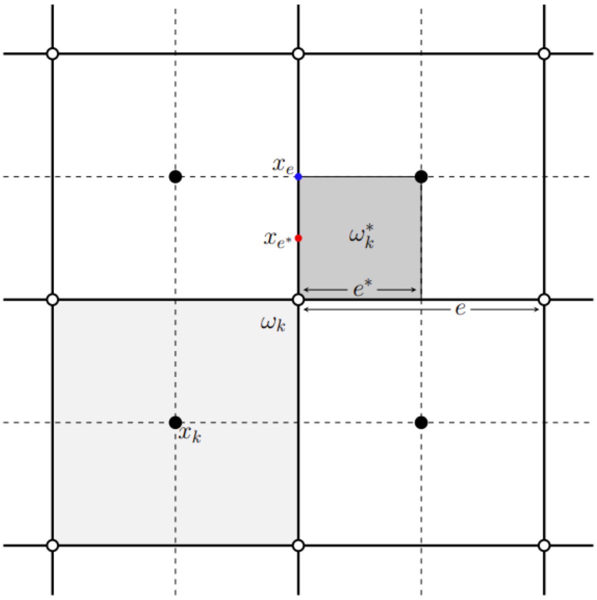

Figure 2.2: The solid lines are the cell (primal) grid and the dotted lines are the dual grid. The solid circles are cell centers x_k and the white circles are the interaction points.

As shown in Figure 2.2, inspired by [Jacobsen, 2022], the domain Ω is partitioned into control volumes ω_k with the solid black lines. This partition, known as the primal grid, is shown with a lighter grey area representing an example control volume. Each control volume has a cell center, denoted x_k, and face centers, denoted as x_e (shown in blue). By introducing a new grid, the dual grid, the MPFA method can be used. The dual grid is constructed by lines between x_k and x_e. A refined sub-grid is given by the intersections between the primal and the dual grid, where the cells are called sub-cells, denoted by ω_k^*, as shown in darker grey. The sub-cells consists of two solid line faces and two dashed line faces, where these sub-faces are denoted by e^*.

The potential is now described as a linear function on each sub-cell, where a continuity of the potential is enforced at each cell-center. From this potential field, a constant flux field is derived, where the flux is approximated over each sub-faces instead of the cell faces. Local flux balance is enforced over the sub-faces, giving us continuity in the flux. The integrated fluxes satisfy the following equation:

$$\int_{e^*} \boldsymbol{f} \cdot \boldsymbol{n}_{e^*_{k_1}} \, dS = -\int_{e^*} \boldsymbol{f} \cdot \boldsymbol{n}_{e^*_{k_2}} \, dS = q_{e^*}$$

The flux over a face is then constructed by summing the fluxes over all the subfaces corresponding to the face.

In Figure 2.2, the dual grid cells can be observed surrounding the interaction points, forming what is known as the interaction region. This region, represented by the 2-dimensional quadrilateral grid in Figure 2.2, consists of four sub-cells. Within these interaction regions, the principle of flux and potential continuity applies to each sub-cell. By assuming a linear potential and approximating it within each of the four sub-cells, a total of $4 \cdot 3 = 12$ degrees of freedom can be obtained. By requiring continuity of the potential at the midpoints of the interfaces, four conditions are established. Similarly, the flux continuity at the four sub-interfaces introduces an additional four conditions. Additionally, the linear potential must be equal to the values of the potential at the cell centers, resulting in another set of four conditions. Consequently, 12 conditions are imposed for the 12 degrees of freedom [Aavatsmark, 2002].

The MPSA method draws inspiration from the MPFA method. The MPSA method is derived based on the discrete principles of momentum conservation and continuity of forces, as outlined in [Nilsen et al., 2018]. In the method the stresses are approximated based on the gradient of displacements. Unlike the MPFA method, which solves the general conservation problem for a cell, the MPSA method focuses on solving the balance of linear momentum described by Equation (3.4) at each control volume.

Chapter 3

Poroelasticity in a fracture medium

Poroelasticity governs flow through a deformable porous medium [Storvik, 2022]. To study the phenomenon of poroelasticity, the quasi-static linear Biot model was developed, describing the interaction between the deformation of the elastic porous medium and the fluid flow within the medium [Skoglund, 2019]. The model takes the balance of both mass and linear momentum and Darcy's law into account, as well as adding the pore-pressure to the effective stress with the Biot-Willis coefficient. In this chapter the different model equations utilized in the fracture-domain are examined.

3.1 The system of Biot equations

In a deformable porous media, the quasi-static Biot model of poroelasticity describes the flow within the medium [Girault et al., 2015]. The model consists of equations that describe both the elastic behaviour and the fluid flow within the system. In this section an introduction to the different equations in $\Omega \backslash \mathcal{C}$ is given. Having a linear elastic, homogeneous, and isotropic body, where the porous medium is saturated with a slightly compressible viscous fluid, we have that the poroelastic Cauchy stress tensor is given by:

$$\boldsymbol{\sigma}(\boldsymbol{u}, p) = \boldsymbol{\sigma}_e(\boldsymbol{u}) - \alpha p \boldsymbol{I} \tag{3.1}$$

Here $\boldsymbol{u}$ is the displacement of the solid, $\boldsymbol{I}$ the identity tensor, p the pressure of the fluid, $0 < \alpha \leq 1$ the Biot-Willis coefficient and $\boldsymbol{\sigma}$ the linear stress tensor. The linear elastic stress tensor is given by:

$$\boldsymbol{\sigma}_e(\boldsymbol{u}) = \lambda(\nabla \cdot \boldsymbol{u})\boldsymbol{I} + 2\mu\boldsymbol{\epsilon}(\boldsymbol{u}) \tag{3.2}$$

Where $\lambda > 0$ and $\mu > 0$ are the Lamé's first and second parameters, respectively, and $\boldsymbol{\epsilon}(\boldsymbol{u}) = \frac{1}{2}(\nabla\boldsymbol{u}+(\nabla\boldsymbol{u})$ the linear strain tensor, describing the deformation of the body of the matrix and being positive for expansion [Mehrabia and Abousleiman, 2014]. By combining Equation (3.1) and (3.2) the Cauchy stress tensor is given by:

$$\boldsymbol{\sigma}(\boldsymbol{u}, p) = \lambda(\nabla \cdot \boldsymbol{u})\boldsymbol{I} + 2\mu\boldsymbol{\epsilon}(\boldsymbol{u}) - \alpha p\boldsymbol{I} \tag{3.3}$$

Having the Cauchy stress tensor defined in Equation (3.1) and by letting $\boldsymbol{f}$ be the body force of the porous medium, we have the balance of linear momentum of the solid given as:

$$-\nabla \cdot \boldsymbol{\sigma}(\boldsymbol{u}, p) = \boldsymbol{f} \quad \text{in} \quad \Omega\backslash\mathcal{C} \tag{3.4}$$

By inserting Equation (3.3) in the balance of linear momentum equation the first equation, the mechanics equation, of the quasi-static, linear Biot-model is:

$$-\nabla \cdot [\lambda(\nabla \cdot \boldsymbol{u})\boldsymbol{I} + 2\mu\boldsymbol{\epsilon}(\boldsymbol{u})] + \alpha\nabla \cdot (p\boldsymbol{I}) = \boldsymbol{f} \tag{3.5}$$

With the mechanics equation established for the quasi-static, linear Biot model, we still require the two additional equations that describe the fluid flow within the medium. A linearized, slightly compressible single-phase model for the fluid, as in [Girault et al., 2015, Girault et al., 2016, Girault et al., 2018] is used. We define the variables p_r as the reference pressure, ρ_f as the density of the fluid, $\rho_r > 0$ as a constant reference density relative to the reference pressure, and c_f as the compressibility of the fluid. The linearized fluid density is then given by:

$$\rho_f = \rho_r(1 + c_f(p - p_r)) \tag{3.6}$$

where both c_f and $c_f(p - p_r)$ are assumed to be small. We introduce the fluid volume content of the medium, denoted as ϕ^*. In a poroelastic medium with small deformation, ϕ^* is related to the displacement and the pressure by the following relationship:

$$\phi^* = \phi_0 + \frac{p}{M} + \alpha\nabla \cdot \boldsymbol{u} \tag{3.7}$$

Here ϕ_0 represents the initial porosity of the medium, M denotes the Biot modulus, which is a constant related to compressibility, and α represents the Biot-Willis coefficient. The first equation describing the fluid flow in $\Omega\backslash\mathcal{C}$ is the mass balance equation, derived in Section 1.4. Within $\Omega\backslash\mathcal{C}$ the mass balanced equation is expressed as follows:

$$\frac{\partial}{\partial t}(\rho_f\phi^*) + \nabla \cdot (\rho_f\boldsymbol{q}) = \psi \tag{3.8}$$

By inserting Equation (3.6) and (3.7) into Equation (3.8) the following is obtained:

$$\frac{\partial}{\partial t}(\rho_r(1 + c_f(p - p_r))(\phi_0 + \frac{p}{M} + \alpha\nabla \cdot \boldsymbol{u})) + \nabla \cdot (\rho_r(1 + c_f(p - p_r))\boldsymbol{q}) = \psi$$

That results in the following expanded equation:

$$\rho_r(\frac{1}{M}(1+c_f(p-p_r))+c_f(\phi_0+\alpha\nabla\cdot\boldsymbol{u}+\frac{1}{M}p))\frac{\partial p}{\partial t} \\ +\rho_r(1+c_f(p-p_r))\alpha\nabla\cdot\frac{\partial \boldsymbol{u}}{\partial t}+\nabla\cdot(\rho_r(1+c_f(p-p_r))\boldsymbol{q})=\psi$$

The following approximations can be made by neglecting quantities whose the values become small:

$$\begin{cases} \frac{1}{M}(1+c_f(p-p_r))\approx\frac{1}{M} \\ c_f(\phi_0+\alpha\nabla\cdot\boldsymbol{u}+\frac{1}{M}p)\approx c_f\phi_0 \\ \rho_r(1+c_f(p-p_r))\alpha\approx\rho_r\alpha \\ \rho_r(1+c_f(p-p_r))\boldsymbol{q}\approx\rho_r\boldsymbol{q} \end{cases}$$

hence, the reduced form becomes:

$$\rho_r(\frac{1}{M}+c_f\phi_0)\frac{\partial p}{\partial t}+\rho_r\alpha\nabla\cdot\frac{\partial \boldsymbol{u}}{\partial t}+\rho_r\nabla\cdot\boldsymbol{q}=\psi$$

By letting $\frac{\psi}{\rho_r}=\hat{\psi}$ and taking $\frac{1}{M}+c_f\phi_0=c_0$, the mass balance equation becomes:

$$\frac{\partial}{\partial t}(c_0p+\alpha\nabla\cdot\boldsymbol{u})+\nabla\cdot\boldsymbol{q}=\hat{\psi} \tag{3.9}$$

Equation (3.9) represents the second equation in the quasi-static, linear Biot model. The fluid velocity within the reservoir matrix is described by Darcy's equation, discussed in Section 1.3, and can be expressed as follows:

$$\boldsymbol{q}=-\frac{\boldsymbol{k}}{\mu_f}(\nabla p-\rho_f\boldsymbol{g})=-\frac{\boldsymbol{k}}{\mu_f}(\nabla p-\rho_f g\nabla\eta) \tag{3.10}$$

In the equation, $\boldsymbol{k}$ denotes the absolute permeability tensor, which is assumed to be symmetric, bounded, uniformly positive definite in space, and constant in time. The variable η represents the distance in the vertical direction, which is constant in time and variable in space.

Remark 1. *For simplicity, the gravitational term is neglected during the analysis.*

Letting $\boldsymbol{K}=-\frac{k\rho_f}{\mu_f}=-\frac{k}{\nu_f}$, with ν_f being the kinematic viscosity, and rearranging Equation (3.10), the last equation in the reservoir matrix is:

$$\boldsymbol{K}^{-1}\boldsymbol{q}+\nabla p=\rho_f g\nabla\eta \tag{3.11}$$

The equations within the reservoir matrix correspond to the linear quasi-static Biot equations. By setting the body force in Equation (3.4) as $\boldsymbol{f}_1$ and the source term in the conservation of mass equation (3.9) as f_2, the equations within the reservoir matrix becomes:

$$-\nabla \cdot \boldsymbol{\sigma}(\boldsymbol{u}, p) = \boldsymbol{f_1} \tag{3.12a}$$

$$\frac{\partial}{\partial t}(c_0 p + \alpha \nabla \cdot \boldsymbol{u}) + \nabla \cdot \boldsymbol{q} = f_2 \tag{3.12b}$$

$$\boldsymbol{K}^{-1}\boldsymbol{q} + \nabla p = 0 \tag{3.12c}$$

3.2 Fractures in a poroelastic medium

Recall that in our model, the fracture will be approximated by a single line when $d = 2$ and a surface when $d = 3$. Thus, the domain $\mathcal{C}$ is of one dimension less than $\Omega \backslash \mathcal{C}$. In this section the equations describing the flow through the fracture are introduced. During the analysis, it is assumed that the fracture will not propagate, meaning that the front of the fracture is stationary. The pressure p is assumed to belong to $H^1(\Omega)$, resulting in a well-defined trace p_c on $\mathcal{C}$. As seen in [Girault et al., 2015, Girault et al., 2018] the flow rate within the fracture, $\boldsymbol{q}_c$, is described with a form of the Reynolds lubrication equation:

$$\boldsymbol{q}_c = -\frac{w^3}{12\mu_f}(\overline{\nabla} p_c - \rho g \overline{\nabla} \eta) \tag{3.13}$$

Here w denotes the width of the fracture, being a non-negative function equal to the jump of displacement $\boldsymbol{u}$ in the normal direction. The surface gradient operator on $\mathcal{C}$ is denoted as $\overline{\nabla}$. The surface gradient operator corresponds to the tangential trace of the gradient and is well-defined for functions in $H^1(\Omega)$. It is important to note that this operator is not utilized in the context of this research.

Remark 2. *In this work, for simplcity reasons, the tensor $\boldsymbol{K}_c$, which represents the permeability integrated over the width of the fracture is introduced. It is assumed that $\boldsymbol{K}_c$ is a positive definite constant tensor.*

Considering Remark 1 and Remark 2, the volumetric flow rate within the fracture $\mathcal{C}$ in this research can be expressed as follows:

$$\boldsymbol{K}_c^{-1}\boldsymbol{q}_c + \overline{\nabla} p_c = 0$$

As discussed in Section 1.5 the two sides of the fracture $\mathcal{C}$ were distinguished by the superscript $*$, with $* = +, -$. The region of Ω adjacent to $\mathcal{C}^*$ was denoted Ω^*, and $\boldsymbol{n}^*$ represents the unit normal vector to $\mathcal{C}$ exterior to Ω^*. If we have a function g defined in the matrix $\Omega \backslash \mathcal{C}$ and having a trace, then g^* denotes the trace of g on $\mathcal{C}^*$. The jump of g in the direction of $\boldsymbol{n}^+$ is given by:

$$[g]_{\mathcal{C}} = g^+ - g^-$$

The width w of the fracture is determined by the jump of $\boldsymbol{u} \cdot \boldsymbol{n}^-$ on $\mathcal{C}$ which can be expressed as:

$$w = -[\boldsymbol{u}]_{\mathcal{C}} \cdot \boldsymbol{n}^+$$

In the papers [Girault et al., 2016, Girault et al., 2015, Girault et al., 2018], the conservation of mass is described by the following equation:

$$\frac{\partial}{\partial t}(\rho_f w) + \overline{\nabla} \cdot (\rho_f \boldsymbol{q}_c) = q_W - q_L \tag{3.14}$$

with q_W and q_L being a known injection term into the fracture and an unknown leakage from the fracture into the reservoir matrix, respectively. By defining $\frac{q_W}{\rho_r} = f_3$ and $\frac{q_L}{\rho_r} = \hat{q}_L$, and considering the relationship between displacement and the width of the fracture, as well as the approximations presented in Section 3.1, the conservation of mass within the fracture in this research can be expressed as follows:

$$\frac{\partial}{\partial t}(c_0 p_c) - \frac{\partial}{\partial t}([\boldsymbol{u}] \cdot \boldsymbol{n}^+) + \overline{\nabla} \cdot \boldsymbol{q}_c = f_3 - \hat{q}_L \tag{3.15}$$

The equations within the fracture becomes:

$$\boldsymbol{K}_c^{-1} \boldsymbol{q}_c + \overline{\nabla} p_c = 0 \tag{3.16a}$$

$$\frac{\partial}{\partial t}(c_0 p_c) - \frac{\partial}{\partial t}([\boldsymbol{u}] \cdot \boldsymbol{n}^+) + \overline{\nabla} \cdot \boldsymbol{q}_c = f_3 - \hat{q}_L \tag{3.16b}$$

3.3 Interface, boundary and initial conditions

In Section 3.1, the equations in $\Omega \backslash \mathcal{C}$ were derived and presented as Equations (3.12). The equations in the fracture $\mathcal{C}$ were given in Section 3.2 as Equations (3.16). To complete the system, we need to introduce the interface, initial, and boundary conditions. We let $\boldsymbol{\tau}_j^\star$, where $1 \leq j \leq d-1$, be the set of orthonormal tangent vectors on $\mathcal{C}^\star$. The first interface condition on each side of $\mathcal{C}$ is a result of the balance of the normal traction vector and the conservation of mass, and it is given by:

$$(\boldsymbol{\sigma}(\boldsymbol{u}, p))^\star \boldsymbol{n}^\star = -p_c \boldsymbol{n}^\star \tag{3.17}$$

As a result of Equation (3.17) and the continuity of pressure across the fracture, we have:

$$[\boldsymbol{\sigma}(\boldsymbol{u}, p))]_{\mathcal{C}} \boldsymbol{n}^\star = \boldsymbol{0}$$

and, Equation (3.17) also implies:

$$\boldsymbol{\sigma}(\boldsymbol{u}, p)^\star \boldsymbol{n}^\star \cdot \boldsymbol{n}^\star = -p_c, \quad \boldsymbol{\sigma}(\boldsymbol{u}, p)^\star \boldsymbol{n}^\star \cdot \boldsymbol{\tau}^\star = 0$$

These interface conditions also indicate our disregard for tangential resistance in fracture. The conservation of mass at the interface yields from the above approximations, and is expressed as follows:

$$[\boldsymbol{K}\nabla p]_{\mathcal{C}} \cdot \boldsymbol{n}^{+} = \hat{q}_L \tag{3.18}$$

with $\hat{q}_L$ being the unknown leakage term from the fracture into the reservoir divided by the reference density. There is also a continuity of pressure across the interfaces, ensuring that the pressure within the fracture remains equal to the pressure in the reservoir matrix adjacent to the fracture:

$$p^{*} = p_c \tag{3.19}$$

Thus, the interface conditions have been introduced, while the boundary and initial conditions for our system are yet to be presented. The boundary conditions can be divided into Dirichlet boundary conditions and Neumann boundary conditions. The boundary conditions in this research are given by:

$$\boldsymbol{u} = \boldsymbol{g_u} \quad \text{on } \Gamma_D^{\text{disp}}, \qquad \boldsymbol{\sigma} \cdot \boldsymbol{n} = \boldsymbol{g_\sigma} \quad \text{on } \Gamma_N^{\text{stress}} \tag{3.20}$$

$$p = g_p \quad \text{on } \Gamma_D^{\text{pres}}, \qquad \boldsymbol{q} \cdot \boldsymbol{n} = \boldsymbol{g_q} \quad \text{on } \Gamma_N^{\text{vel}} \tag{3.21}$$

The initial condition can be defined by considering that the time derivative in Equation (3.9) operates on $c_0 p + \alpha \nabla \cdot \boldsymbol{u}$, resulting in:

$$(c_0 p + \alpha \nabla \cdot \boldsymbol{u})(0) = c_0 p_0 + \alpha \nabla \cdot \boldsymbol{u}_0 \tag{3.22}$$

here p_0 and $\boldsymbol{u}_0$ represent the initial pressure and displacement, respectively. Our complete problem follows from solving the equations in (3.12) for the reservoir matrix and the equations in (3.16) for the fracture over the entire time range $t \in [0, T]$. The problem is governed by the interface conditions (3.17) and (3.18) on $\mathcal{C}$, as well as the boundary conditions (3.20) and (3.21) on $\partial\Omega$ and initial condition (3.22) at time $t = 0$. The complete problem statement is shown in the next section.

Remark 3. *For simplicity reasons we have adopted the continuity of pressure in equation (3.19) as an interface condition, as demonstrated in [Kumar et al., 2020, List et al., 2020]. This justification holds when the fracture permeability in the normal direction is significantly large. More general conditions, such as pressure jumps as discussed in [Martin et al., 2005a, Formaggia et al., 2014, Fumagalli and Scotti, 2013], can also be considered here. The continuity condition is widely used in practice [Reichenberger et al., 2006].*

3.4 The complete problem statement

As previously mentioned, in this research, we express the poroelastic system with flow in a fracture using a fully mixed formulation due to its advantages in enabling locally conservative schemes. This section will present the complete strong form of our problem, written in the fully mixed form.

Remark 4. *For simplicity, we will not represent vectors and tensors by bold letters from now on.*

We begin by introducing the stress-strain constitutive relationship for the poroelastic body, given by:

$$A\sigma_e = \epsilon(u) \tag{3.23}$$

Here $A = A(x)$ is a compliance tensor describing the properties of the material at each point in the domain, where A is a symmetric, bounded, positive definite linear operator acting from $\mathbb{S} \to \mathbb{S}$. The displacement is denoted by u, which can be described as $\epsilon(u) = \frac{1}{2}(\nabla u + \nabla u^T)$, where $\epsilon(u)$ represents the strain tensor. The elastic stress, denoted σ_e, is given by:

$$\sigma_e = 2\mu\epsilon(u) + \lambda(\nabla \cdot u)I \tag{3.24}$$

with $\mu > 0$ and $\lambda > 0$ being the Lamé parameters and I the identity tensor. The poroelastic stress, which includes the effect of fluid pressure p, is given by:

$$\sigma = \sigma_e - \alpha p I \tag{3.25}$$

with α being the Biot-Willis constant. Having a homogeneous and isotropic body gives:

$$A\sigma_e = \frac{1}{2\mu}(\sigma - \frac{\lambda \operatorname{tr}(\sigma)I}{2\mu + \lambda d} - \frac{\lambda\alpha p d I}{2\mu + \lambda d} + \alpha p I) \tag{3.26}$$

where Equation (3.26) is the compliance form of the equation. Recalling the equations in the reservoir matrix, Equation (3.12), as presented in Section 3.1, we can express the fluid flow within a poroelastic medium in terms of a vector field f_1 representing the body forces and a source term f_2 as follows:

$$-\nabla \cdot \sigma = f_1 \quad \text{in } \Omega\backslash\mathcal{C} \times (0,T] \tag{3.27a}$$

$$\frac{\partial}{\partial t}(c_0 p + \alpha\nabla \cdot u) + \nabla \cdot q = f_2 \quad \text{in } \Omega\backslash\mathcal{C} \times (0,T] \tag{3.27b}$$

$$K^{-1}q + \nabla p = 0 \quad \text{in } \Omega\backslash\mathcal{C} \times (0,T] \tag{3.27c}$$

This system is closed with the following boundary conditions:

$$u = g_u \quad \text{on } \Gamma_D^{\text{disp}} \times (0,T] \qquad \sigma \cdot n = g_\sigma \quad \text{on } \Gamma_N^{\text{stress}} \times (0,T] \tag{3.28}$$

$$p = g_p \quad \text{on } \Gamma_D^{\text{pres}} \times (0,T] \qquad q \cdot n = g_q \quad \text{on } \Gamma_N^{\text{vel}} \times (0,T] \tag{3.29}$$

and an initial condition equal to $p(x,0) = p_0(x)$ in $\Omega \backslash \mathcal{C}$. The boundaries given in equation (3.28) and (3.29) yields the following equality $\Gamma_D^u \cup \Gamma_N^\sigma = \Gamma_D^p \cup \Gamma_N^{\text{vel}} = \partial\Omega$ and n is the outward unit normal vector field on $\partial\Omega$. To avoid technical issues, we assume that there is always a Dirichlet boundary condition present at least on one of the boundaries. In other words, the Lebesgue measures of Γ_D^u and Γ_D^p are both positive.

To use mixed finite element for elasticity with weakly symmetric stress, we introduce the Lagrange multiplier $\gamma = \text{Skew}(\nabla u) = \frac{1}{2}(\nabla u - (\nabla u)^T)$. From the Lagrange multiplier, the constitutive relationship (3.23), and Equation (3.25), the constitutive relation can be rewritten as:

$$A(\sigma + \alpha p I) = \nabla u - \gamma$$

Furthermore, $\nabla \cdot u = \text{tr}(\epsilon(u)) = \text{tr}(A\sigma_e) = \text{tr}A(\sigma + \alpha p I)$, which inserted into (3.27b) results in:

$$\frac{\partial}{\partial t}(c_0 p + \alpha \text{tr} A(\sigma + \alpha p I)) + \nabla \cdot q = f_2$$

By recalling that the elastic stress is $\sigma_e = 2\mu\epsilon(u) + \lambda(\nabla \cdot u)I$, and that the poroelastic stress is given by:

$$\sigma = \sigma_e - \alpha p I$$

the complete model problem written on a mixed form is given by Problem 1. In this problem, the skew-operator is applied, which implies that a matrix A is considered skew-symmetric if it satisfies the condition $A^T = -A$.

Problem 1.

The equations for our model problem, expressed on the mixed strong form with the use of the Lagrange multiplier, are given by:

$$A(\sigma + \alpha p I) = \nabla u - \gamma \tag{P1.1}$$

$$-\nabla \cdot \sigma = f_1, \quad \text{in } \Omega \backslash \mathcal{C} \times (0,T] \tag{P1.2}$$

$$\text{skew}(\sigma) = 0 \tag{P1.3}$$

$$K^{-1} q + \nabla p = 0, \quad \text{in } \Omega \backslash \mathcal{C} \times (0,T] \tag{P1.4}$$

$$\frac{\partial}{\partial t}(c_0 p + \alpha \text{tr} A(\sigma + \alpha p I)) + \nabla \cdot q = f_2, \quad \text{in } \Omega \backslash \mathcal{C} \times (0,T] \tag{P1.5}$$

$$K_c^{-1} q_c + \overline{\nabla} p_c = 0, \quad \text{in } \mathcal{C} \times (0,T] \tag{P1.6}$$

$$\frac{\partial}{\partial t}(c_0 p_c) - \frac{\partial}{\partial t}([u] \cdot n^+) + \overline{\nabla} \cdot q_c = f_3 - \hat{q}_L, \quad \text{in } \mathcal{C} \times (0,T] \tag{P1.7}$$

Interface conditions:

$$\sigma^\star \cdot n^\star = -p_c \cdot n^\star \quad \text{on } \mathcal{C} \tag{P1.8}$$

$$p^* = -p_c \quad \text{on } \mathcal{C} \tag{P1.9}$$

$$[K \nabla p]_{\mathcal{C}} \cdot n^+ = \hat{q}_L \quad \text{on } \mathcal{C} \tag{P1.10}$$

Boundary conditions:

$$u = g_u \quad \text{on } \Gamma_D^{\text{disp}} \times (0,T] \qquad \sigma \cdot n = g_\sigma \quad \text{on } \Gamma_N^{\text{stress}} \times (0,T] \tag{P1.11}$$

$$p = g_p \quad \text{on } \Gamma_D^{\text{pres}} \times (0,T] \qquad q \cdot n = g_q \quad \text{on } \Gamma_N^{\text{vel}} \times (0,T] \tag{P1.12}$$

Initial condition:

$$(c_0 p + \alpha \nabla \cdot u)(0) = c_0 p_0 + \alpha \nabla \cdot u_0 \quad \text{at } t = 0 \tag{P1.13}$$

Figure 3.1, similar to Figure 1.4, illustrates an example of a fracture within a $2D$ poroelastic medium. The blue line represents the fracture, while the orange lines represent the interfaces..

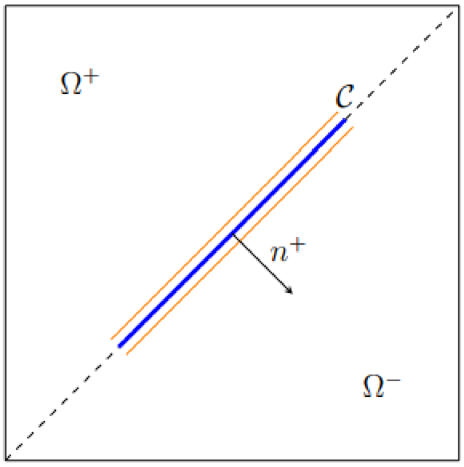

Figure 3.1: A fracture embedded in a two dimensional poroelastic medium. The orange lines represent the interfaces and the blue line represent the fracture.

Chapter 4

Variational formulation

In this chapter we present our research on the fully mixed variational problem concerning our system, as defined in Problem 1 in Section 3.4. Furthermore, the results of a stability analysis are given. Our problem is solved over the spatial domain Ω and in the time interval $(0, T)$, with T being the final time. A fully mixed variational formulation of our poroelastic system with a fracture embedded in the medium will be given. This formulation involves a mixed stress-displacement-rotation formulation for the elasticity, coupled with a mixed velocity-pressure Darcy formulation for both the matrix and the fracture.

The chapter begins with an introduction to general spaces and notation, and continues with an introduction of the test functions. Then we derive the fully mixed variational formulation for the equations in both the reservoir matrix and in the fracture. In the end a stability analysis of our method is presented. In this chapter theory from [Girault et al., 2018] and [Ambartsumyan et al., 2020b] is combined. Additionally, for Section 4.1, we incorporate theory from [Knabner and Angermann, 2003, Cheney, 2001], as well as literature from the course on functional analysis at the University of Bergen [Radu, 2022].

4.1 General spaces and notation

We let Ω denote a simply connected bounded domain of $\mathbb{R}^d$, where $d = 2, 3$. The domain has a Lipschitz continuous boundary $\partial\Omega$ with an open subset Γ having a positive measure. The domain is occupied by a poroelastic medium saturated with a fluid. A fracture $\mathcal{C}$ is embedded in the domain, where $\mathcal{C} \subset \mathbb{R}^{d-1}$. Before discussing the fully mixed formulation, some general spaces and operators are introduced. The spaces of $d \times d$ matrices, symmetric matrices and skew-symmetric matrices are denoted by $\mathbb{M}$, $\mathbb{S}$ and $\mathbb{N}$, respectively. Moreover, the divergence operator is employed on both vector fields and matrix fields. When utilized on a matrix field it produces a vector field, where the divergence is taken at each row. The curl operator will also be used, which, when applied on scalar fields φ in two dimensions, is defined as $\nabla \times \varphi = (\partial_2 \varphi, -\partial_1 \varphi)$. The letter C will represent a positive constant that is independent from the discretization parameter h. From now on, we assume that $\Omega \subset \mathbb{R}^d$ and proceed to provide the definition of Lebesgue spaces.

Definition 4 (Lebesgue spaces, $L^p(\Omega)$).
For $p \in [1, \infty)$, then the $L^p(\Omega)$-spaces, Lebesgue spaces, are:

$$L^p(\Omega) = \left\{ f : \|f\|_{L^p(\Omega)} = \left(\int_\Omega |f|^p dx \right)^{\frac{1}{p}} < \infty \right\}$$

Having the domain $\Omega \subset \mathbb{R}^d$, $(\cdot, \cdot)$ and $\| \cdot \|$ denotes the $L^2(\Omega)$ inner product and norm, respectively, are introduced. Furthermore, the Hilbert spaces, denoted $H^k(\Omega)$, have the norms and semi-norms denoted by $\| \cdot \|_k$ and $| \cdot |_k$, respectively. To define Hilbert spaces, some definitions are given.

Definition 5. *Let $\{X_n\}$ be a sequence in a normed linear space X. Then $\{x_n\}$ is said to be a Cauchy sequence if for all $\epsilon > 0$ there exists an $N \in \mathbb{N}$ such that:*

$$\|x_i - x_j\| < \epsilon \quad \forall i, j \geq N$$

Definition 6. *The space X is said to be complete if every Cauchy sequence in the space X is convergent. A complete normed linear space is called a Banach space. A Banach space having an inner-product $\langle \cdot, \cdot \rangle$ that induces the norm $\langle \cdot, \cdot \rangle^{\frac{1}{2}} = \| \cdot \|$ is called a Hilbert space.*

Theorem 4.1.1 (The Riesz-Fischer theorem [Cheney, 2001] Chapter 8). *Every L^p-space is a Banach space.*

The Sobolev space is denoted by $W^{r,p}(\Omega)$ where r is a non-negative integer and $p \in [1, \infty)$. The norms and the semi-norms of the Sobolev space are denoted by $\| \cdot \|_{r,p}$ and $| \cdot |_{r,p}$, respectively.

Theorem 4.1.2 ([Adams and Fournier, 2003], Chapter 3). *Every Sobolev space $W^{r,p}(\Omega)$ is a Banach space.*

Note that when $r = 1$, $W^{1,p}(\Omega)$ is the space:

$$W^{1,p}(\Omega) = \{v \in L^p(\Omega)\ ;\ \nabla v \in L^p(\Omega)^d\}$$

equipped with the semi-norm and norm:

$$|v|_{W^{1,p}(\Omega)} = \|\nabla v\|_{L^p(\Omega)}, \quad \|v\|_{W^{1,p}(\Omega)} = (\|v\|^p_{L^p(\Omega)} + |v|^p_{W^{1,p}(\Omega)})^{\frac{1}{p}}$$

Furthermore, when $p = 2$, $W^{1,2}(\Omega)$ corresponds to the classical Hilbert Sobolev space $H^1(\Omega)$, where:

$$H^1(\Omega) = \{v \in L^2(\Omega) : \nabla v \in L^2(\Omega)^d\}$$

The space $H^{\frac{1}{2}}(\Gamma)$ is the space of traces of functions of $H^1(\Omega)$ on $\Gamma \subset \partial\Omega$. It is a proper subspace of $L^2(\Gamma)$ and has a dual space denoted by $H^{-\frac{1}{2}}(\Gamma)$. In this research, it is convenient to employ the following semi-norm and norm of the $H^{\frac{1}{2}}(\Gamma)$ space:

$$|v|_{H^{\frac{1}{2}}(\Gamma)} = \left(\int_\Gamma \int_\Gamma \frac{|v(\boldsymbol{x}) - v(\boldsymbol{y})|^2}{|\boldsymbol{x} - \boldsymbol{y}|^d} d\boldsymbol{x} d\boldsymbol{y}\right)^{\frac{1}{2}}, \quad \|v\|_{H^{\frac{1}{2}}(\Gamma)} = \left(\|v\|^2_{L^2(\Gamma)} + |v|^2_{H^{\frac{1}{2}}(\Gamma)}\right)^{\frac{1}{2}}$$

Furthermore, we define the spaces:

$$H^1_0(\Omega) = \{v \in H^1(\Omega)\ ;\ v|_{\partial\Omega} = 0\} \quad \text{and} \quad H^1_{0,\Gamma}(\Omega) = \{v \in H^1(\Omega)\ ;\ v|_\Gamma = 0\}$$

The Cauchy-Schwarz and Young's inequalities that are used in the sequel are introduced.

Lemma 4.1.3 (Cauchy-Schwarz inequality).
Having $(X, \langle \cdot, \cdot \rangle_X)$ a normed vector space with the norm induced by an inner product. For $u, v \in X$ the following estimate holds:

$$|\langle u, v \rangle_X| \leq \|u\|_X \|v\|_X$$

Lemma 4.1.4 (Young's inequality).
Let a, b be two non-negative real number, $a, b > 0$. Then:

$$ab \leq \frac{1}{2\epsilon} a^2 + \frac{\epsilon}{2} b^2, \quad \forall\, \epsilon > 0$$

Furthermore, during the stability analysis the Grönwall's lemma is applied. The following lemma is one version of Grönwall's lemma given in [Dieudonné, 1960].

Lemma 4.1.5 (Grönvall's lemma [Dieudonné, 1960]).
Let $y(t)$, $f(t)$ and $g(t)$ be non-negative functions on $[0, T]$ having one-sided limits at every $t \in [0, T]$, and assume that for $0 \leq t \leq T$ we have:

$$y(t) \leq f(t) + \int_0^t g(s) y(s) ds$$

Then for $0 \leq t \leq T$ we also have:

$$y(t) \leq f(t) + \int_0^t g(s) f(s) \exp\left(\int_0^t g(u) du\right) ds$$

In this work, the divergence operator $(\nabla\cdot)$ is concerned, and for that purpose, we introduce the following space:

$$H(\mathrm{div};\Omega) = \{\boldsymbol{v} \in L^2(\Omega)^d : \nabla\cdot\boldsymbol{v} \in L^2(\Omega)\}$$

equipped with the following norm:

$$\|\boldsymbol{v}\|_{H(\mathrm{div};\Omega)} = (\|\boldsymbol{v}\|^2_{L^2(\Omega)} + \|\nabla\cdot\boldsymbol{v}\|^2_{L^2(\Omega)})^{\frac{1}{2}}$$

Note that:

$$H(\mathrm{div};\Omega,\mathbb{M}) = \{\tau \in L^2(\Omega,\mathbb{M}) : \nabla\cdot\tau \in L^2(\Omega)\}$$

This research has time-dependent problems and therefore it is convenient to consider functions defined on a time interval $t \in [a,b]$, with values in a function space X. We let $p \in [1,\infty)$, and denote the norm of the space X as $\|\cdot\|_X$, then for any $p \in [1,\infty)$, we have:

$$L^p(a,b;X) = \left\{ f \text{ measurable in } [a,b] \ : \ \int_a^b \|f(t)\|^r_X \, dt < \infty \right\}$$

equipped with the norm:

$$\|f\|_{L^p(a,b;X)} = \left(\int_a^b \|f(t)\|^p_X \, dt \right)^{\frac{1}{p}}$$

If X is a Banach, then $L^p(a,b;X)$ is also a Banach space. When $p = 2$, $L^p(a,b;X)$ is a Hilbert space if X is a Hilbert space. We denote the derivative with respect to time as $\frac{\partial}{\partial t}$ and define:

$$H^1(a,b;X) = \left\{ f \in L^2(a,b;X)\ ;\ \frac{\partial f}{\partial t} \in L^2(a,b;X) \right\}$$

$$H^1_0(a,b;X) = \left\{ f \in H^1(a,b;X)\ ;\ f(a) = f(b) = 0 \right\}$$

as the functions of $H^1(a,b;X)$ are continuous with respect to time. The dual space of $H^1_0(a,b;X)$ is denoted as $H^{-1}(a,b;X)$.

4.2 Mixed variational formulation

In this section we derive and describe the fully mixed variational formulation of our poroelastic system with a fracture embedded in the medium, i.e. a mixed stress-displacement-rotation formulation for the elasticity will be coupled with a mixed velocity-pressure Darcy formulation in both the matrix and the fracture.

As this research employs an MSMFE-MFMFE method, there a number of unknowns and corresponding test-functions involved in the formulation. Table 4.1 presents the unknowns of our problem and their corresponding test functions.

Table 4.1: Symbols of the unknown parameters and their corresponding test functions

Unknown parameter	Symbol of parameter	Test function
Stress	σ	τ
Displacement	u	v
Rotation	γ	ξ
Pressure in reservoir	p	θ
Pressure in fracture	p_c	θ_c
Flux in reservoir	q	z
Flux in fracture	q_c	z_c
Mortar displacement	χ	v_c

4.2.1 Variational formulation in the reservoir matrix

In this section the mixed weak formulation for the equations within the reservoir are derived. We first note, as mentioned in Section 3.4, that:

$$A(\sigma + \alpha pI) = A\sigma_e = \epsilon(u) = \frac{1}{2}(\nabla u + \nabla u^T) = \nabla u - \frac{1}{2}(\nabla u - \nabla u^T) = \nabla u - \gamma$$

where γ is the skew-symmetric part of ∇u. The above equation is multiplied by the test function τ and we integrate by parts with respect to the ∇u term:

$$\begin{aligned}\int_{\Omega^+} A(\sigma + \alpha pI)\tau dx = \int_{\Omega^+} (\nabla u - \gamma)\tau dx = \int_{\Omega^+} \nabla u \tau dx - \int_{\Omega^+} \gamma\tau dx \\ = -\int_{\Omega^+} u(\nabla \cdot \tau)dx + \int_{\partial\Omega^+} u\tau \cdot n ds - \int_{\Omega^+} \gamma\tau dx\end{aligned}$$

Doing the same over Ω^- a similar result is obtained:

$$\begin{aligned}\int_{\Omega^-} A(\sigma + \alpha p I)\tau dx = \int_{\Omega^-} (\nabla u - \gamma)\tau dx = \int_{\Omega^-} \nabla u \tau dx - \int_{\Omega^-} \gamma\tau dx \\ = -\int_{\Omega^-} u(\nabla \cdot \tau)dx + \int_{\partial\Omega^-} u\tau \cdot n ds - \int_{\Omega^-} \gamma\tau dx\end{aligned}$$

The two results for Ω^+ and Ω^- are combined, and the integrals over the boundaries are placed on the right-hand side, while the integrals over the domain are placed on the left-hand side:

$$\begin{aligned}\int_{\Omega^+ \cup\, \Omega^-} A(\sigma + \alpha p I)\tau dx + \int_{\Omega^+ \cup\, \Omega^-} u(\nabla \cdot \tau)dx + \int_{\Omega^+ \cup\, \Omega^-} \gamma\tau dx \\ = \int_{\partial\Omega^+} u\tau \cdot n ds + \int_{\partial\Omega^-} u\tau \cdot n ds\end{aligned}$$

Remark 5. *We assume that g_σ and g_q are both equal to zero in this research.*

The boundary $\partial\Omega^+$ is partitioned into $\partial\Omega^+_D$, $\partial\Omega^+_N$ and $\mathcal{C}$. By applying the boundary conditions in (3.28) the result is:

$$\begin{aligned}\int_{\partial\Omega^+} u\tau \cdot n ds = \int_{\partial\Omega^+_D} u\tau \cdot n ds + \int_{\partial\Omega^+_N} u\tau \cdot n ds + \int_{\mathcal{C}} u\tau \cdot n^+ ds \\ = \int_{\partial\Omega^+_D} g_u\tau \cdot n ds + \int_{\mathcal{C}} u\tau \cdot n^+ ds\end{aligned}$$

Applying the same approach to the boundary $\partial\Omega^-$, a similar result is achieved. Combining the result gives the following results for the boundary terms:

$$\int_{\partial\Omega_D} g_u\tau \cdot n ds \int_{\mathcal{C}} (u^+ - u^-)\tau \cdot n ds = \int_{\partial\Omega_D} g_u\tau \cdot n ds + \int_{\mathcal{C}} [u]\tau \cdot n ds$$

Note that the jump of the displacement $[u]$ on $\mathcal{C}$ is denoted $[\chi]$, resulting in the following:

$$\begin{aligned}\int_{\Omega^+ \cup\, \Omega^-} A(\sigma + \alpha p I)\tau dx + \int_{\Omega^+ \cup\, \Omega^-} u(\nabla \cdot \tau)dx + \int_{\Omega^+ \cup\, \Omega^-} \gamma\tau dx \\ = \int_{\partial\Omega_D} g_u\tau \cdot n ds + \int_{\mathcal{C}} [\chi]\tau \cdot n ds\end{aligned}$$

The first equation of our system, written on the mixed weak form, is expressed as follows:

$$(A(\sigma + \alpha p I), \tau) + (u, \nabla \cdot \tau) + (\gamma, \tau) = ([\chi], \tau n)_{\mathcal{C}} + \langle g_u, \tau n\rangle_{\Gamma_D^{\text{disp}}} \tag{4.1}$$

Next, the first flow equation in the reservoir matrix is considered:

$$K^{-1}q + \nabla p = 0$$

Again the equation is multiplied by the test function z and integrated over Ω^+:

$$\int_{\Omega^+} K^{-1}qzdx + \int_{\Omega^+} \nabla p \cdot zdx = \int_{\Omega^+} K^{-1}qzdx - \int_{\Omega^+} p\nabla \cdot zdx + \int_{\partial\Omega^+} pz \cdot nds$$

The boundary $\partial\Omega^+$ is again divided into $\partial\Omega^+_D$, $\partial\Omega^+_N$ and $\mathcal{C}$. Incorporating the boundary conditions in (3.29), we obtain:

$$\begin{aligned}\int_{\partial\Omega^+} pz \cdot nds = \int_{\mathcal{C}} pz \cdot n^+ds + \int_{\partial\Omega^+_D} pz \cdot nds + \int_{\partial\Omega^+_N} pz \cdot nds \\ = \int_{\mathcal{C}} pz \cdot n^+ds + \int_{\partial\Omega^+_D} g_pz \cdot nds\end{aligned}$$

These together results in the following:

$$\begin{aligned}&\int_{\Omega^+} K^{-1}qzdx + \int_{\Omega^+} \nabla p \cdot zdx \\ &\qquad = \int_{\Omega^+} K^{-1}qzdx - \int_{\Omega^+} p\nabla \cdot zdx + \int_{\mathcal{C}} pz \cdot n^+ds + \int_{\partial\Omega^+_D} g_pz \cdot nds\end{aligned}$$

Doing the same over Ω^- the following result is achieved:

$$\begin{aligned}&\int_{\Omega^-} K^{-1}qzdx + \int_{\Omega^-} \nabla p \cdot zdx \\ &\qquad = \int_{\Omega^-} K^{-1}qzdx - \int_{\Omega^-} p\nabla \cdot zdx + \int_{\mathcal{C}} pz \cdot n^-ds + \int_{\partial\Omega^-_D} g_pz \cdot nds\end{aligned}$$

Combining the two results over Ω^+ and over Ω^- gives the following result:

$$\int_{\Omega^+\cup\,\Omega^-} K^{-1}qzdx - \int_{\Omega^+\cup\,\Omega^-} p\nabla \cdot zdx + \int_{\mathcal{C}} p_c[z] \cdot n^+ds = -\int_{\partial\Omega_D} g_pz \cdot nds$$

The first flow equation in the reservoir matrix, expressed in the mixed weak form, can be written as follows:

$$(K^{-1}q, z) - (p, \nabla \cdot z) + (p_c, [z]_{\mathcal{C}} \cdot n^+)_{\mathcal{C}} = -\langle g_p, z \cdot n\rangle_{\Gamma^{\text{pres}}_D} \tag{4.2}$$

We then consider the second flow equation within the reservoir matrix:

$$\frac{\partial}{\partial t}(c_0 p + \alpha \mathrm{tr} A(\sigma + \alpha p I)) + \nabla \cdot q = f_2$$

Multiplying by the test function θ, and integrating over Ω^+, we obtain:

$$\int_{\Omega^+} \frac{\partial}{\partial t}(c_0 p + \alpha \mathrm{tr} A(\sigma + \alpha p I))\theta dx + \int_{\Omega^+} \nabla \cdot q\theta dx = \int_{\Omega^+} f_2 \theta dx$$

$$\int_{\Omega^+} c_0 \partial_t p \theta dx + \int_{\Omega^+} \alpha \partial_t \mathrm{tr} A(\sigma + \alpha p I)\theta dx + \int_{\Omega^+} \nabla \cdot q\theta dx = \int_{\Omega^+} f_2 \theta dx$$

Doing the same over Ω^- and combining the results for Ω^+ and Ω^- gives:

$$\int_{\Omega^+ \cup \Omega^-} c_0 \partial_t p \theta dx + \int_{\Omega^+ \cup \Omega^-} \alpha \partial_t \mathrm{tr} A(\sigma + \alpha p I)\theta dx + \int_{\Omega^+ \cup \Omega^-} \nabla \cdot q\theta dx = \int_{\Omega^+ \cup \Omega^-} f_2 \theta dx$$

Remark 6. *For the mixed variational formulation the identity* $(trAx, w) = (Ax, wI)$ *is used.*

The second flow equation in the reservoir matrix, written on the mixed weak form, reads as follows:

$$(c_0 \partial_t p, \theta) + \alpha(\partial_t A(\sigma + \alpha p I), \theta I) + (\nabla \cdot q, \theta) = (f_2, \theta) \tag{4.3}$$

Furthermore, we consider the balance of linear momentum:

$$\nabla \cdot \sigma = -f_1$$

We multiply by the test function v and integrate over Ω^+ and Ω^-:

$$\int_{\Omega^+} \nabla \cdot \sigma v dx = \int_{\Omega^+} -f_1 v dx \quad \text{and} \quad \int_{\Omega^-} \nabla \cdot \sigma v dx = \int_{\Omega^-} -f_1 v dx$$

Combining the two results of Ω^+ and Ω^- gives:

$$\int_{\Omega^+ \cup \Omega^-} \nabla \cdot \sigma v dx = \int_{\Omega^+ \cup \Omega^-} -f_1 v dx$$

The mixed weak form of the balance of linear momentum is given by:

$$(\nabla \cdot \sigma, v) = -(f_1, v) \tag{4.4}$$

4.2.2 Variational formulation in the fracture

In this section the mixed weak formulation of the equations within the fracture are derived.

Remark 7. *It is assumed that there is no flow at the endpoints of the fracture.*

The first equation within the fracture was given by:

$$K_c^{-1} q_c + \overline{\nabla} p_c = 0$$

Multiplying by the test function z_c and integrating by parts of the $\overline{\nabla} p_c$ term over $\mathcal{C}$ gives:

$$\int_{\mathcal{C}} K_c^{-1} q_c z_c dx - \int_{\mathcal{C}} p_c \overline{\nabla} \cdot z_c dx + \int_{\partial \mathcal{C}} p_c z_c \cdot n ds = 0$$

Having no flow at the boundaries gives:

$$\int_{\mathcal{C}} K_c^{-1} q_c z_c dx - \int_{\mathcal{C}} p_c \overline{\nabla} \cdot z_c dx = 0$$

The mixed weak form of the first equation within the fracture is given by:

$$(K_c^{-1} q_c, z_c)_{\mathcal{C}} - (p_c, \overline{\nabla} \cdot z_c)_{\mathcal{C}} = 0 \tag{4.5}$$

Next, we consider the second equation within the fracture:

$$\frac{\partial}{\partial t}(c_0 p_c) - \frac{\partial}{\partial t}([u] \cdot n) + \overline{\nabla} \cdot q_c = f_3 - \hat{q}_L$$

As mentioned earlier, the jump of the displacement $(u^+ - u^-)$ on $\mathcal{C}$ will be denoted by $[\chi]$. Furthermore, in the view of the jump and boundary conditions of Problem 1, q must satisfy the jump condition:

$$[q]_c \cdot n^+ = -\hat{q}_L$$

Inserting this equality, multiplying by the test function θ_c and integrating over $\mathcal{C}$ gives:

$$\int_{\mathcal{C}} c_0 \partial_t p_c \theta_c dx - \int_{\mathcal{C}} \partial_t [\chi] \cdot n^+ \theta_c dx + \int_{\mathcal{C}} \overline{\nabla} \cdot q_c \theta_c dx = \int_{\mathcal{C}} f_3 \theta_c dx + \int_{\mathcal{C}} [q]_c \cdot n^+ \theta dx$$

The second equation within the fracture, written on the mixed weak form, is given by:

$$(c_0 \partial_t p_c, \theta_c)_{\mathcal{C}} - (\partial_t [\chi] \cdot n^+, \theta_c)_{\mathcal{C}} + (\overline{\nabla} \cdot q_c, \theta_c)_{\mathcal{C}} = (f_3, \theta_c)_{\mathcal{C}} + ([q]_c \cdot n^+, \theta_c)_{\mathcal{C}} \tag{4.6}$$

Finally, by the interface condition (P1.5) and the test function v_c, we obtain:

$$(\sigma \cdot n, v_c)_{\mathcal{C}} = (-p_c n, v_c)_{\mathcal{C}} \tag{4.7}$$

4.2.3 The coupled mixed variational formulation

By combining equations (4.1) - (4.7), the mixed weak formulation for the Biot problem in the reservoir matrix coupled with the flow equations for the fracture flow can be expressed as follows:

Problem 2.
Find $(\sigma, u, \gamma, q, p, q_c, p_c, \chi) : [0,T] \to \mathbb{X} \times V \times \mathbb{Q} \times Z \times W \times Z_{\mathcal{C}} \times W_{\mathcal{C}} \times V_{\mathcal{C}}$ such that $p(0) = p_0$ and $u(0) = u_0$, and for a.e. $t \in (0,T)$

$$\forall\, \tau \in \mathbb{X}, \quad (A(\sigma + \alpha p I), \tau) + (u, \nabla \cdot \tau) + (\gamma, \tau) = ([\chi], \tau n)_{\mathcal{C}} + \langle g_u, \tau n \rangle_{\Gamma_D^{\text{disp}}} \tag{P2.1}$$

$$\forall\, v \in V, \quad (\nabla \cdot \sigma, v) = -(f_1, v) \tag{P2.2}$$

$$\forall\, \xi \in \mathbb{Q}, \quad (\sigma, \xi) = 0 \tag{P2.3}$$

$$\forall\, z \in Z, \quad (K^{-1} q, z) - (p, \nabla \cdot z) + (p_c, [z]_{\mathcal{C}} \cdot n^+)_{\mathcal{C}} = -\langle g_p, z \cdot n \rangle_{\Gamma_D^{\text{pres}}} \tag{P2.4}$$

$$\forall\, \theta \in W, \quad (c_0 \partial_t p, \theta) + \alpha(\partial_t A(\sigma + \alpha p I), \theta I) + (\nabla \cdot q, \theta) = (f_2, \theta) \tag{P2.5}$$

$$\forall\, z_c \in Z_{\mathcal{C}}, \quad (K_c^{-1} q_c, z_c)_{\mathcal{C}} - (p_c, \overline{\nabla} \cdot z_c)_{\mathcal{C}} = 0 \tag{P2.6}$$

$$\forall\, \theta_c \in W_c, \quad (c_0 \partial_t p_c, \theta_c)_{\mathcal{C}} - (\partial_t [\chi] \cdot n^+, \theta_c)_{\mathcal{C}} + (\overline{\nabla} \cdot q_c, \theta_c)_{\mathcal{C}} = (f_3, \theta_c)_{\mathcal{C}} + ([q]_c \cdot n^+, \theta_c)_{\mathcal{C}} \tag{P2.7}$$

$$\forall\, v_c \in V_{\mathcal{C}}, \quad (\sigma \cdot n, v_c)_{\mathcal{C}} = (-p_c n, v_c)_{\mathcal{C}} \tag{P2.8}$$

To simplify the notation, the spaces related to the fracture, $\mathcal{C}$, are written $L^2(\mathcal{C})$, $H^{\frac{1}{2}}(\mathcal{C})$, etc., and the spaces to the reservoir are written $L^2(\Omega^+ \cup \Omega^-)$, etc. The functional spaces are defined as follows:

$$\begin{gathered}
\mathbb{X} = \{\tau \in H(\text{div}\,;\, \Omega^+ \cup \Omega^-,\, \mathbb{M}) \;:\; \tau n = 0 \text{ on } \Gamma_N^{\text{stress}}\}, \\
V = L^2(\Omega^+ \cup \Omega^-,\, \mathbb{R}^d), \qquad \mathbb{Q} = L^2(\Omega^+ \cup \Omega^-,\, \mathbb{N}), \\
Z = \{z \in H(\text{div}\,;\, \Omega^+ \cup \Omega^-, \mathbb{R}^d) \;:\; z \cdot n = 0 \text{ on } \Gamma_N^{\text{vel}}\}, \\
W = L^2(\Omega^+ \cup \Omega^-), \qquad W_{\mathcal{C}} = H^{\frac{1}{2}}(\mathcal{C}), \\
Z_{\mathcal{C}} = \{z_c \in L^2(\mathcal{C})^{d-1}\,;\, \nabla \cdot z_c \in H^{-\frac{1}{2}}(\mathcal{C})\}, \\
V_{\mathcal{C}} = L^2(\mathcal{C})
\end{gathered}$$

4.3 Stability estimates

In this section the stability bound of the mixed variational formulation (P2.1) - (P2.8) are derived. We assume that the solution exists and can be used as test functions.

Remark 8. *For the stability analysis, we assume that both g_p and g_u are equal to zero.*

The question of regularity is postponed to later discussions. We begin by giving inf-sup conditions for the continuous mixed Darcy and elasticity spaces.

From [Ambartsumyan et al., 2020b], it is known that the spaces $Z \times W$ should satisfy the following inf-sup condition:

$$\exists\, \beta_1 > 0 \text{ s.t. } \forall\, \theta \in W, \quad \sup_{0 \neq z \in Z} \frac{(\theta, \nabla \cdot z)}{\|z\|_{\text{div}}} \geq \beta_1 \|\theta\| \tag{4.8}$$

Moreover, from [Ambartsumyan et al., 2020b], it is known that the spaces $\mathbb{X} \times V \times \mathbb{Q}$ should satisfy the following inf-sup condition:

$$\exists\, \beta_2 > 0 \text{ s.t. } \forall\, v \in V, \xi \in \mathbb{Q}, \quad \sup_{0 \neq \tau \in \mathbb{X}} \frac{(v, \nabla \cdot \tau) + (\gamma, \tau)}{\|\tau\|_{\text{div}}} \geq \beta_2 (\|v\| + \|\xi\|) \tag{4.9}$$

Additionally, from the reference [Girault et al., 2018] the inf-sup condition of the pressure p_c in the fracture is derived, and it reads as follows:

$$\exists\, \beta_3 > 0 \text{ s.t. } \forall\, p_c \in H^{\frac{1}{2}}(\mathcal{C}), \quad \sup_{z \in Z} \frac{(p_c, [z]_{\mathcal{C}} \cdot n^+)_{\mathcal{C}}}{\|z\|_Z} \geq \beta_3 \|p_c\|_{H^{\frac{1}{2}}(\mathcal{C})} \tag{4.10}$$

Theorem 4.3.1. *There exists a positive constant C independent of c_0 such that the solution of (P2.1) - (P2.8) satisfies:*

$$\begin{aligned}
&\|\sigma\|_{L^\infty(0,T\,;\,H(div\,;\,\Omega))} + \|u\|_{L^\infty(0,T\,;\,L^2(\Omega))} + \|\gamma\|_{L^\infty(0,T\,;\,L^2(\Omega))} + \|q\|_{L^\infty(0,T\,;\,L^2(\Omega))} \\
&\quad + \|p\|_{L^\infty(0,T\,;\,L^2(\Omega))} + \|q_c\|_{L^\infty(0,T\,;\,L^2(\mathcal{C}))} + \|p_c\|_{L^\infty(0,T\,;\,L^2(\mathcal{C}))} + \|\chi\|_{L^\infty(0,T\,;\,L^2(\mathcal{C}))} \\
&\quad + \|\sigma\|_{L^2(0,T\,;\,H(div\,;\,\Omega))} + \|u\|_{L^2(0,T\,;\,L^2(\Omega))} + \|\gamma\|_{L^2(0,T\,;\,L^2(\Omega))} + \|q\|_{L^2(0,T\,;\,H(div\,;\,\Omega))} \\
&\quad + \|p\|_{L^2(0,T\,;\,L^2(\Omega))} + \|q_c\|_{L^2(0,T\,;\,H(div\,;\,\mathcal{C}))} + \|p_c\|_{L^2(0,T\,;\,L^2(\mathcal{C}))} + \|\chi\|_{L^2(0,T\,;\,L^2(\mathcal{C}))} \\
&\qquad \leq C(\|f_1\|_{H^1(0,T\,;\,L^2(\Omega))} + \|f_2\|_{H^1(0,T\,;\,L^2(\Omega))} + \|f_3\|_{H^1(0,T\,;\,L^2(\mathcal{C}))} \\
&\qquad\quad + \|p_0\|_{H^1(\Omega)} + \|p_{c,0}\|_{H^1(\mathcal{C})} + \|K\nabla p_0\|_{H(div\,;\,\Omega)} + \|K_c \nabla p_{c0}\|_{H(div\,;\,\mathcal{C})}
\end{aligned} \tag{4.11}$$

Proof. From the variational formulation in Problem 2 there are 8 equations with 8 unknowns. We choose:

$$\tau = \sigma, \quad v = \partial_t u, \quad \xi = \partial_t \gamma, \quad z = q, \quad \theta = p, \quad z_c = q_c, \quad \theta_c = p_c, \quad v_c = [\chi]$$

We differentiate the first equation (P2.1) and the last (P2.8) in time, and get the following results by inserting the equalities chosen above:

$$(A(\partial_t\sigma + \alpha\partial_t pI), \sigma) + (\partial_t u, \nabla \cdot \sigma) + (\partial_t \gamma, \sigma) = (\partial_t[\chi], \sigma n)_{\mathcal{C}} + \langle \partial_t g_u, \sigma n \rangle_{\Gamma_D^{\text{disp}}} \tag{4.12}$$

$$(\nabla \cdot \sigma, \partial_t u) = -(f_1, \partial_t u) \tag{4.13}$$

$$(\sigma, \partial_t \gamma) = 0 \tag{4.14}$$

$$(K^{-1}q, q) - (p, \nabla \cdot q) + (p_c, [q]_c \cdot n^+)_{\mathcal{C}} = 0 \tag{4.15}$$

$$(c_0 \partial_t p, p) + \alpha(\partial_t A(\sigma + \alpha pI), pI) + (\nabla \cdot q, p) = (f_2, p) \tag{4.16}$$

$$(K_c^{-1} q_c, q_c)_{\mathcal{C}} - (p_c, \overline{\nabla} \cdot q_c)_{\mathcal{C}} = 0 \tag{4.17}$$

$$(c_0 \partial_t p_c, p_c)_{\mathcal{C}} - (\partial_t[\chi] \cdot n^+, p_c)_{\mathcal{C}} + (\overline{\nabla} \cdot q_c, p_c)_{\mathcal{C}} = (f_3, p_c)_{\mathcal{C}} + ([q]_c \cdot n^+, p_c)_{\mathcal{C}} \tag{4.18}$$

$$(\partial_t \sigma \cdot n, [\chi])_{\mathcal{C}} = (-\partial_t p_c n, [\chi])_{\mathcal{C}} \tag{4.19}$$

We begin by considering the mechanical equations (4.12-4.14), and note that $\partial_t g_u = 0$. We change the signs in (4.13) and (4.14), and sum up the equations:

$$\begin{aligned}(A(\partial_t\sigma + \alpha\partial_t pI), \sigma) + (\partial_t u, \nabla \cdot \sigma) + (\partial_t \gamma, \sigma) - (\nabla \cdot \sigma, \partial_t u) - (\sigma, \partial_t \gamma)& \\ = (\partial_t[\chi], \sigma n)_{\mathcal{C}} + \langle \partial_t g_u, \sigma n \rangle_{\Gamma_D^{\text{disp}}} + (f_1, \partial_t u)&\end{aligned}$$

that results in:

$$(A(\partial_t\sigma + \alpha\partial_t pI), \sigma) = (\partial_t[\chi], \sigma n)_{\mathcal{C}} + (f_1, \partial_t u) \tag{4.20}$$

Similarly, by taking the flow equations within the reservoir matrix (4.15) and (4.16) and summing them gives:

$$\begin{aligned}(K^{-1}q, q) - (p, \nabla \cdot q) + (p_c, [q]_c \cdot n^+)_{\mathcal{C}} + (c_0 \partial_t p, p) + \alpha(\partial_t A(\sigma + \alpha pI), pI)& \\ + (\nabla \cdot q, p) = (f_2, p)&\end{aligned}$$

that results in:

$$\begin{aligned}c_0 \partial_t \int_\Omega p^2 dx + \int_\Omega K^{-1} q \cdot q dx + (p_c, [q]_c \cdot n^+)_{\mathcal{C}} + \alpha(\partial_t A(\sigma + \alpha pI), pI)& \\ = (f_2, p)&\end{aligned} \tag{4.21}$$

We add the mechanics equation (4.20) with the flow equation within the reservoir (4.21) and get:

$$\begin{aligned}(A(\partial_t\sigma + \alpha\partial_t pI), \sigma + \alpha pI) + c_0 \partial_t \int_\Omega p^2 dx + \int_\Omega K^{-1} q \cdot q dx + (p_c, [q]_c \cdot n^+)_{\mathcal{C}}& \\ = (\partial_t[\chi], \sigma n)_{\mathcal{C}} + (f_1, \partial_t u) + (f_2, p)&\end{aligned} \tag{4.22}$$

Furthermore, we consider the fracture flow equations (4.17-4.19) and combine them:

$$
\begin{aligned}
\|K_c^{-\frac{1}{2}}q_c\|^2 - (p_c, \nabla\cdot q_c)_{\mathcal{C}} + \frac{c_0}{2}\partial_t\|p_c\|^2 - (\partial_t[\chi]\cdot n^+, p_c)_{\mathcal{C}} + (\overline{\nabla}\cdot q_c, p_c)_{\mathcal{C}} \\
- (\partial_t\sigma\cdot n, [\chi])_{\mathcal{C}} - (\partial_t p_c, [\chi]\cdot n)_{\mathcal{C}} = (f_3, p_c)_{\mathcal{C}} + ([q]_c\cdot n^+, p_c)_{\mathcal{C}}
\end{aligned}
$$

This results in:

$$
\|K_c^{-\frac{1}{2}}q_c\|^2 + \frac{c_0}{2}\partial_t\|p_c\|^2 - (\partial_t\sigma\cdot n, [\chi])_{\mathcal{C}} = (f_3, p_c) + ([q]_c\cdot n^+, p_c)_{\mathcal{C}} \tag{4.23}
$$

Combining (4.22) and (4.23) results in:

$$
\begin{aligned}
\frac{1}{2}\partial_t\|A^{\frac{1}{2}}(\sigma+\alpha pI)\|^2 + \frac{c_0}{2}\partial_t\|p\|^2 + \|K^{-\frac{1}{2}}q\|^2 + (p_c, [q]_c\cdot n^+)_{\mathcal{C}} + \|K_c^{-\frac{1}{2}}q_c\|^2 \\
+ \frac{c_0}{2}\partial_t\|p_c\|^2 - (\partial_t\sigma\cdot n, [\chi])_{\mathcal{C}} = (f_3, p_c) + ([q]_c\cdot n^+, p_c)_{\mathcal{C}} + (\partial_t[\chi], \sigma\cdot n)_{\mathcal{C}} \\
+ (f_1, \partial_t u) + (f_2, p)
\end{aligned}
$$

that gives:

$$
\begin{aligned}
\frac{1}{2}\partial_t\|A^{\frac{1}{2}}(\sigma+\alpha pI)\|^2 + \frac{c_0}{2}\partial_t\|p\|^2 + \|K^{-\frac{1}{2}}q\|^2 + \|K_c^{-\frac{1}{2}}q_c\|^2 + \frac{c_0}{2}\partial_t\|p_c\|^2 \\
= (f_3, p_c) + (f_1, \partial_t u) + (f_2, p)
\end{aligned} \tag{4.24}
$$

Next, integrating (4.24) in time from 0 to an arbitrary $t \in (0, T]$ results in:

$$
\begin{aligned}
\frac{1}{2}[\|A^{\frac{1}{2}}(\sigma+\alpha pI)(t)\|^2 + \|c_0^{\frac{1}{2}}p(t)\|^2 + \|c_0^{\frac{1}{2}}p_c(t)\|^2] \\
+ \int_0^t \|K^{-\frac{1}{2}}q\|^2 ds + \int_0^t \|K_c^{-\frac{1}{2}}q_c\|^2 ds = \int_0^t (f_2, p) ds + \int_0^t (f_3, p_c)_{\mathcal{C}} ds \\
- \int_0^t (\partial_t f_1, u_h) ds + \frac{1}{2}\|A^{\frac{1}{2}}(\sigma+\alpha pI)(0)\|^2 + \frac{1}{2}\|c_0^{\frac{1}{2}}p(0)\|^2 \\
+ \frac{1}{2}\|c_0^{\frac{1}{2}}p_c(0)\|^2 + (f_1, u)(t) - (f_1, u)(0)
\end{aligned} \tag{4.25}
$$

From the inf-sup condition (4.8), Equation (P2.4), and assuming the boundary terms to be zero, we can establish an upper bound for $\|p\|$ as follows:

$$
\|p\| \le C \sup_{0\neq z\in Z} \frac{(p, \nabla\cdot z)}{\|z\|_{\mathrm{div}}} = C \sup_{0\neq z\in Z} \frac{(K^{-1}q, z) + (p_c, [z]_{\mathcal{C}}\cdot n^+)_{\mathcal{C}}}{\|z\|_{\mathrm{div}}}
$$

Remark 9. *For simplicity reasons, we assume for now:*

$$
\|p\| \le C\|K^{-\frac{1}{2}}q\| \tag{4.26}
$$

Similarly, by utilizing the inf-sup condition (4.9) and Equation (P2.1), we can bound $\|u\|$ and $\|\gamma\|$ as follows:

$$\|u\| + \|\gamma\| \leq C \sup_{0 \neq \tau \in \mathbb{X}} \frac{(u, \nabla \cdot \tau) + (\gamma, \tau)}{\|\tau\|_{\text{div}}} = C \sup_{0 \neq \tau \in \mathbb{X}} \frac{([\chi], \tau n)_{\mathcal{C}} - (A(\sigma + \alpha p I), \tau)}{\|\tau\|_{\text{div}}}$$

Remark 10. *For simplicity reasons, we assume for now:*

$$\|u\| + \|\gamma\| \leq C \|A^{\frac{1}{2}}(\sigma + \alpha p I)\| \tag{4.27}$$

Using the inf-sup condition (4.10), Equation (P2.4) and assuming the boundary terms to be zero, we bound $\|p_c\|$ as follows:

$$\|p_c\| =_{H^{\frac{1}{2}}(\mathcal{C})} \leq C \sup_{z \in Z} \frac{(p_c, [z]_{\mathcal{C}} \cdot n^+)_{\mathcal{C}}}{\|z\|_Z} = C \sup_{z \in Z} \frac{(p, \nabla \cdot z) - (K^{-1} q, z)}{\|z\|_Z}$$

getting the following estimate for the pressure within the fracture:

$$\|p_c\|_{H^{\frac{1}{2}}(\mathcal{C})} \leq C(\|p\|_{L^2(\Omega)} + \|K^{-1} q\|_{L^2(\Omega \setminus \mathcal{C})}) \tag{4.28}$$

Remark 11. *We assume the following bound for the mortar variable:*

$$\|\chi\|_{L^2(\mathcal{C})} \leq C \|\sigma\| \tag{4.29}$$

Additionally, by considering the mechanical equations gives the two following estimates:

$$\|\sigma\|^2 \leq C(\|p\|^2 + \epsilon_1 \|u\|^2 + \|p_c\|^2 + \frac{1}{\epsilon_1}\|f_1\|^2) \quad \text{and} \quad \|\nabla \cdot \sigma\| \leq C \|f_1\| \tag{4.30}$$

To show this we choose:

$$\tau = \sigma, \quad v = u, \quad \xi = \gamma, \quad v_c = [\chi]$$

and inserting the equalities above in (P2.1-P2.3) and (P2.8) the following results are obtained:

$$A(\sigma + \alpha p I), \sigma) + (u, \nabla \cdot \sigma) + (\gamma, \sigma) = -([\chi], \sigma n)_{\mathcal{C}} \tag{4.31}$$

$$-(\nabla \cdot \sigma, u) = (f_1, u) \tag{4.32}$$

$$(\sigma, \gamma) = 0 \tag{4.33}$$

$$-(\sigma \cdot n, [\chi])_{\mathcal{C}} = (p_c n, [\chi])_{\mathcal{C}} \tag{4.34}$$

Summing these equations gives:

$$(A\sigma, \sigma) = (p_c n, [\chi])_{\mathcal{C}} + (f_1, u) - (\alpha p I, \sigma)$$

From the coercivity condition we have the following bound:

$$(A\sigma, \sigma) \geq C_1\|\sigma\|^2$$

Furthermore, from applying first Cauchy-Schwarz and then Young's inequality gives the following bounds:

$$|(f_1, u)| \leq \|f_1\|\|u\| \leq \frac{1}{2}(\frac{1}{\epsilon_1}\|f_1\|^2 + \epsilon_1\|u\|^2)$$

$$|(\alpha p_h I, \sigma_h)| \leq \|\alpha p I\|\|\sigma\| \leq \frac{1}{2}(\frac{1}{\epsilon_2}\|\alpha p I\|^2 + \epsilon_2\|\sigma\|^2)$$

Using the bound of the mortar variable gives:

$$|(p_c n, [\chi])_{\mathcal{C}}| \leq \|p_c n\|\|[\chi]\| \leq \frac{1}{2}(\frac{1}{\epsilon_3}\|p_c n\|^2 + \epsilon_3\|[\chi]\|^2) \leq \frac{1}{2}(\frac{1}{\epsilon_3}\|p_c\|^2 + \epsilon_3 C_2^2\|\sigma\|^2)$$

Placing all the terms containing σ on the right-hand side and creating a constant containing $\alpha, n, I, \epsilon_2, \epsilon_3$ and C_2 we obtain:

$$\|\sigma\|^2 \leq C(\frac{1}{\epsilon_1}\|f_1\|^2 + \epsilon_1\|u\|^2 + \|p\|^2 + \|p_c\|^2) \tag{4.35}$$

By testing Equation (P2.2) with $v = \nabla \cdot \sigma$, we obtain the bound:

$$\|\nabla \cdot \sigma\| \leq C\|f_1\| \tag{4.36}$$

Similarly, applying Cauchy-Schwarz and then Young's inequality on Equation (4.25) gives the following bounds:

$$|(f_3, p_c)| \leq \|f_3\|\|p_c\| \leq \frac{1}{2}(\frac{1}{\epsilon_4}\|f_3\|^2 + \epsilon_4\|p_c\|^2)$$

$$|(f_2, p)| \leq \|f_2\|\|p\| \leq \frac{1}{2}(\frac{1}{\epsilon_4}\|f_2\|^2 + \epsilon_4\|p\|^2)$$

$$|(\partial_t f_1, u)| \leq \|\partial_t f_1\|\|u\| \leq \frac{1}{2}(\frac{1}{\epsilon_4}\|\partial_t f_1\|^2 + \epsilon_4\|u\|^2)$$

$$|(f_1, u)(t)| \leq \|f(t)\|\|u(t)\| \leq \frac{1}{2}(\frac{1}{\epsilon_4}\|f_1(t)\|^2 + \epsilon_4\|u(t)\|^2)$$

$$|(f_1, u)(0)| \leq \|f_1(0)\|\|u(0)\| \leq \frac{1}{2}(\|f(0)\|^2 + \|u(0)\|^2)$$

This results in:

$$\begin{aligned}
&\|A^{\frac{1}{2}}(\sigma+\alpha pI)(t)\|^2+\|c_0^{\frac{1}{2}}p(t)\|^2+\|c_0^{\frac{1}{2}}p_c(t)\|^2\\
&\qquad+2\int_0^t\|K^{-\frac{1}{2}}q\|^2ds+2\int_0^t\|K_c^{-\frac{1}{2}}q_c\|^2ds\\
&\qquad\le\epsilon_4(\|u(t)\|^2+\int_0^t(\|p\|^2+\|p_c\|^2+\|u\|^2)ds)\\
&\qquad+\frac{1}{\epsilon_4}(\|f_1(t)\|^2+\int_0^t(\|f_2\|^2+\|f_3\|^2+\|\partial_tf_1\|^2ds)\\
&\qquad+\|A^{\frac{1}{2}}(\sigma+\alpha pI)(0)\|^2+\|c_0^{\frac{1}{2}}p(0)\|^2+\|c_0^{\frac{1}{2}}p_c(0)\|^2\\
&\qquad\qquad+\|u(0)\|^2+\|f_1(0)\|^2 \qquad (4.37)
\end{aligned}$$

By using the inf-sup condition (4.27) and denoting the initial terms as a constant C_3 we get:

$$\begin{aligned}
&C\|u(t)\|^2+c_0\|p(t)\|^2+c_0\|p_c(t)\|^2\\
&\qquad+2\int_0^t\|K^{-\frac{1}{2}}q\|^2ds+2\int_0^t\|K_c^{-\frac{1}{2}}q_c\|^2ds\\
&\qquad\le\epsilon_4(\|u(t)\|^2+\int_0^t(\|p\|^2+\|p_c\|^2+\|u\|^2)ds)\\
&\qquad+\frac{1}{\epsilon_4}(\|f_1(t)\|^2+\int_0^t(\|f_2\|^2+\|f_3\|^2+\|\partial_tf_1\|^2ds)+C_3 \qquad (4.38)
\end{aligned}$$

where C is a constant. We choose $\epsilon_4=\frac{C}{2}$ and remove the integral terms on the left-hand side—including q and q_c as these terms are positive—and obtain:

$$\begin{aligned}
&\frac{C}{2}\|u(t)\|^2+c_0\|p(t)\|^2+c_0\|p_c(t)\|^2\\
&\qquad\le\frac{C}{2}(\int_0^t(\|p\|^2+\|p_c\|^2+\|u\|^2)ds))\\
&\qquad+\frac{2}{C}(\int_0^t(\|f_2\|^2+\|f_3\|^2+\|\partial_tf_1\|^2ds))+C_3 \qquad (4.39)
\end{aligned}$$

We take c_0 to a minimum, and create a new constant C_4 on the left-hand side including C and c_0. The initial conditions and the known functions on the left-hand side creates another constant C_5:

$$C_4(\|u(t)\|^2+\|p(t)\|^2+\|p_c(t)\|^2)\le\frac{C}{2}(\int_0^t(\|u\|^2+\|p\|^2+\|p_c\|^2)ds)+C_5 \qquad (4.40)$$

By defining $C_6 = \frac{C}{2C_4}$ and $C_7 = \frac{C_5}{C_4}$, we obtain:

$$\|u(t)\|^2 + \|p(t)\|^2 + \|p_c(t)\|^2 \leq C_6(\int_0^t (\|u\|^2 + \|p\|^2 + \|p_c\|^2)ds) + C_7 \tag{4.41}$$

We choose:

$$Y(t) = \|y(t)\|^2 + \|p(t)\|^2 + \|p_c(t)\|^2$$

giving us:

$$Y(t) \leq C_6 \int_0^t Y(s)ds + C_7 \tag{4.42}$$

By Grönwall's lemma we have:

$$Y(t) \leq C_7 \exp{(C_6 T)} \tag{4.43}$$

with T being the final time. By considering the final time T, we can conclude that $Y(t)$ is bounded. By combining the established result and utilizing the inf-sup conditions mentioned earlier, we have proven the stability of the continuous problem. □

Chapter 5

The semi-discrete MSMFE-MFMFE method coupled with MFMFE within fracture

In this chapter the discretization of the fully mixed variational formulation of the poroelastic system with a fracture (P1.1)-(P1.8) is presented. We derive the semi-discrete scheme, establish the existence and uniqueness of the solution, and perform a stability analysis of the scheme, inspired by [Ambartsumyan et al., 2020b, Girault et al., 2018]. The discretization is based on mixed finite elements methods for elasticity and Darcy flow, with mixed finite elements for the flow in the fracture. For simplicity we assume that Ω is a polygonal. Similar to Section 2.1.3, we consider a finite element partition $\mathcal{T}_h$ of Ω that is shape-regular and quasi-uniform. In two dimensions the partition comprises triangles and/or quadrilaterals, and tetrahedra for three dimensions. For simplification, by assuming that the partition $\mathcal{T}_h$ meshes Ω^+ and Ω^-, results in the fracture $\mathcal{C}$ not crossing the element of $\mathcal{T}_h$. For any element $E \in \mathcal{T}_h$ there will exist a bijection mapping $F_E : \hat{E} \to E$ as shown in Figure 2.1. The Jacobian matrix is denoted as DF_E and its determinant as $J_E = |\det(DF_E)|$. The shape-regularity and quasi-uniformity of the grid imply:

$$\|DF_E\|_{0,\infty,\hat{E}} \sim h, \quad \|J_E\|_{0,\infty,\hat{E}} \sim h^d \quad \forall E \in \mathcal{T}_h$$

5.1 Discretization in the reservoir

The finite element spaces $\mathbb{X}_h \times V_h \times \mathbb{Q}_h$ will be the triple $(\mathcal{BDM}_1)^d \times (\mathcal{P}_0)^d \times (\mathcal{P}_0^{\text{cts}})^{d\times d,\text{ skew}}$ on simplicial elements. On quadrilateral elements this triple is given by $(\mathcal{BDM}_1)^2 \times (\mathcal{Q}_0)^2 \times (\mathcal{Q}_0^{\text{cts}})^{2\times 2,\text{ skew}}$. In these definitions, $\mathcal{P}_0$ represents the space of polynomials of total degree 0, and $\mathcal{Q}_0$ denotes the space of polynomials of degree 0 in each variable. For the flow discretization in the reservoir, $Z_h \times W_h$ is chosen to be the lowest order $\mathcal{BDM}_1 \times \mathcal{P}_0$ mixed finite element spaces. On triangle elements, the spaces in the reservoir on the reference element, as described in Section 2.1.3, are defined as follows:

$$\hat{\mathbb{X}}(\hat{E}) = (\mathcal{P}_1(\hat{E})^2)^2, \quad \hat{V}(\hat{E}) = \mathcal{P}_0(\hat{E})^2, \quad \hat{\mathbb{Q}}(\hat{E}) = \Xi(p),\ p \in \mathcal{P}_0(\hat{E})$$

with $\Xi(p)$ defined as:

$$\Xi(p) = \begin{bmatrix} 0 & p \\ -p & 0 \end{bmatrix}, \text{ for } p \in \mathbb{R}$$

Having tetrahedral elements, the definitions are similar:

$$\hat{\mathbb{X}}(\hat{E}) = (\mathcal{P}_1(\hat{E})^3)^3, \quad \hat{V}(\hat{E}) = \mathcal{P}_0(\hat{E})^3, \quad \hat{\mathbb{Q}}(\hat{E}) = \Xi(p),\ p \in \mathcal{P}_0(\hat{E})^d$$

with $\Xi(p)$ defined as follows:

$$\Xi(p) = \begin{bmatrix} 0 & -p_3 & p_2 \\ p_3 & 0 & -p_1 \\ -p_2 & p_1 & 0 \end{bmatrix}, \text{ for } p \in \mathbb{R}^3$$

On the reference simplex the spaces of the Darcy flow discretization are defined as follows:

$$\hat{Z}(\hat{E}) = \mathcal{P}_1(\hat{E})^d, \quad \hat{W}(\hat{E}) = \mathcal{P}_0(\hat{E})$$

Having quadrilateral elements, the spaces will be defined on the reference square as:

$$\hat{\mathbb{X}}(\hat{E}) = (\mathcal{P}_1(\hat{E})^2 + r\mathrm{curl}(\hat{x}^2\hat{y}) + s\ \mathrm{curl}(\hat{x}\hat{y}^2))^2 = \begin{pmatrix} \alpha_1\hat{x} + \beta_1\hat{y} + \gamma_1 + r_1\hat{x}^2 + 2s_1\hat{x}\hat{y} & \alpha_2\hat{x} + \beta_2\hat{y} + \gamma_2 - 2r_1\hat{x}\hat{y} - s_1\hat{y}^2 \\ \alpha_3\hat{x} + \beta_3\hat{y} + \gamma_3 + r_2\hat{x}^2 + 2s_2\hat{x}\hat{y} & \alpha_4\hat{x} + \beta_4\hat{y} + \gamma_4 - 2r_2\hat{x}\hat{y} - s_2\hat{y}^2 \end{pmatrix}$$

$$\hat{V}(\hat{E}) = \mathcal{P}_0(\hat{E})^d, \quad \hat{\mathbb{Q}}(\hat{E}) = \begin{bmatrix} 0 & p \\ -p & 0 \end{bmatrix}, p \in \mathcal{Q}_0(\hat{E}), \quad \hat{W}(\hat{E}) = \mathcal{P}_0(\hat{E})$$

$$\hat{Z}(\hat{E}) = \mathcal{P}_1(\hat{E})^2 + r\ \mathrm{curl}(\hat{x}^2\hat{y}) + s\ \mathrm{curl}(\hat{x}\hat{y}^2) = \begin{pmatrix} \alpha_5\hat{x} + \beta_5\hat{y} + \gamma_5 + r_3\hat{x}^2 + 2s_3\hat{x}\hat{y} \\ \alpha_6\hat{x} + \beta_6\hat{y} + \gamma_6 - 2r_3\hat{x}\hat{y} - s_3\hat{y}^2 \end{pmatrix}$$

For $\mathcal{BDM}_1$, the degrees of freedom can be chosen to be the values of the normal fluxes at any two points on each edge $\hat{e}$ of $\hat{E}$ in 2d or at any three points on each face $\hat{e}$ of $\hat{E}$ in 3d. This is similar for the normal stresses in the case $(\mathcal{BDM}_1)^d$. Motivated by the quadrature rule in [Ambartsumyan et al., 2020b], these points are chosen to be at the vertices of $\hat{e}$ for both velocity and stress spaces, as shown in Figure 5.1, inspired by [Ambartsumyan et al., 2020a].

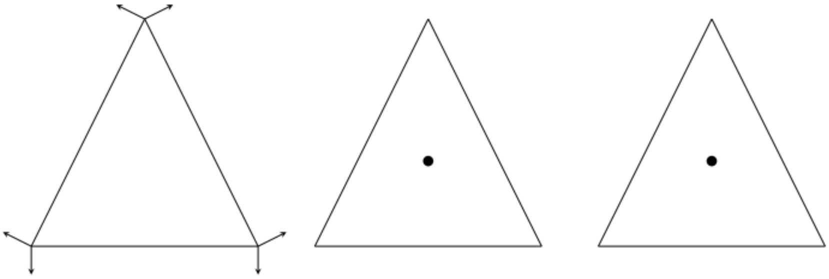

Figure 5.1: Degrees of freedom for $(\mathcal{BDM}_1)^d \times (\mathcal{P}_0)^d \times (\mathcal{P}_0)^{d\times d,\,\text{skew}}$ mixed finite elements spaces on triangles.

Via the following transformations, the above spaces can be defined on any element $E \in \mathcal{T}_h$ as:

$$\tau \overset{\mathcal{P}}{\longleftrightarrow} \hat{\tau} \,:\, \tau^T = \frac{1}{J_E} DF_E \hat{\tau}^T \circ F_E^{-1}, \quad v \leftrightarrow \hat{v} \,:\, v = \hat{v} \circ F_E^{-1}, \quad \xi \leftrightarrow \hat{\xi} \,:\, \xi = \hat{\xi} \circ F_E^{-1}$$

$$z \overset{\mathcal{P}}{\longleftrightarrow} \hat{z} \,:\, z = \frac{1}{J_E} DF_E \hat{z}^T \circ F_E^{-1}, \quad \theta \leftrightarrow \hat{\theta} \,:\, \theta = \hat{\theta} \circ F_E^{-1}$$

for $\tau \in \mathbb{X}$, $v \in V$, $\xi \in \mathbb{Q}$, $z \in Z$ and $\theta \in W$. Shown in the transformations above, the velocity vector and the stress tensor are mapped with the Piola transformation. Note that the stress is transformed row-wise. An advantage with the Piola transformation is that it is designed such that it preserves the normal components and divergence of the stress and velocity on the element edges (2D) or faces (3D) in the following sense [Girault et al., 2016]:

$$(\nabla \cdot v, w)_E = (\hat{\nabla} \cdot \hat{v}, \hat{w})_{\hat{E}}, \quad \text{and} \quad (v \cdot n_{\mathcal{C}}, w)_{\mathcal{C}} = (\hat{v} \cdot n_{\mathcal{C}}, \hat{w})_{\mathcal{C}}$$

Moreover, we have:

$$\tau n_e = \frac{1}{|J_E DF^{-T} \hat{n}_{\hat{e}}|_{\mathbb{R}^d}} \hat{\tau} \hat{n}_{\hat{e}}, \quad \text{div } \tau = \frac{1}{J_E} \text{div } \hat{\tau}$$

$$z \cdot n_e = \frac{1}{|J_E DF^{-T} \hat{n}_{\hat{e}}|_{\mathbb{R}^d}} \hat{z} \cdot \hat{n}_{\hat{e}}, \quad \text{div } z = \frac{1}{J_E} \text{div } \hat{z}$$

with $|\cdot|_{\mathbb{R}^d}$ denoting the Euclidean vector norm. With the transformations given above, the finite element spaces for the reservoir on $\mathcal{T}_h$ can be defined as follows:

$$\begin{aligned}
\mathbb{X}_h &= \{\tau \in \mathbb{X} \,:\, \tau|_E \overset{\mathcal{P}}{\longleftrightarrow} \hat{\tau},\ \hat{\tau} \in \hat{\mathbb{X}}(\hat{E}) \quad \forall\, E \in \mathcal{T}_h\}, \\
V_h &= \{v \in V \,:\, v|_E \leftrightarrow \hat{v},\ \hat{v} \in \hat{V}(\hat{E}) \quad \forall\, E \in \mathcal{T}_h\}, \\
\mathbb{Q}_h &= \{\xi \in \mathbb{Q} \,:\, \xi|_e \leftrightarrow \hat{\xi},\ \hat{\xi} \in \hat{\mathbb{Q}}(\hat{E}) \quad \forall\, E \in \mathcal{T}_h\}, \\
Z_h &= \{z \in Z \,:\, z|_E \overset{\mathcal{P}}{\longleftrightarrow} \hat{z},\ \hat{z} \in \hat{Z}(\hat{E}) \quad \forall\, E \in \mathcal{T}_h\}, \\
W_h &= \{\theta \in W \,:\, \theta|_E \leftrightarrow \hat{\theta},\ \hat{\theta} \in \hat{W}(\hat{E}) \quad \forall\, E \in \mathcal{T}_h\}
\end{aligned}$$

5.2 Discretization in the fracture

To avoid handling curved elements, we assume that the fracture $\mathcal{C}$ is a polygonal or polyhedral. As already mentioned, $\mathcal{T}_h$ is a finite element partition of Ω, and we assume that $\mathcal{T}_h$ triangulates Ω^+ and Ω^-. This choice ensures that the fracture $\mathcal{C}$ does not cross the elements of $\mathcal{T}_h$. Following the approach in [Girault et al., 2015, Girault et al., 2018], when the fracture $\mathcal{C}$ is assumed to be a polygonal or a polyhedral, each line segment or plane face of $\mathcal{C}$ can be mapped onto a segment in the x_1 line ($d = 2$) or the $x_1 - x_2$ plane when $d = 3$. This mapping is achieved by a rigid-body transformation that preserves both the surface gradient and divergence, and maps the normal n^+ into a unit vector along x_3 and whose Jacobian is one. All operations on the line segment or plane face can be treated as the same operations on the x_1 axis or the $x_1 - x_2$ plane after the change of variable. For this change in variable, particular notion is not used.

In 2D, we work with the line segments of $\mathcal{C}$ to lie on the x_1 line, while for 3D case, we work with the plane faces of $\mathcal{C}$ to lie on the $x_1 - x_2$ plane. We denote the line segments or plane faces of $\mathcal{C}$ as $\mathscr{S}i$, where $1 \le i \le I$. To simplify, we drop the index i, and take the trace of $\mathcal{T}_h$ on $\mathscr{S}$, denoted $\mathcal{T}_{\mathscr{S},h}$, as a partition of $\mathscr{S}$. We use e to represent a generic element of $\mathcal{T}_{\mathscr{S},h}$, with a corresponding reference element $\hat{e}$. The Piola transformation is defined as before, but now with respect to the element e instead of E. The finite element spaces on $\mathcal{C}$ are the same as the finite element spaces defined in [Girault et al., 2018], with the addition of a new finite element space for the mortar variable. They are defined as follows:

$$Z_{\mathcal{C},h} = \{z_c \in Z_{\mathcal{C}} \mid z_c|_{\mathscr{S}_i} \in Z_{\mathscr{S}_i,h},\ 1 \le i \le I\}$$

$$W_{\mathcal{C},h} = \{\theta_c \in L^2(\mathcal{C}) \mid \theta_c|_{\mathscr{S}_i} \in W_{\mathscr{S}_i,h},\ 1 \le i \le I\}$$

$$V_{\mathcal{C},h} = \{v_c \in L^2(\mathcal{C}) \mid v_c|_{\mathscr{S}_i} \in V_{\mathscr{S}_i,h},\ 1 \le i \le I\}$$

with:

$$Z_{\mathscr{S},h} = \{z_c \in Z_{\mathcal{C}} \mid z_c|_e \leftrightarrow \hat{z}_c,\ \hat{z}_c \in \hat{Z}_{\mathcal{C}}(\hat{e}),\ \forall\, e \in \mathcal{T}_{\mathscr{S},h}\}$$

$$W_{\mathscr{S},h} = \{\theta_c \in L^2(\mathcal{C}) \mid \theta_c|_e \leftrightarrow \hat{\theta}_c,\ \hat{\theta}_c \in \hat{W}_{\mathcal{C}}(\hat{e}),\ \forall\, e \in \mathcal{T}_{\mathscr{S},h}\}$$

$$V_{\mathscr{S},h} = \{v_c \in L^2(\mathcal{C}) \mid v_c|_e \leftrightarrow \hat{v}_c,\ \hat{v}_c \in \hat{V}_{\mathcal{C}}(\hat{e}),\ \forall\, e \in \mathcal{T}_{\mathscr{S},h}\}$$

where $\hat{Z}_{\mathcal{C}}(\hat{e})$, $\hat{W}_{\mathcal{C}}(\hat{e})$ and $\hat{V}_{\mathcal{C}}(\hat{e})$ are the finite element spaces on the reference element $\hat{e}$. The spaces $\hat{Z}_{\mathcal{C}}(\hat{e})$ and $\hat{W}_{\mathcal{C}}(\hat{e})$ are assumed to be compatible pairs [Girault et al., 2018].

5.3 The semi-discrete mixed finite element approximation

With the finite element spaces defined in Section 5.1 and Section 5.2, the semi-discrete mixed finite element approximation of the Biot problem in the reservoir coupled with a flow equation within the fracture (P2.1)-(P2.8) can be expressed as follows:

Problem 3.
Find $(\sigma_h, u_h, \gamma_h, q_h, p_h, q_{ch}, p_{ch}, \chi_h) : [0,T] \to \mathbb{X}_h \times V_h \times \mathbb{Q}_h \times Z_h \times W_h \times Z_{\mathcal{C},h} \times W_{\mathcal{C},h} \times V_{\mathcal{C},h}$ such that $p_h(0) = p_{h,0}$ and $u_h(0) = u_{h,0}$, and for a.e. $t \in (0,T)$

$\forall\, \tau \in \mathbb{X}_h,$

$$(A(\sigma_h + \alpha p_h I), \tau) + (u_h, \nabla \cdot \tau) + (\gamma_h, \tau) = ([\chi_h], \tau n)_{\mathcal{C}} + \langle g_u, \tau n \rangle_{\Gamma_D^{\text{disp}}} \tag{P3.1}$$

$$\forall\, v \in V_h, \qquad (\nabla \cdot \sigma_h, v) = -(f_1, v) \tag{P3.2}$$

$$\forall\, \xi \in \mathbb{Q}_h, \qquad (\sigma_h, \xi) = 0 \tag{P3.3}$$

$$\forall\, z \in Z_h, \qquad (K^{-1} q_h, z) - (p_h, \nabla \cdot z) + (p_{ch}, [z]_{\mathcal{C}} \cdot n^+)_{\mathcal{C}} = -\langle g_p, z \cdot n \rangle_{\Gamma_D^{\text{pres}}} \tag{P3.4}$$

$$\forall\, \theta \in W_h, \qquad (c_0 \partial_t p_h, \theta) + \alpha(\partial_t A(\sigma_h + \alpha p_h I), \theta I) + (\nabla \cdot q_h, \theta) = (f_2, \theta) \tag{P3.5}$$

$$\forall\, z_c \in Z_{\mathcal{C},h}, \qquad (K_c^{-1} q_{ch}, z_c)_{\mathcal{C}} - (p_{ch}, \overline{\nabla} \cdot z_c)_{\mathcal{C}} = 0 \tag{P3.6}$$

$\forall\, \theta_c \in W_{\mathcal{C},h},$

$$(c_0 \partial_t p_{ch}, \theta_c)_{\mathcal{C}} - (\partial_t [\chi_h] \cdot n^+, \theta_c)_{\mathcal{C}} + (\overline{\nabla} \cdot q_{ch}, \theta_c)_{\mathcal{C}} = (f_3, \theta_c)_{\mathcal{C}} + ([q_h]_c \cdot n^+, \theta_c)_{\mathcal{C}} \tag{P3.7}$$

$$\forall\, v_c \in V_{\mathcal{C},h}, \qquad (\sigma_h \cdot n, v_c)_{\mathcal{C}} = (-p_{ch} n, v_c)_{\mathcal{C}} \tag{P3.8}$$

5.4 Existence and uniqueness of the semi-discrete scheme

In this section, we establish the existence and uniqueness of the semi-discrete mixed finite element approximation of the Biot poroelasticity problem coupled with a flow problem within a fracture. Similar to the exact problem, we need inf-sup conditions to control the discrete surface variables. We begin by presenting the inf-sup conditions of the mixed Darcy and elasticity spaces, which will be utilized in the subsequent analysis. The inf-sup conditions for the mixed elasticity spaces $\mathbb{X}_h \times V_h \times \mathbb{Q}_h$ and the spaces $Z_h \times W_h$ have been studied in [Ambartsumyan et al., 2020b]. Additionally, a discrete inf-sup condition for p_{ch} has been studied in [Girault et al., 2018].

We begin by introducing the inf-sup stability of the mixed Darcy elasticity spaces. Similarly, as in Section 4.3 for the continuous case and from [Ambartsumyan et al., 2020b] it is known that the spaces $Z_h \times W_h$ satisfy the following inf-sup condition:

$$\exists\, \beta_1 > 0 \text{ s.t. } \forall\, \theta_h \in W_h, \quad \sup_{0 \neq z \in Z_h} \frac{(\theta_h, \nabla \cdot z)}{\|z\|_{\text{div}}} \geq \beta_1 \|\theta_h\| \tag{5.1}$$

For the inf-sup stability of the mixed elasticity spaces $\mathbb{X}_h \times V_h \times \mathbb{Q}_h$, the following assumptions, as outlined in [Ambartsumyan et al., 2020b], are required when considering quadrilateral elements:

(**A1**) Each element E can have at most one edge on Γ_N^{stress}.

(**A2**) The mesh size h is sufficiently small, and there exists a constant C such that for every pair of neighboring elements E and $\hat{E}$, where either E or $\hat{E}$ is a non-parallelogram, and for every pair of edges $e \subset \partial E \backslash \partial \hat{E}$ and $\hat{e} \subset \partial \hat{E} \backslash \partial E$ that share a vertex, the following condition holds:

$$|\boldsymbol{r}_e - \boldsymbol{r}_{\hat{e}}|_{\mathbb{R}^2} \leq C h^2$$

where $\boldsymbol{r}_e$ and $\boldsymbol{r}_{\hat{e}}$ are the vectors corresponding to e and $\hat{e}$, respectively.

In the case of quadrilaterals, we assume that the above-mentioned assumptions hold. From [Ambartsumyan et al., 2020b] it is known that the spaces $\mathbb{X}_h \times V_h \times \mathbb{Q}_h$ satisfy the given inf-sup condition:

$$\begin{aligned} &\exists\, \beta_2 > 0 \\ &\qquad \text{s.t. } \forall v_h \in V_h, \xi_h \in \mathbb{Q}_h, \; \sup_{0 \neq \tau \in \mathbb{X}_h} \frac{(v_h, \nabla \cdot \tau_h) + (\xi_h, \tau)_Q}{\|\tau\|_{\text{div}}} \geq \beta_2 (\|v_h\| + \|\xi_h\|) \end{aligned} \tag{5.2}$$

Furthermore, the discrete case under the assumptions given in [Ambartsumyan et al., 2020b] we have:

$$\exists\, \beta_3 > 0, \text{independent of } h, \text{ s.t. } \forall \theta_{ch} \in W_{\mathcal{C},h}, \quad \sup_{z_h \in Z_h} \frac{(\theta_{ch}, [z_h]_{\mathcal{C}})_{\mathcal{C}}}{\|z_h\|_Z} \geq \beta_3 \|\theta_{ch}\|_{L^2(\mathcal{C})|} \tag{5.3}$$

Theorem 5.4.1. *The semi-discrete method (P3.1) - (P3.8) has a unique solution.*

Proof. The proof begins by establishing two matrices, denoted as $\mathcal{N}$ and $\mathcal{M}$, such that we can rewrite our system in the form of differential-algebraic equations (DAE):

$$\mathcal{N}\frac{\partial}{\partial t}x(t) + \mathcal{M}x(t) = \mathcal{F}(t), \quad \text{a.e. } 0 < t < T \tag{5.4}$$

We consider a slightly modified version of Problem 3 with Equation (P3.1) and (P3.8) differentiated in time and with the new variables $\dot{u}_h$ and $\dot{\gamma}_h$ representing $\partial_t u_h$ and $\partial_t \gamma_h$, respectively. Recalling our assumption that the boundary terms g_u and g_p are zero, the modified problem can be expressed as follows:

$$(\partial_t A(\sigma_h + \alpha p_h I, \tau)) + (\dot{u}_h, \nabla \cdot \tau) + (\dot{\gamma}_h, \tau) - (\partial_t[\chi_h], \tau n)_{\mathcal{C}} = 0 \tag{5.5}$$

$$(\partial_t \sigma_h \cdot n, v_c) + (\partial_t p_{ch} n, v_c) = 0 \tag{5.6}$$

We introduce the following operators given in [Ambartsumyan et al., 2020b]:

$$(A_{\sigma\sigma}\sigma_h, \tau) = (A\sigma_h, \tau), \quad (A_{\sigma p}\sigma_h, \theta) = \alpha(A\sigma_h, \theta I), \quad (A_{\sigma u}\sigma_h, v) = (\text{div}\sigma_h, v),$$

$$(A_{\sigma\gamma}\sigma_h, \xi) = (\sigma_h, \xi), \quad (A_{qq}q_h, z) = (K^{-1}q_h, z), \quad (A_{qp}q_h, \theta) = -(\text{div}q_h, \theta),$$

$$(A_{pp}p_h, \theta) = (c_0 p_h, \theta) + \alpha(A\alpha p_h I, \theta I)$$

and some new operators including the fracture terms:

$$(A_{q_c q_c}q_{ch}, z_c) = (K_c^{-1}q_{ch}, z_c)_{\mathcal{C}}, \quad (A_{q_c p_c}q_{ch}, \theta_c) = -(\text{div}q_{ch}, \theta)_{\mathcal{C}},$$

$$(A_{p_c p_c}p_{ch}, \theta_c) = (c_0 p_{ch}, \theta_c)_{\mathcal{C}}, \quad (A_{qp_c}q_h, \theta_c) = ([q_h] \cdot n^+, \theta_c)_{\mathcal{C}}$$

$$(A_{\sigma\chi}\sigma_h, v_c) = (\sigma_h \cdot n, v_c)_{\mathcal{C}}, \quad (A_{p_c\chi}p_{ch}, v_c) = (p_c n, v_c)_{\mathcal{C}}$$

With these operators, the system can be expressed in the form of (5.4), where $\dot{x}$ and $\mathcal{N}$ are defined as follows:

$$\dot{x} = \begin{bmatrix} \sigma_h \\ \dot{u}_h \\ \dot{\gamma}_h \\ q_h \\ p_h \\ q_{ch} \\ p_{ch} \\ \chi_h \end{bmatrix}, \quad \mathcal{N} = \begin{bmatrix} A_{\sigma\sigma} & 0 & 0 & 0 & A_{\sigma p}^T & 0 & 0 & -A_{\sigma\chi}^T \\ 0 & 0 & 0 & 0 & 0 & 0 & 0 & 0 \\ 0 & 0 & 0 & 0 & 0 & 0 & 0 & 0 \\ 0 & 0 & 0 & 0 & 0 & 0 & 0 & 0 \\ A_{\sigma p} & 0 & 0 & 0 & A_{pp} & 0 & 0 & 0 \\ 0 & 0 & 0 & 0 & 0 & 0 & 0 & 0 \\ 0 & 0 & 0 & 0 & 0 & 0 & A_{p_c p_c} & -A_{p_c\chi}^T \\ A_{\sigma\chi} & 0 & 0 & 0 & 0 & 0 & A_{p_c\chi} & 0 \end{bmatrix},$$

and $\mathcal{M}$ and the right-hand side $\mathcal{F}$ are defined as:

$$\mathcal{M} = \begin{bmatrix} 0 & A_{\sigma u}^T & A_{\sigma\gamma}^T & 0 & 0 & 0 & 0 & 0 \\ -A_{\sigma u} & 0 & 0 & 0 & 0 & 0 & 0 & 0 \\ -A_{\sigma\gamma} & 0 & 0 & 0 & 0 & 0 & 0 & 0 \\ 0 & 0 & 0 & A_{qq} & A_{qp}^T & 0 & A_{qp_c}^T & 0 \\ 0 & 0 & 0 & -A_{qp} & 0 & 0 & 0 & 0 \\ 0 & 0 & 0 & 0 & 0 & A_{q_cq_c} & A_{q_cp_c}^T & 0 \\ 0 & 0 & 0 & -A_{qp_c} & 0 & -A_{q_cp_c} & 0 & 0 \\ 0 & 0 & 0 & 0 & 0 & 0 & 0 & 0 \end{bmatrix}, \quad \mathcal{F} = \begin{bmatrix} 0 \\ -f_1 \\ 0 \\ 0 \\ f_2 \\ 0 \\ f_3 \\ 0 \end{bmatrix}$$

From theory of DAEs, we have a unique solution of (5.4) if the matrix pencil, $s\mathcal{N} + \mathcal{M}$ is of full rank for $s \neq 0$ [Brenan et al., 1987]. Choosing $s = 1$, results in: Find $(\hat{\sigma}_h, \hat{u}_h, \hat{\gamma}_h, \hat{q}_h, \hat{p}_h, \hat{q}_{ch}, \hat{p}_{ch}, \hat{\chi}_h) \in \mathbb{X}_h \times V_h \times \mathbb{Q}_h \times Z_h \times W_h \times Z_{\mathcal{C},h} \times W_{\mathcal{C},h} \times V_{\mathcal{C},h}$ such that $\forall\ \tau \in \mathbb{X}_h,\ v \in V_h,\ \xi \in \mathbb{Q}_h,\ z \in Z_h,\ \theta \in W_h,\ z_c \in Z_{\mathcal{C},h},\ \theta_c \in W_{\mathcal{C},h}$ and $v_c \in V_{\mathcal{C},h}$

$$(A(\hat{\sigma}_h + \alpha\hat{p}_h I), \tau) + (\hat{u}_h, \nabla\cdot\tau) + (\hat{\gamma}_h, \tau) - ([\hat{\chi}_h], \tau n)_{\mathcal{C}} = 0 \tag{5.7}$$

$$(\nabla\cdot\hat{\sigma}_h, v) = 0 \tag{5.8}$$

$$(\hat{\sigma}_h, \xi) = 0 \tag{5.9}$$

$$(K^{-1}\hat{q}_h, z) - (\hat{p}_h, \nabla\cdot z) + (\hat{p}_{ch}, [z]_{\mathcal{C}}\cdot n^+) = 0 \tag{5.10}$$

$$(c_0\hat{p}_h, \theta) + \alpha(A(\hat{\sigma}_h + \alpha\hat{p}_h I), \theta I) + (\nabla\cdot\hat{q}_h, \theta) = 0 \tag{5.11}$$

$$(K_c^{-1}\hat{q}_{ch}, z_c)_{\mathcal{C}} - (\hat{p}_{ch}, \overline{\nabla}\cdot z_c)_{\mathcal{C}} = 0 \tag{5.12}$$

$$(c_0\hat{p}_{ch}, \theta_c)_{\mathcal{C}} - ([\hat{\chi}_h]\cdot n^+, \theta_c)_{\mathcal{C}} + (\overline{\nabla}\cdot\hat{q}_{ch}, \theta_c)_{\mathcal{C}} - ([\hat{q}_h]_c\cdot n^+, \theta_c)_{\mathcal{C}} = 0 \tag{5.13}$$

$$(\hat{\sigma}_h\cdot n, v_c)_{\mathcal{C}} + (\hat{p}_{ch} n, v_c)_{\mathcal{C}} = 0 \tag{5.14}$$

has only the zero solution. We choose the following:

$$\tau = \hat{\sigma}_h, \quad v = \hat{u}_h, \quad \xi = \hat{\gamma}_h, \quad z = \hat{q}_h,$$

$$\theta = \hat{p}_h, \quad z_c = \hat{q}_{ch}, \quad \theta_c = \hat{p}_{ch}, \quad v_c = [\hat{\chi}_h]$$

We insert the above equalities into Equations (5.7) - (5.14), change the signs of (5.8) and (5.9) and add the mechanics equation together, giving:

$$\begin{aligned}(A(\hat{\sigma}_h + \alpha\hat{p}_h I), \hat{\sigma}_h) + (\hat{u}_h, \nabla\cdot\hat{\sigma}_h) + (\hat{\gamma}_h, \hat{\sigma}_h) - ([\hat{\chi}_h], \hat{\sigma}_h n)_{\mathcal{C}} \\ - (\nabla\cdot\hat{\sigma}_h, \hat{u}_h) - (\hat{\sigma}_h, \hat{\gamma}_h) = 0\end{aligned}$$

This results in:

$$(A(\hat{\sigma}_h + \alpha\hat{p}_h I), \hat{\sigma}_h) - ([\hat{\chi}_h], \hat{\sigma}_h n)_{\mathcal{C}} = 0 \tag{5.15}$$

Furthermore, by combining the flow equations within the reservoir matrix (5.10) - (5.11), we obtain:

$$(K^{-1}\hat{q}_h, \hat{q}_h) - (\hat{p}_h, \nabla \cdot \hat{q}_h) + (\hat{p}_{ch}, [\hat{q}_h]_{\mathcal{C}} \cdot n^+) + (c_0\hat{p}_h, \hat{p}_h) \\ + \alpha(A(\hat{\sigma}_h + \alpha\hat{p}_h I), \hat{p}_h I) + (\nabla \cdot \hat{q}_h, \hat{p}_h) = 0$$

that results in:

$$\|K^{-\frac{1}{2}}\hat{q}_h\|^2 + (\hat{p}_{ch}, [\hat{q}_h]_{\mathcal{C}} \cdot n^+) + c_0\|\hat{p}_h\|^2 + \alpha(A(\hat{\sigma}_h + \alpha\hat{p}_h I), \hat{p}_h I) = 0 \tag{5.16}$$

We combine (5.15) and (5.16) and obtain:

$$(A(\hat{\sigma}_h + \alpha\hat{p}_h I), \alpha\hat{p}_h I + \hat{\sigma}_h) - ([\hat{\chi}_h], \hat{\sigma}_h n)_{\mathcal{C}} + \|K^{-\frac{1}{2}}\hat{q}_h\|^2 \\ + (\hat{p}_{ch}, [\hat{q}_h]_{\mathcal{C}} \cdot n^+) + c_0\|\hat{p}_h\|^2 = 0 \tag{5.17}$$

Furthermore, by considering the flow equations within the fracture (5.12)-(5.14), we add them together to obtain:

$$(K_c^{-1}\hat{q}_{ch}, \hat{q}_{ch})_{\mathcal{C}} - (\hat{p}_{ch}, \overline{\nabla} \cdot \hat{q}_{ch})_{\mathcal{C}} + (c_0\hat{p}_{ch}, \hat{p}_{ch})_{\mathcal{C}} \\ - ([\hat{\chi}_h] \cdot n^+, \hat{p}_{ch})_{\mathcal{C}} + (\overline{\nabla} \cdot \hat{q}_{ch}, \hat{p}_{ch})_{\mathcal{C}} - ([\hat{q}_h]_c \cdot n^+, \hat{p}_{ch})_{\mathcal{C}} \\ + (\hat{\sigma}_h \cdot n, [\hat{\chi}_h])_{\mathcal{C}} + (\hat{p}_{ch} n, [\hat{\chi}_h])_{\mathcal{C}} = 0$$

This results in:

$$\|K_c^{-\frac{1}{2}}\hat{q}_{ch}\|^2 + c_0\|\hat{p}_{ch}\|^2 + (\hat{\sigma}_h \cdot n, [\hat{\chi}_h])_{\mathcal{C}} - ([\hat{q}_h]_c \cdot n^+, \hat{p}_{ch})_{\mathcal{C}} = 0 \tag{5.18}$$

By adding (5.17) and (5.18) together we get:

$$\|A(\hat{\sigma}_h + \alpha\hat{p}_h I)\|^2 + \|K^{-\frac{1}{2}}\hat{q}_h\|^2 + \|c_0^{\frac{1}{2}}\hat{p}_h\|^2 + \|K_c^{-\frac{1}{2}}\hat{q}_{ch}\|^2 + \|c_0^{\frac{1}{2}}\hat{p}_{ch}\|^2 = 0 \tag{5.19}$$

Using the positive definiteness of A, K and K_c we get $\hat{\sigma}_h + \alpha\hat{p}_h I = 0$, $\hat{q}_h = 0$ and $\hat{q}_{ch} = 0$. The Darcy inf-sup condition (5.1) implies that $\hat{p}_h = 0$, and consequently, $\hat{\sigma}_h = 0$. Applying the inf-sup condition (5.2), we find $\hat{u}_h = 0$ and $\hat{\gamma}_h = 0$. Similarly, the fracture pressure inf-sup condition (5.3) implies $\hat{p}_{ch} = 0$. The bound of the mortar value implies in $\hat{\chi}_h = 0$. Thus:

$$\hat{\sigma}_h = 0, \quad \hat{u}_h = 0, \quad \hat{\gamma}_h = 0, \quad \hat{q}_h = 0,$$

$$\hat{p}_h = 0, \quad \hat{q}_{ch} = 0, \quad \hat{p}_{ch} = 0, \quad \hat{\chi}_h = 0$$

As our problem is linear, uniqueness implies existence, thereby proving both uniqueness and existence of the solution to the semi-discrete problem. □

5.5 Stability estimates

As in the continuous case, we perform a stability analysis for the semi-discrete method, considering zero boundary conditions. We derive a stability bound for equations (P3.1) - (P3.8).

Theorem 5.5.1. *There exists a positive constant C which is independent of h and c_0, such that the solution of (P3.1) - (P3.8) satisfies:*

$$\begin{aligned}
&\|\sigma_h\|_{L^\infty(0,T\,;\,H(div\,;\,\Omega))} + \|u_h\|_{L^\infty(0,T\,;\,L^2(\Omega))} + \|\gamma_h\|_{L^\infty(0,T\,;\,L^2(\Omega))} + \|q_h\|_{L^\infty(0,T\,;\,L^2(\Omega))} \\
&+ \|p_h\|_{L^\infty(0,T\,;\,L^2(\Omega))} + \|q_{ch}\|_{L^\infty(0,T\,;\,L^2(\mathcal{C}))} + \|p_{ch}\|_{L^\infty(0,T\,;\,L^2(\mathcal{C}))} + \|\chi_h\|_{L^\infty(0,T\,;\,L^2(\mathcal{C}))} \\
&+ \|\sigma_h\|_{L^2(0,T\,;\,H(div\,;\,\Omega))} + \|u_h\|_{L^2(0,T\,;\,L^2(\Omega))} + \|\gamma_h\|_{L^2(0,T\,;\,L^2(\Omega))} + \|q_h\|_{L^2(0,T\,;\,H(div\,;\,\Omega))} \\
&+ \|p_h\|_{L^2(0,T\,;\,L^2(\Omega))} + \|q_{ch}\|_{L^2(0,T\,;\,H(div\,;\,\mathcal{C}))} + \|p_{ch}\|_{L^2(0,T\,;\,L^2(\mathcal{C}))} + \|\chi_h\|_{L^2(0,T\,;\,L^2(\mathcal{C}))} \\
&\quad \le C(\|f_1\|_{H^1(0,T\,;\,L^2(\Omega))} + \|f_2\|_{H^1(0,T\,;\,L^2(\Omega))} + \|f_3\|_{H^1(0,T\,;\,L^2(\mathcal{C}))} \\
&\quad + \|p_0\|_{H^1(\Omega)} + \|p_{c,0}\|_{H^1(\mathcal{C})} + \|K\nabla p_0\|_{H(div\,;\,\Omega)} + \|K_c\nabla p_{c0}\|_{H(div\,;\,\mathcal{C})}
\end{aligned} \tag{5.20}$$

Proof. There are 8 unknowns and 8 equations, and we carry out similar steps as in the continuous case. Again, we assume that the solution exists and use them as test functions. We choose:

$$\tau = \sigma_h, \quad v = \partial_t u_h, \quad \xi = \partial_t \gamma_h, \quad z = q_h,$$

$$\theta = p_h, \quad z_c = q_{ch}, \quad \theta_c = p_{ch}, \quad v_c = [\chi_h]$$

By substituting these equalities into Problem 3 and differentiating Equations (P3.1) and (P3.8) with respect to time, we obtain the following results:

$$(A(\partial_t\sigma_h + \alpha\partial p_h I), \sigma_h) + (\partial_t u_h, \nabla\cdot\sigma_h) + (\partial_t\gamma_h, \sigma_h) = (\partial_t[\chi_h], \sigma_h n)_{\mathcal{C}} \tag{5.21}$$

$$(\nabla\cdot\sigma_h, \partial_t u_h) = -(f_1, \partial_t u_h) \tag{5.22}$$

$$(\sigma_h, \partial_t\gamma_h) = 0 \tag{5.23}$$

$$(K^{-1}q_h, q_h) - (p_h, \nabla\cdot q_h) + (p_{ch}, [q_h]_c\cdot n^+)_{\mathcal{C}} = 0 \tag{5.24}$$

$$(c_0\partial_t p_h, p_h) + \alpha(\partial_t A(\sigma_h + \alpha p_h I), p_h I) + (\nabla\cdot q_h, p_h) = (f_2, p_h) \tag{5.25}$$

$$(K_c^{-1}q_{ch}, q_{ch})_{\mathcal{C}} - (p_{ch}, \overline{\nabla}\cdot q_{ch})_{\mathcal{C}} = 0 \tag{5.26}$$

$$(c_0\partial_t p_{ch}, p_{ch})_{\mathcal{C}} - (\partial_t[\chi_h]\cdot n^+, p_{ch})_{\mathcal{C}} + (\overline{\nabla}\cdot q_{ch}, p_{ch})_{\mathcal{C}} = (f_3, p_{ch})_{\mathcal{C}} + ([q_h]\cdot n^+, p_{ch})_{\mathcal{C}} \tag{5.27}$$

$$(\partial_t\sigma_h\cdot n, [\chi_h])_{\mathcal{C}} = (-\partial_t p_{ch} n, [\chi_h])_{\mathcal{C}} \tag{5.28}$$

Similar to Section 4.3, we consider the mechanical Equations (5.21-5.23), reverse the signs in (5.22) and (5.23), and combine them as follows:

$$\begin{aligned}
(A(\partial_t\sigma_h + \alpha\partial_t p_h I), \sigma_h) + (\partial_t u_h, \nabla\cdot\sigma_h) + (\partial_t\gamma_h, \sigma_h) - (\nabla\cdot\sigma_h, \partial_t u_h)& \\
- (\sigma_h, \partial_t\gamma_h) = (\partial_t[\chi_h], \sigma_h n)_{\mathcal{C}} + (\partial_t g_u, \sigma_h n)_{\Gamma_D^{\text{pres}}} + (f_1, \partial_t u_h)&
\end{aligned}$$

that results in:

$$(A(\partial_t\sigma_h + \alpha\partial_t p_h I), \sigma_h) = (\partial_t[\chi_h], \sigma_h n)_{\mathcal{C}} + (f_1, \partial_t u_h) \tag{5.29}$$

Furthermore, we add the flow equations within the reservoir matrix as follows:

$$\begin{aligned}(K^{-1}q_h, q_h) - (p_h, \nabla\cdot q_h) + (p_{ch}, [q_h]_c\cdot n^+)_{\mathcal{C}} + (c_0\partial_t p_h, p_h)& \\ + \alpha(\partial_t A(\sigma_h + \alpha p_h I), p_h I) + (\nabla\cdot q_h, p_h) = (f_2, p_h)&\end{aligned}$$

This gives:

$$\begin{aligned}c_0\partial_t\int_\Omega p_h^2 dx + \int_\Omega K^{-1}q_h\cdot q_h dx + (p_{ch}, [q_h]_c\cdot n^+)_{\mathcal{C}}& \\ + \alpha(\partial_t A(\sigma_h + \alpha p_h I), p_h I) = (f_2, p_h)&\end{aligned} \tag{5.30}$$

We combine the mechanics equation (5.29) and the flow equation within the reservoir matrix (5.30) and obtain:

$$\begin{aligned}(A(\partial_t\sigma_h + \alpha\partial_t p_h I), (\sigma_h + \alpha p_h I)) + c_0\partial_t\int_\Omega p_h^2 dx + \int_\Omega K^{-1}q_h\cdot q_h dx& \\ + (p_{ch}, [q_h]_c\cdot n^+)_{\mathcal{C}} = (\partial_t[\chi_h], \sigma_h n)_{\mathcal{C}} + (f_1, \partial_t u_h) + (f_2, p_h)&\end{aligned} \tag{5.31}$$

Moreover, we add the flow equations within the fracture (5.26 - 5.28) as follows:

$$\begin{aligned}\|K_c^{-\frac{1}{2}}q_{ch}\|^2 - (p_{ch}, \overline{\nabla}\cdot q_{ch})_{\mathcal{C}} - (\partial_t[\chi_h]\cdot n^+, p_{ch})_{\mathcal{C}} + \frac{c_0}{2}\partial_t\|p_{ch}\|^2& \\ + (\nabla\cdot q_{ch}, p_{ch})_{\mathcal{C}} + (\partial_t\sigma_h\cdot n, [\chi_h])_{\mathcal{C}} - (\partial_t p_{ch}, [\chi_h]\cdot n)_{\mathcal{C}}& \\ = (f_3, p_{ch})_{\mathcal{C}} + ([q_h]\cdot n^+, p_{ch})_{\mathcal{C}}&\end{aligned}$$

This results in:

$$\|K_c^{-\frac{1}{2}}q_{ch}\|^2 + \frac{c_0}{2}\partial_t\|p_{ch}\|^2 - (\partial_t\sigma_h\cdot n, [\chi_h])_{\mathcal{C}} = (f_3, p_{ch})_{\mathcal{C}} + ([q_h]\cdot n^+, p_{ch})_{\mathcal{C}} \tag{5.32}$$

By placing (5.31) and (5.32) together we obtain:

$$\begin{aligned}\frac{1}{2}\partial_t\|A^{\frac{1}{2}}(\sigma_h + \alpha p_h I)\|^2 + \frac{c_0}{2}\partial_t\|p_h\|^2 + \|K^{-\frac{1}{2}}\|^2 + (p_{ch}, [q_h]_c\cdot n^+)_{\mathcal{C}}& \\ + \|K_c^{-\frac{1}{2}}q_{ch}\|^2 + \frac{c_0}{2}\partial_t\|p_{ch}\|^2 - (\partial_t\sigma_h\cdot n, [\chi_h])_{\mathcal{C}}& \\ = (f_3, p_{ch})_{\mathcal{C}} + ([q_h]\cdot n^+, p_{ch})_{\mathcal{C}} + (\partial_t[\chi_h], \sigma_h\cdot n)_{\mathcal{C}}& \\ + (f_1, \partial_t u_h) + (f_2, p_h)&\end{aligned}$$

that gives us:

$$\frac{1}{2}\partial_t\|A^{\frac{1}{2}}(\sigma_h+\alpha p_hI)\|^2+\frac{c_0}{2}\partial_t\|p_h\|^2+\|K^{-\frac{1}{2}}q_h\|^2+\|K_c^{-\frac{1}{2}}q_{ch}\|^2+\frac{c_0}{2}\partial_t\|p_{ch}\|^2 \\ =(f_3,p_{ch})_{\mathcal{C}}+(f_1,\partial_tu_h)+(f_2,p_h) \quad (5.33)$$

Next, by integrating Equation (5.33) in time from 0 to an arbitrary $t\in[0,T)$ we obtain:

$$\frac{1}{2}\|A^{\frac{1}{2}}(\sigma_h+\alpha p_hI)(t)\|^2+\frac{c_0}{2}\|p_h(t)\|^2+\int_0^t\|K^{-\frac{1}{2}}q_h\|^2ds \\ +\int_0^t\|K_c^{-\frac{1}{2}}q_{ch}\|^2ds+\frac{c_0}{2}\|p_{ch}(t)\|^2=\int_0^t(f_3,p_{ch})_{\mathcal{C}}ds+\int_0^t(f_2,p_h)ds \\ -\int_0^t(\partial_tf_1,u_h)ds+\frac{1}{2}\|A^{\frac{1}{2}}(\sigma_h+\alpha p_hI)(0)\|^2+\frac{c_0}{2}\|p_h(0)\|^2 \\ +\frac{c_0}{2}\|p_{ch}(0)\|^2+(f_1,u_h)(t)-(f_1,u_h)(0) \quad (5.34)$$

Similarly to Section 4.3, we now consider the discrete inf-sup conditions.

Remark 12. *From the inf-sup condition (5.1), Equation (P3.4) and assuming the zero boundary terms, we assume for now that $\|p_h\|$ is bounded by:*

$$\|p_h\|\leq C\|K^{\frac{1}{2}}q_h\| \quad (5.35)$$

Remark 13. *Using the inf-sup condition (5.2) and Equation (P3.1) we assume that $\|u_h\|$ and $\|\gamma_h\|$ is bounded by:*

$$\|u_h\|+\|\gamma_h\|\leq C\|A^{\frac{1}{2}}(\sigma_h+\alpha p_hI)\| \quad (5.36)$$

Furthermore, by utilizing the inf-sup condition (5.3), Equation (P3.4), and assuming the boundary terms to be zero, we can establish an upper bound for $\|p_{ch}\|$ as follows:

$$\|p_{ch}\|\leq C(\|p_h\|_{L^2(\Omega)}+\|K^{-1}q_h\|_{L^2(\Omega\setminus\mathcal{C})}) \quad (5.37)$$

Remark 14. *The mortar variable is assumed to have the following bound:*

$$\|\chi_h\|_{L^2(\mathcal{C})}\leq C\|\sigma_h\| \quad (5.38)$$

Similarly to the continuous case, we have the following two estimates:

$$\|\sigma_h\|^2\leq C(\|p_h\|^2+\epsilon_5\|u_h\|^2+\|p_{ch}\|^2+\frac{1}{\epsilon_5}\|f_1\|^2), \quad \|\nabla\cdot\sigma_h\|\leq C\|f_1\| \quad (5.39)$$

The Cauchy-Schwarz and then Young's inequality are applied on Equation (5.34). We have the following bounds:

$$|(f_3, p_{ch})| \leq \|f_3\|\|p_{ch}\| \leq \frac{1}{2}(\frac{1}{\epsilon_6}\|f_3\|^2 + \epsilon_6\|p_{ch}\|^2)$$

$$|(f_2, p_h)| \leq \|f_2\|\|p_h\| \leq \frac{1}{2}(\frac{1}{\epsilon_6}\|f_2\|^2 + \epsilon_6\|p_h\|^2)$$

$$|(\partial_t f_1, u_h)| \leq \|\partial_t f_1\|\|u_h\| \leq \frac{1}{2}(\frac{1}{\epsilon_6}\|\partial_t f_1\|^2 + \epsilon_6\|u_h\|^2)$$

$$|(f_1, u_h)(t)| \leq \|f_1(t)\|\|u_h(t)\| \leq \frac{1}{2}(\frac{1}{\epsilon_6}\|f_1(t)\|^2 + \epsilon_6\|u_h(t)\|^2)$$

$$|(f_1, u_h)(0)| \leq \|f_1(0)\|\|u_h(0)\| \leq \frac{1}{2}(\|f_1(0)\|^2 + \|u_h(0)\|^2)$$

This gives:

$$\begin{aligned}
&\|A^{\frac{1}{2}}(\sigma_h + \alpha p_h I)(t)\|^2 + \|c_0^{\frac{1}{2}} p_h(t)\|^2 + \|c_0^{\frac{1}{2}} p_{ch}(t)\|^2 \\
&\qquad + 2\int_0^t \|K^{-\frac{1}{2}} q_h\|^2 ds + 2\int_0^t \|K_c^{-\frac{1}{2}} q_{ch}\|^2 ds \\
&\qquad \leq \epsilon_6(\|u_h(t)\|^2 + \int_0^t (\|p_{ch}\|^2 + \|p_h\|^2 + \|u_h\|^2) ds) \\
&\qquad + \frac{1}{\epsilon_6}(\|f_1(t)\|^2 + \int_0^t (\|f_3\|^2 + \|f_2\|^2 + \|\partial_t f_1\|^2) ds) \\
&\qquad + \|A^{\frac{1}{2}}(\sigma_h + \alpha p_h I)(0)\|^2 + \|c_0^{\frac{1}{2}} p_h(0)\|^2 + \|c_0^{\frac{1}{2}} p_{ch}(0)\|^2 \\
&\qquad\qquad + \|u_h(0)\|^2 + \|f_1(0)\|^2 \qquad (5.40)
\end{aligned}$$

Similarly to the stability estimates in Chapter 4, we utilize the inf-sup condition (5.36) and denote the initial terms as a constant C_8, giving:

$$\begin{aligned}
&C\|u_h(t)\|^2 + c_0\|p_h(t)\|^2 + c_0\|p_{ch}(t)\|^2 \\
&\qquad + 2\int_0^t \|K^{-\frac{1}{2}} q_h\|^2 ds + 2\int_0^t \|K_c^{-\frac{1}{2}} q_{ch}\|^2 ds \\
&\qquad \leq \epsilon_6(\|u_h(t)\|^2 + \int_0^t (\|p_{ch}\|^2 + \|p_h\|^2 + \|u_h\|^2) ds) \\
&\qquad + \frac{1}{\epsilon_6}(\|f_1(t)\|^2 + \int_0^t (\|f_3\|^2 + \|f_2\|^2 + \|\partial_t f_1\|^2) ds) + C_8 \qquad (5.41)
\end{aligned}$$

Following a similar approach as in the continuous case, by choosing $\epsilon_6 = \frac{C}{2}$, removing the integral terms on the left-hand side as they are positive, taking c_0 to be the minimum, and introducing a new constant C_9 on the left-hand side that depends on C and c_0, we obtain the following bound:

$$C_9(\|u_h(t)\|^2 + \|p_h(t)\|^2 + \|p_{ch}(t)\|^2) \\ \leq \frac{C}{2}(\int_0^t (\|p_{ch}\|^2 + \|p_h\|^2 + \|u_h\|^2) ds) + C_{10} \quad (5.42)$$

With C_{10} denoting a constant that includes the source terms and initial conditions, we can set $C_{11} = \frac{C}{2C_9}$ and $C_{12} = \frac{C_{10}}{C_9}$. Thus, we obtain the following expression:

$$\|u_h(t)\|^2 + \|p_h(t)\|^2 + \|p_{ch}(t)\|^2 \leq C_{11}(\int_0^t (\|p_{ch}\|^2 + \|p_h\|^2 + \|u_h\|^2) ds) + C_{12} \quad (5.43)$$

We choose:

$$Z(t) = |u_h(t)\|^2 + \|p_h(t)\|^2 + \|p_{ch}(t)\|^2$$

and get:

$$Z(t) \leq C_{11} \int_0^t Z(s) ds + C_{12} \quad (5.44)$$

By Grönwall's lemma we have:

$$Z(t) \leq C_{12} \exp{(C_{11} T)} \quad (5.45)$$

with T representing the final time. Similar as in Chapter 4, we can conclude that $Z(t)$ is bounded, considering T as the final time. Thus, combining this result with the previously established inf-sup conditions, we have shown stability of the semi-discrete problem. □

Chapter 6

The fully-discrete MSMFE-MFMFE method coupled with MFMFE within fracture

In this chapter we present the fully-discrete method based on the backward Euler method in time. Similarly to earlier sections, we assume that both the boundary $\partial\Omega$ and the fracture $\mathcal{C}$ consist of polygonal or polyhedral surfaces to avoid handling curved elements. First, we introduce the backward Euler in time method, followed by the presentation of the fully-discrete model for the coupled flow-geomechanics model in a fractured medium. Finally, we show the existence and uniqueness of the fully-discrete problem.

6.1 Time discretization

In a time-dependent problem, a fully-discrete system refers to a system that is discretized in both space and time. A time-dependent problem is observed on an interval $[0, T]$, with T being the final time. This interval can be partitioned into time intervals with a step size of $k = \frac{T}{N}$, where N is a positive integer representing the number of time steps. The time steps are given by $t_n = n \cdot k$ for $n \in \{1, ..., N\}$ [Cheney, 2001]. Time discretization can be carried out in several ways, where one can either discretize explicitly or implicitly. This section provides an introduction to the implicit Euler method, also known as the backward Euler method, which will be utilized in our fully-discrete method. The theory within this section is based on [Atkinson et al., 2009, Brorson, 202].

To illustrate the main idea behind the backward Euler method, we consider the time derivative given as:

$$\frac{dy}{dt} = f(t, y(t)) \tag{6.1}$$

with y being an unknown quantity that is to be determined in terms of f. In order to solve the problem numerically using the backward Euler method, we approximate the time derivative term by a finite difference scheme:

$$\frac{dy}{dt} = \frac{y^n - y^{n-1}}{k}$$

To approximate the time derivative, we employ two different values of y. This approximation is substituted into our ODE, represented by Equation (6.1), resulting in the following expression:

$$\frac{y^n - y^{n-1}}{k} = f(t^n, y^n) \tag{6.2}$$

By rearranging Equation (6.2) and finding the time derivative for step $n+1$, the backward Euler method can be expressed as follows:

$$y^{n+1} = y^n + kf(t^{n+1}, y^{n+1}) \tag{6.3}$$

The next section presents the space-time discretization for our mixed variational formulation with the shown backward Euler scheme in time.

6.2 The fully-discrete scheme

The fully-discrete mixed finite element method for the Biot problem in the reservoir, coupled with a flow equation within the fracture, can be expressed as follows, incorporating the backward Euler in time method introduced in Section 6.1:

Problem 4.

Assume that we know the solution at time t_n, resulting in $(\sigma_h^n, u_h^n, \gamma_h^n, q_h^n, p_h^n, q_{ch}^n, p_{ch}^n, \chi_h^n)$ being known. Find for $n = 0, ..., N$, $(\sigma_h^{n+1}, u_h^{n+1}, \gamma_h^{n+1}, q_h^{n+1}, p_h^{n+1}, q_{ch}^{n+1}, p_{ch}^{n+1}, \chi_h^{n+1}) \in \mathbb{X}_h \times V_h \times \mathbb{Q}_h \times Z_h \times W_h \times Z_{\mathcal{C},h} \times W_{\mathcal{C},h} \times V_{\mathcal{C},h}$ such that $\forall\, \tau_h \in \mathbb{X}_h, v_h \in V_h, \xi_h \in \mathbb{Q}_h, z_h \in Z_h, \theta_h \in W_h, c_{ch} \in Z_{\mathcal{C},h}, \theta_{ch} \in W_{\mathcal{C},h}$ and $v_{ch} \in V_{\mathcal{C},h}$:

$$\begin{aligned}(A(\sigma_h^{n+1} + \alpha p_h^{n+1} I), \tau_h) + (u_h^{n+1}, \nabla \cdot \tau_h) + (\gamma_h^{n+1}, \tau_h)& \\ = ([\chi_h^{n+1}], \tau_h n)_{\mathcal{C}} + (g_{uh}, \tau_h n)&\end{aligned} \tag{P4.1}$$

$$(\nabla \cdot \sigma_h^{n+1}, v_h) = -(f_{1_h}, v_h) \tag{P4.2}$$

$$(\sigma_h^{n+1}, \xi_h) = 0 \tag{P4.3}$$

$$(K^{-1} q_h^{n+1}, z_h) - (p_h^{n+1}, \nabla \cdot z_h) + (p_{ch}^{n+1}, [z_h]_{\mathcal{C}} \cdot n^+)_{\mathcal{C}} = -(g_{ph}, z_h \cdot n)_{\Gamma_D^{\text{pres}}} \tag{P4.4}$$

$$(c_0 \frac{1}{\Delta t} p_h^{n+1}, \theta_h) + \alpha(\frac{1}{\Delta t} A(\sigma_h^{n+1} + \alpha p_h^{n+1} I), \theta_h I) + (\nabla \cdot q_h^{n+1}, \theta_h) = (f_{2h}, \theta_h) \tag{P4.5}$$

$$(K_c^{-1} q_{ch}^{n+1}, z_{ch})_{\mathcal{C}} - (p_{ch}^{n+1}, \overline{\nabla} \cdot z_{ch})_{\mathcal{C}} = 0 \tag{P4.6}$$

$$\begin{aligned} &-(\frac{1}{\Delta t}[\chi_h^{n+1}] \cdot n^+, \theta_{ch})_{\mathcal{C}} + (c_0 \frac{1}{\Delta t} p_{ch}^{n+1}, \theta_{ch})_{\mathcal{C}} + (\overline{\nabla} \cdot q_{ch}^{n+1}, \theta_{ch})_{\mathcal{C}} \\ &\qquad = (f_{3h}, \theta_{ch})_{\mathcal{C}} + ([q_h^{n+1}]_c \cdot n^+, \theta_{ch})_{\mathcal{C}} \end{aligned} \tag{P4.7}$$

$$(\sigma_h^{n+1} \cdot n, v_{ch})_{\mathcal{C}} = (-p_{ch}^{n+1} n, v_{ch})_{\mathcal{C}} \tag{P4.8}$$

Remark 15. *Problem 4 leads to a finite dimensional linear system of equations and has a block structure. This structure consists of elasticity equations, flow in matrix equations, flow in fracture equations, and the coupling conditions. Algebraically, this can be solved in a fully implicit manner. Alternatively, iterative schemes can be employed to decompose the problem into simpler block structures. For example, these block structures can be designed such that they consist of only elasticity equations or flow equations that are decoupled from each other. It is important that such iterative schemes are designed carefully to ensure stability and robustness. Starting from [Settari and Mourits, 1994, Kim et al., 2011a, Kim et al., 2011b, Mikelić and Wheeler, 2006, Both et al., 2022] and [Storvik et al., 2021], several studies have investigated iterative schemes for the Biot equation. Further studies, including Anderson acceleration [Both et al., 2019a] and parameter optimization, have been conducted in [Both et al., 2019b, Gaspar and Rodrigo, 2017, Storvik et al., 2019] and [White et al., 2016].*

Remark 16. *For the time discretization, we have considered the same time-stepping for both the flow and mechanics equations. However, in a multi-physics problem involving elasticity and flow models, the characteristic time scales of the different physics can be quite different. This motivates the use of different time stepping schemes for flow and mechanics, known as multi-rate schemes. These schemes have been studied in work such as [Ye et al., 2020, de Hoop et al., 2020, Borregales et al., 2019, Almani and Kumar, 2022, Almani et al., 2021, Almani et al., 2020, Almani et al., 2019, Almani et al., 2017, Kumar et al., 2016] and [Almani et al., 2016].*

6.3 Existence and uniqueness of the fully-discrete scheme

In this section, we show the existence and uniqueness of the fully-discrete solution at the $(n+1)$-level.

Theorem 6.3.1. *The fully-discrete method (P4.1)-(P4.8) has a unique solution.*

Proof. We choose

$$\tau_h = \sigma_h^{n+1}, \quad v_h = u_h^{n+1}, \quad \xi_h = \gamma_h^{n+1}, \quad z_h = q_h^{n+1},$$

$$\theta_h = p_h^{n+1}, \quad z_{ch} = q_{ch}^{n+1}, \quad \theta_{ch} = p_{ch}^{n+1}, \quad v_{ch} = [\chi_h^{n+1}]$$

Since our problem is linear, uniqueness implies the existence of the solution. Therefore, our focus is on proving uniqueness. In the proof, we consider the case where the initial conditions, forcing terms, and any boundary conditions are all set to zero. We demonstrate that under these conditions, the solution is forced to be zero, establishing its uniqueness. By inserting the above equalities into our problem, we obtain:

$$(A(\sigma_h^{n+1} + \alpha p_h^{n+1} I), \sigma_h^{n+1}) + (u_h^{n+1}, \nabla \cdot \sigma_h^{n+1}) + (\gamma_h^{n+1}, \sigma_h^{n+1}) = ([\chi_h^{n+1}], \sigma_h^{n+1} n)_{\mathcal{C}} \tag{6.4}$$

$$(\nabla \cdot \sigma_h^{n+1}, u_h^{n+1}) = 0 \tag{6.5}$$

$$(\sigma_h^{n+1}, \gamma_h^{n+1}) = 0 \tag{6.6}$$

$$(K^{-1} q_h^{n+1}, q_h^{n+1}) - (p_h^{n+1}, \nabla \cdot q_h^{n+1}) + (p_{ch}^{n+1}, [q_h^{n+1}]_{\mathcal{C}} \cdot n^+)_{\mathcal{C}} = 0 \tag{6.7}$$

$$(c_0 \frac{1}{\Delta t} p_h^{n+1}, p_h^{n+1}) + \alpha(\frac{1}{\Delta t} A(\sigma_h^{n+1} + \alpha p_h^{n+1} I), p_h^{n+1} I) + (\nabla \cdot q_h^{n+1}, p_h^{n+1}) = 0 \tag{6.8}$$

$$(K_c^{-1} q_{ch}^{n+1}, q_{ch}^{n+1})_{\mathcal{C}} - (p_{ch}^{n+1}, \overline{\nabla} \cdot q_{ch}^{n+1})_{\mathcal{C}} = 0 \tag{6.9}$$

$$-(\frac{1}{\Delta t}[\chi_h^{n+1}] \cdot n^+, p_{ch}^{n+1})_{\mathcal{C}} + (c_0 \frac{1}{\Delta t} p_{ch}^{n+1}, p_{ch}^{n+1})_{\mathcal{C}} + (\overline{\nabla} \cdot q_{ch}^{n+1}, p_{ch}^{n+1})_{\mathcal{C}} = ([q_h^{n+1}]_c \cdot n^+, p_{ch}^{n+1})_{\mathcal{C}} \tag{6.10}$$

$$\frac{1}{\Delta t}(\sigma_h^{n+1} \cdot n, [\chi_h^{n+1}])_{\mathcal{C}} = \frac{1}{\Delta t}(-p_{ch}^{n+1} n, [\chi_h^{n+1}])_{\mathcal{C}} \tag{6.11}$$

We change the sign in (6.5) and (6.6) and add the mechanical equations (6.4-6.6):

$$(A(\sigma_h^{n+1} + \alpha p_h^{n+1} I), \sigma_h^{n+1}) + (u_h^{n+1}, \nabla \cdot \sigma_h^{n+1}) + (\gamma_h^{n+1}, \sigma_h^{n+1}) - (\nabla \cdot \sigma_h^{n+1}, u_h^{n+1}) - (\sigma_h^{n+1}, \gamma_h^{n+1}) = ([\chi_h^{n+1}], \sigma_h^{n+1} n)_{\mathcal{C}}$$

Dividing by Δt, we obtain the following expressions:

$$\frac{1}{\Delta t}(A(\sigma_h^{n+1}+\alpha p_h^{n+1}I),\sigma_h^{n+1}) = \frac{1}{\Delta t}([\chi_h^{n+1}],\sigma_h^{n+1}n)_{\mathcal{C}} \tag{6.12}$$

Furthermore, we combine the flow within the reservoir matrix equations (6.7-6.8) and obtain:

$$\begin{aligned}(K^{-1}q_h^{n+1},q_h^{n+1}) - (p_h^{n+1},\nabla\cdot q_h^{n+1}) + (p_{ch}^{n+1},[q_h^{n+1}]_{\mathcal{C}}\cdot n^+)_{\mathcal{C}}\\ + (c_0\frac{1}{\Delta t}p_h^{n+1},p_h^{n+1}) + \alpha(\frac{1}{\Delta t}A(\sigma_h^{n+1}+\alpha p_h^{n+1}I),p_h^{n+1}I) + (\nabla\cdot q_h^{n+1},p_h^{n+1}) = 0\end{aligned}$$

that results in:

$$\begin{aligned}(K^{-1}q_h^{n+1},q_h^{n+1}) + (p_{ch}^{n+1},[q_h^{n+1}]_{\mathcal{C}}\cdot n^+)_{\mathcal{C}} + (c_0\frac{1}{\Delta t}p_h^{n+1},p_h^{n+1})\\ + \alpha(\frac{1}{\Delta t}A(\sigma_h^{n+1}+\alpha p_h^{n+1}I),p_h^{n+1}I) = 0\end{aligned} \tag{6.13}$$

Similarly to the stability analysis in previous sections we combine (6.12) and (6.13) and get:

$$\begin{aligned}(\frac{1}{\Delta t}A(\sigma_h^{n+1}+\alpha p_h^{n+1}I),\alpha p_h^{n+1}I+\sigma_h^{n+1}) + \|K^{-\frac{1}{2}}q_h^{n+1}\|^2 + c_0\frac{1}{\Delta t}\|p_h^{n+1}\|^2\\ + (p_{ch}^{n+1},[q_h^{n+1}]_{\mathcal{C}}\cdot n^+)_{\mathcal{C}} = \frac{1}{\Delta t}([\chi_h^{n+1}],\sigma_h^{n+1}n)_{\mathcal{C}}\end{aligned} \tag{6.14}$$

Furthermore, we consider the flow equations within the fracture (6.9 - 6.11) and add them:

$$\begin{aligned}(K_c^{-1}q_{ch}^{n+1},q_{ch}^{n+1})_{\mathcal{C}} - (p_{ch}^{n+1},\overline{\nabla}\cdot q_{ch}^{n+1})_{\mathcal{C}} - (\frac{1}{\Delta t}[\chi_h^{n+1}]\cdot n^+,p_{ch}^{n+1})_{\mathcal{C}}\\ + (c_0\frac{1}{\Delta t}p_{ch}^{n+1},p_{ch}^{n+1})_{\mathcal{C}} + (\overline{\nabla}\cdot q_{ch}^{n+1},p_{ch}^{n+1})_{\mathcal{C}} + \frac{1}{\Delta t}(\sigma_h^{n+1}\cdot n,[\chi_h^{n+1}])_{\mathcal{C}}\\ = ([q_h^{n+1}]_c\cdot n^+,p_{ch}^{n+1})_{\mathcal{C}} + \frac{1}{\Delta t}(-p_{ch}^{n+1}n,[\chi_h^{n+1}])_{\mathcal{C}}\end{aligned}$$

This results in:

$$\begin{aligned}\|K_c^{-\frac{1}{2}}q_{ch}^{n+1}\|^2 + c_0\frac{1}{\Delta t}\|p_{ch}^{n+1}\|^2 + \frac{1}{\Delta t}(\sigma_h^{n+1}\cdot n,[\chi_h^{n+1}])_{\mathcal{C}}\\ - ([q_h^{n+1}]_c\cdot n^+,p_{ch}^{n+1})_{\mathcal{C}} = 0\end{aligned} \tag{6.15}$$

By combining (6.14) and (6.15), we obtain:

$$\begin{aligned}(\frac{1}{\Delta t}A(\sigma_h^{n+1}+\alpha p_h^{n+1}I),\alpha p_h^{n+1}I+\sigma_h^{n+1}) + \|K^{-\frac{1}{2}}q_h^{n+1}\|^2 + c_0\frac{1}{\Delta t}\|p_h^{n+1}\|^2\\ + \|K_c^{-\frac{1}{2}}q_{ch}^{n+1}\|^2 + c_0\frac{1}{\Delta t}\|p_{ch}^{n+1}\|^2 = 0\end{aligned} \tag{6.16}$$

Rewriting Equation (6.16), we obtain:

$$\frac{1}{\Delta t}\|A^{\frac{1}{2}}(\sigma_h^{n+1} + \alpha p_h^{n+1} I)\|^2 + \|K^{-\frac{1}{2}} q_h^{n+1}\|^2 + \frac{1}{\Delta t}\|c_0^{\frac{1}{2}} p_h^{n+1}\|^2 \\ + \|K_c^{-\frac{1}{2}} q_{ch}^{n+1}\|^2 + \frac{1}{\Delta t}\|c_0^{\frac{1}{2}} p_{ch}^{n+1}\|^2 = 0 \quad (6.17)$$

Using the positive definiteness of A, K and K_c we have that $\sigma_h^{n+1} + \alpha p_h^{n+1} I = 0$, $q_h^{n+1} = 0$ and $q_{ch}^{n+1} = 0$. The Darcy inf-sup condition (5.1) and the following bound (5.35) implies $p_h^{n+1} = 0$, and consequently $\sigma_h^{n+1} = 0$. Moreover, by considering the elasticity inf-sup condition (5.2) and the subsequent bound (5.36) we have that $u_h^{n+1} = 0$ and $\gamma_h^{n+1} = 0$. The inf-sup condition for fracture pressure (5.3) and the associated (5.37) results in $p_{ch}^{n+1} = 0$. Finally, the bound on the mortar variable (5.38) implies $\chi_h^{n+1} = 0$. Thus we have:

$$q_h^{n+1} = 0, \quad q_{ch}^{n+1} = 0, \quad p_h^{n+1} = 0, \quad \sigma_h^{n+1} = 0,$$

$$u_h^{n+1} = 0, \quad \gamma_h^{n+1} = 0, \quad p_{ch}^{n+1} = 0, \quad \chi_h^{n+1} = 0$$

This proves uniqueness and thus existence of the solution of the fully-discrete problem. □

Chapter 7

Numerical simulations

In this chapter we present code verification and results of different simulations executed in the research presented in this thesis. The implementation of a fully-discrete method using simplicial grids is already incorporated into the Porepy framework [Keilegavlen et al., 2021], specifically referring to the version dated January 14th, 2023. ParaView [Ahrens et al., 2005] was used as a visualization tool for all the visualizations. Section 7.1 covers verification of the implementation, while Section 7.2 presents three simulations of fractures within a poroelastic medium. These simulations include a single tilted fracture in a homogeneous media, multiple tilted fractures in a homogeneous media, and simulations of fractures in a layered media. The code used within this thesis can be found at: `https://github.com/solveigste/Master-thesis`.

7.1 Verification

In this section we verify the convergence of our method using a two-dimensional grid. The domain is the unit square and all the boundaries are assigned Dirichlet boundary conditions for both pressure and displacement. Additionally, we consider zero initial conditions. The analytical solutions for pressure and displacement are given as follows:

$$p_a = t\sin(\pi x)\sin(\pi y) \tag{7.1}$$

$$\boldsymbol{u}_a = \{t\sin(\pi x)y(1-y),\ t\sin(\pi y)x(1-x)\} \tag{7.2}$$

Before presenting the verification results, we specify the values of the different parameters. The simulation parameters for the convergence rates are given in Table 7.1. We use the analytical solutions (7.1) and (7.2) with the strong problem 1 to obtain the rest of the variables and the right-hand side functions. With the Lamé parameters from Table 7.1, we will employ a Poisson ratio $\nu = \frac{\lambda}{2(\lambda+\mu)} = 0.25$.

Table 7.1: Simulation parameters for convergence rates

Parameter	Symbol of parameter	Value
First Lamé parameter	λ	1
Second Lamé parameter	μ	1
Permeability	$\boldsymbol{K}$	I
Mass storativity	c_0	1
Biot-Willis constant	α	1
Final time	t_f	1
Time-step	Δt	0.1

To control the error caused by the time discretization, we constructed an analytical solution being linear in time, allowing us to observe the asymptotic convergence rate with just a single time-step. Table 7.2 shows a second-order convergence rate for both displacement and pressure. In the case of normal fluxes, we observed an order of convergence of 1.5, however, this is not supported by theoretical results. Furthermore, our numerical results with a smooth solution are consistent with the MPSA-MPFA method for poroelasticity developed by [Nordbotten and Keilegavlen, 2021]. The solutions shown in Figure 7.1 are rendered with a mesh size $h = \frac{1}{128}$, which corresponds to the last row in Table 7.2. The results in Table 7.2 and Figure 7.1 verify and document the correctness of our implementation, respectively.

Table 7.2: Numerical relative errors and convergence rates. The table below documents errors for normal fluxes on facets.

h	L_2-error in $\boldsymbol{u}$	Rate	L_2-error in p	Rate
2.5000e-01	6.1330e-02	-	4.5805e-02	-
1.2500e-01	1.4317e-02	2.0989	1.2424e-02	1.8824
6.2500e-02	4.0305e-03	1.8287	3.2828e-03	1.9201
3.1250e-02	9.8832e-04	2.0279	8.1888e-04	2.0032
1.5625e-02	2.4796e-04	1.9949	2.0539e-04	1.9953
7.8125e-03	6.1974e-05	2.0004	5.1332e-05	2.0004

h	L_2-error in $\boldsymbol{\sigma}_e \cdot \boldsymbol{n}$	Rate	L_2-error in $\boldsymbol{q} \cdot \boldsymbol{n}$	Rate
2.5000e-01	8.6752e-02	-	3.8472e-02	-
1.2500e-01	3.0946e-02	1.4872	1.2739e-02	1.5946
6.2500e-02	1.1316e-02	1.4514	4.3269e-03	1.5578
3.1250e-02	4.0320e-03	1.4888	1.4618e-03	1.5656
1.5625e-02	1.4338e-03	1.4916	5.0739e-04	1.5266
7.8125e-03	5.1022e-04	1.4907	1.7856e-04	1.5067

The solutions of u_x, u_y and p at the final time 1 are shown in Figure 7.1. Additionally, Figure 7.2 shows the results of $\|\boldsymbol{u}\|$ and p over the line from $(0, 0.5)$ to $(1, 0.5)$, compared to the analytic solution.

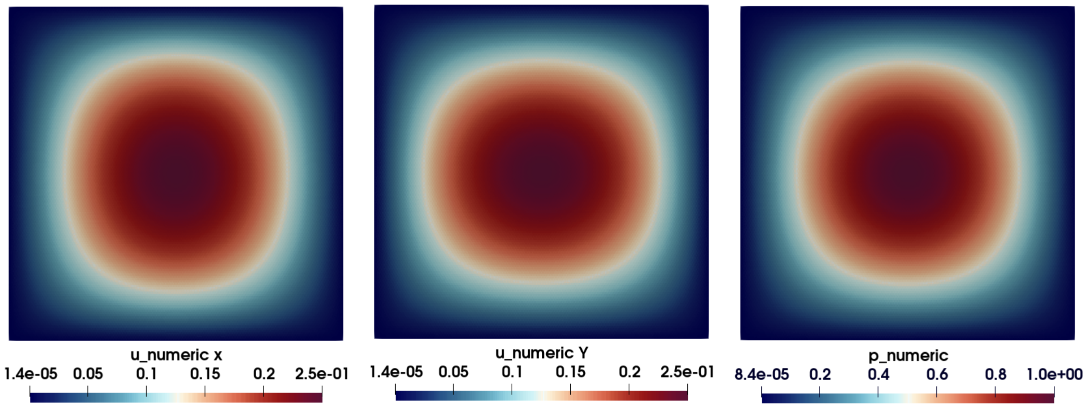

(a) u_x at the final time (b) u_y at the final time (c) p at the final time

Figure 7.1: (a) Solution of u_x at the final time. (b) Solution of u_y at the final time. (c) Solution of p at the final time.

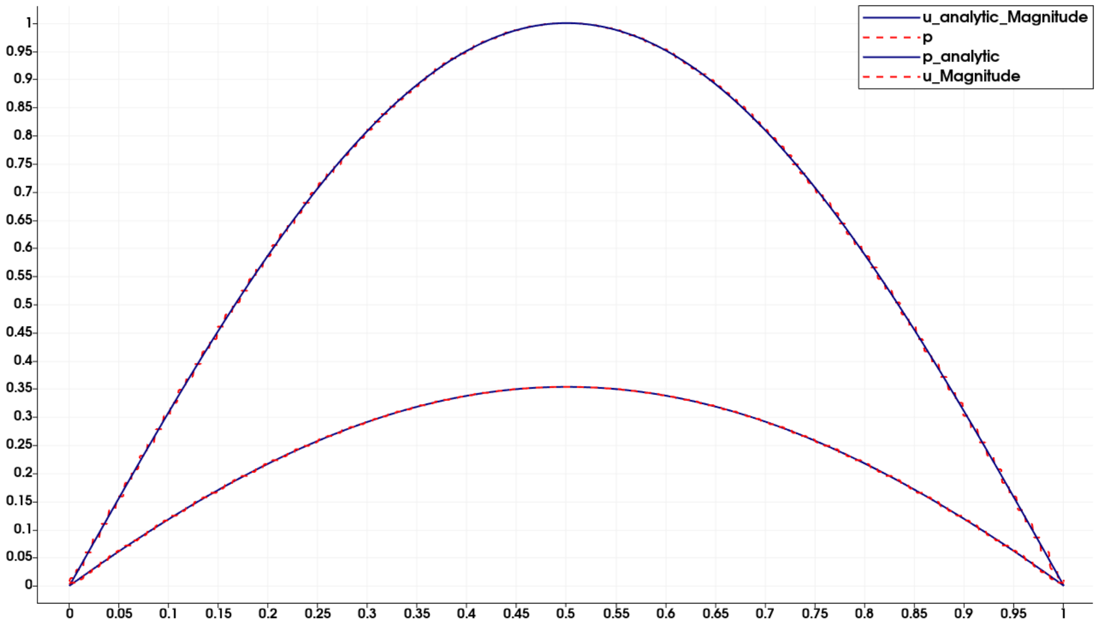

Figure 7.2: A plot over line from $(0, 0.5)$ to $(1, 0.5)$ of p and $\|\boldsymbol{u}\|$. The red dashed lines represent the numerical solutions, while the blue solid lines represent the analytical solution.

Table 7.2 presents the numerical relative errors where the permeability, Lamé parameters and Biot-Willis coefficient are constants. Additionally, we showed convergence of the method where the permeability, Lamé parameters, and the Biot-Willis coefficient are functions of x and y, given as:

$$\boldsymbol{K}(x, y) = x^2 + y^2 + 1$$

$$\lambda = x^2 + y^2 + 10, \quad \mu = x^2 + y^2 + 1$$

$$\alpha = \frac{x^2 + y^2 + 1}{4}$$

Here, we used the same values for mass storativity, final time, and time-step as provided in Table 7.1. Table 7.3 shows that the order of convergence of the displacement, pressure, stress, and flux are similar to those presented in Table 7.2. The displacement and pressure have a second-order convergence rate. Again, the normal fluxes have an order of convergence around 1.5, which aligns with the earlier numerical findings, although not supported by theoretical results. Our method is verified for cases where the permeability, Lamé parameters and the Biot-Willis coefficient are both constant and functions of both x and y. In the second case, we have not provided figures over the plot of p, u_x, u_y and the graph over lines, as these visualizations would closely resemble Figure 7.1 presented earlier.

Table 7.3: Numerical relative errors and convergence rates presented when the permeability, Lamé parameters, and the Biot-Willis coefficient are functions of x and y. The table documents the errors for normal fluxes on facets.

h	L_2-error in $\boldsymbol{u}$	Rate	L_2-error in p	Rate
2.5000e-01	8.4162e-02	-	5.3005e-02	-
1.2500e-01	1.7930e-02	2.2308	1.4806e-02	1.8399
6.2500e-02	4.4847e-03	1.9993	3.8102e-03	1.9583
3.1250e-02	1.0820e-03	2.0512	9.6155e-04	1.9864
1.5625e-02	2.6937e-04	2.0061	2.4109e-04	1.9958
7.8125e-03	6.6777e-05	2.0122	6.0251e-05	2.0005

h	L_2-error in $\boldsymbol{\sigma}_e \cdot \boldsymbol{n}$	Rate	L_2-error in $\boldsymbol{q} \cdot \boldsymbol{n}$	Rate
2.5000e-01	3.9636e-02	-	3.6205e-02	-
1.2500e-01	1.3206e-02	1.5857	1.3131e-02	1.4632
6.2500e-02	4.4872e-03	1.5573	4.7349e-03	1.4716
3.1250e-02	1.5024e-03	1.5786	1.6544e-03	1.517
1.5625e-02	5.1303e-04	1.5501	5.7530e-04	1.5239
7.8125e-03	1.7762e-04	1.5302	2.0394e-04	1.4962

7.2 Simulations

In this section we present the results of the simulated fractures in a poroelastic medium. We begin with a single tilted fracture in a homogeneous medium, followed by multiple tilted fractures in a homogeneous medium, and finally fractures in a layered medium. The first simulation is performed on a unit square domain, whereas the remaining two simulations are conducted on rectangular domains. In all simulations we label the sides of the domain as $\Gamma_1, \ldots, \Gamma_4$, starting from the bottom side and proceeding counter-clockwise. Furthermore, zero sources are considered within the fractures for all the simulations.

Example 1: A single tilted fracture in a homogeneous media

In the first simulation we compared a scenario where no fracture is present with three different angles of a fracture within the medium. The simulation parameters used in this example are listed in Table 7.4.

Table 7.4: Parameters for Simulation 1: A single tilted fracture in a homogeneous media

Parameter	Symbol	Value
First Lamé parameter	λ	10×10^9
Second Lamé parameter	μ	1×10^9
Permeability	$\boldsymbol{K}$	1×10^{-13}
Mass storativity	c_0	5×10^{-10}
Biot-Willis constant	α	1
Tangential permeability in fracture	$\boldsymbol{K}_{tc}$	1×10^{-7}
Normal permeability in fracture	$\boldsymbol{K}_{nc}$	1×10^{-7}
Final time	t_f	5000
Time-step	Δt	50

The body force f_1 and the source term f_2 are assumed to be zero. The initial conditions for displacement are set to zero, while the pressure was initialized with a value of 10.0×10^6. We enforced the boundary conditions specified in Table 7.5.

Table 7.5: Boundary conditions for Simulation 1

Boundary condition	Boundaries
$p = 0$	Γ_3
$u = (0, 0)^T$	Γ_1
$q \cdot n = 0$	$\Gamma_1 \cup \Gamma_2 \cup \Gamma_4$
$\sigma n = (0, -10.0 \times 10^6)^T$	$\Gamma_2 \cup \Gamma_3 \cup \Gamma_4$

The simulation without any fractures was performed using a mesh size of $h = 0.005$, while for simulations including fractures a finer target mesh size of $h = 0.005$ was employed near the fractures, and a coarser target mesh size of $h = 0.05$ was used near the boundaries. Figure 7.3 shows the resulting 2-dimensional grid containing a fracture tilted at an angle of 45 degrees.

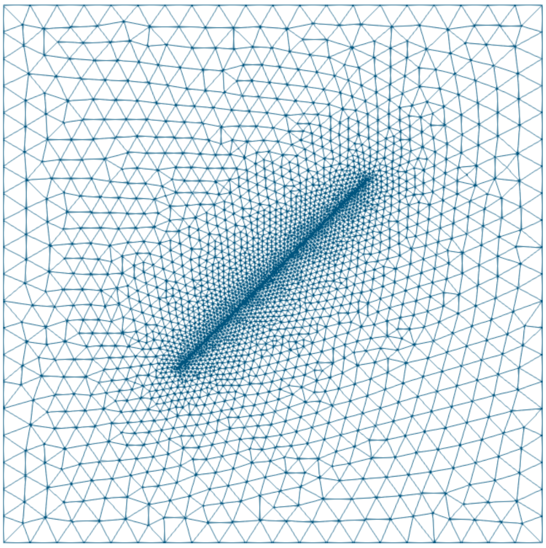

Figure 7.3: The 2-dimensional grid with a fracture tilted 45 degrees

Our objective is to compare simulations without fractures to those with fractures included at various angles. Thus, we begin by examining the pressure for different cases. Figure 7.4 displays the pressure distribution at the final time.

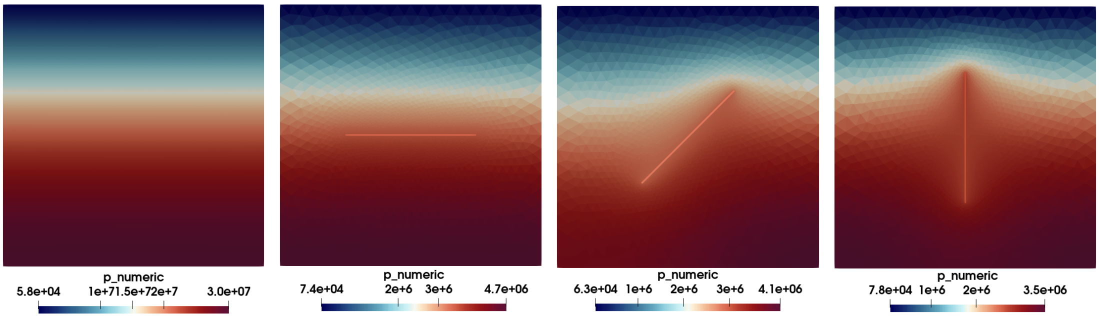

(a) No fracture (b) 0 degrees (c) 45 degrees (d) 90 degrees

Figure 7.4: (a) Pressure at final time without any fracture. (b) Pressure at the final time with a fracture tilted 0 degrees. (c) Pressure at final time with a fracture tilted 45 degrees. (d) Pressure at the final time with a fracture tilted 90 degrees.

From Figure 7.4, it is evident that there are differences in the pressure distribution among the different cases where a single fracture is embedded in the medium. Notably, in the cases involving fractures, the maximum pressure value is smaller compared to the scenario without any fracture, as indicated by the color legends. Furthermore, it can be observed that the domain with a 90-degree tilted fracture exhibits a smaller maximum pressure value compared to the domain containing a 45-degree tilted fracture. Similarly, the domain with a 45-degree tilted fracture demonstrates a smaller maximum pressure value when compared to the non-tilted fracture domain. The differences in the pressure distribution observed between the domains with a fracture embedded within the medium can be attributed to the positioning of the fracture boundaries, which are located at the endpoints of the fractures.

When comparing the case of no fracture embedded in the medium (Figure 7.4a) to the case of a non-tilted fracture (Figure 7.4b), there is minimal difference observed in the pressure distribution. At the first glance, one might assume that the lack of observable differences in the pressure distribution between the two cases is due to the relatively short duration of the simulation, as the final time is set to 5000, however, further investigations have shown that even with an extended simulation duration, the pressure distribution remains similar. The observed variations in pressure values between these two scenarios can be attributed to the higher permeability within the fracture compared to the surrounding medium, along with the slight variations in mesh size. In the case without fractures, a uniform mesh size of $h = 0.005$ was employed, whereas the tilted fractures were characterized by a boundary target mesh size of $h = 0.05$. These differences in mesh size are expected to have an impact on the overall results.

Furthermore, our investigation extends to exploring the influence of the fracture on displacement. To analyze displacement, we employed two filters in ParaView: CellDataToPointData and WarpByVector. The CellDataToPointData filter converts cell data to point data, which is necessary for the subsequent application of the WarpByVector filter. The WarpByVector filter is then applied to displace point coordinates in the input mesh using the vectors present in the dataset itself [Ahrens et al., 2005].

Figure 7.5 illustrates the displacement for a single fracture embedded in the medium and tilted at 45 degrees, while Figure 7.6 displays the displacement for a fracture tilted at 90 degrees. A scale factor of 2.67529 has been applied to scale the displacement. The black squares in the figures represents the original domain.

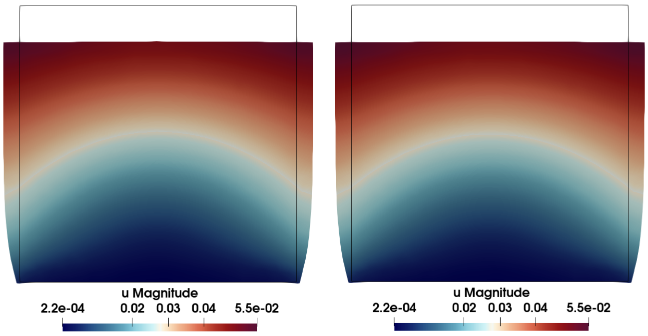

(a) First time-step (b) Final time-step

Figure 7.5: Displacement with a fracture tilted at 45 degrees within the medium.

In the case of a fracture tilted at 90 degrees, it can be observed that there is an initial opening in the fracture at the first time-step, which gradually decreases in size as the simulation progresses towards the final time-step. This phenomenon is caused by a mixed effect of the fluid and mechanics boundary conditions. Specifically, the imposition of a normal stress of $(0, -10.0 \times 10^6)^T$ at the top boundary, which aligns parallel to the 90-degree tilted fracture, is believed to contribute to this distinct behavior. Figure 7.4d demonstrates that the pressure distribution is affected by the angle of the fracture, which in turn influences the displacement. Conversely, in the case of a fracture tilted at 45 degrees, no initial opening is observed. The displacement patterns observed in the cases of no fracture and the non-tilted fracture are similar to those depicted in Figure 7.5. The presence of an opening in the 90-degree tilted fracture, which was not observed in the other fractures, can be reasonably attributed to the influence of boundary conditions.

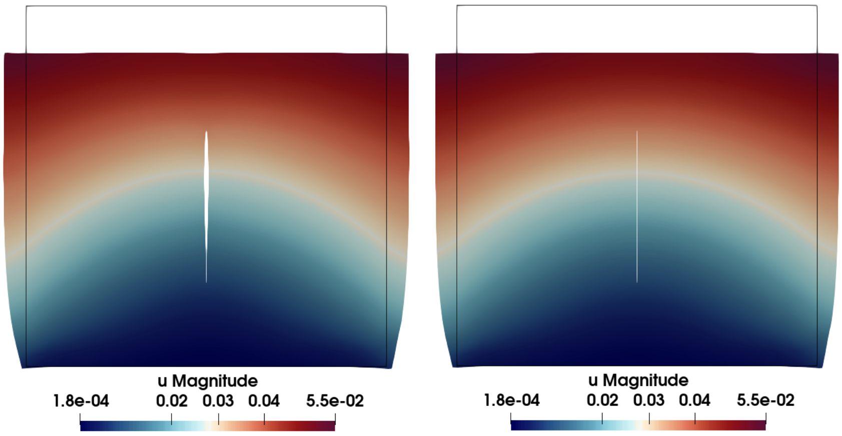

(a) First time-step (b) Final time-step

Figure 7.6: Displacement with a fracture tilted 90 degrees within the medium.

Example 2: Many tilted fractures in a homogeneous media

In the second simulation, we investigated the effect of multiple fractures with varying angles within our domain. It is important to note that during the analysis part of this thesis, we focused exclusively on studying a single fracture embedded within the reservoir matrix. The domain was given by a rectangle with $x \in [0, 100]$ and $y \in [0, 50]$. The simulation was performed using a mesh size of $h = 1.0$. Table 7.6 outlines the parameters used in this simulation. The material properties utilized represents Boise sandstone and were compiled from [Detournay and Cheng, 1993]. To ensure consistency, the permeability value was converted from milliDarcy to m^2, and the first Lamé parameter and Young's modulus were calculated based on the known terms.

Table 7.6: Parameters for Simulation 2: Many tilted fractures in a homogeneous media

Parameter	Symbol	Value
Solid bulk modulus	K_s	4.2×10^{10}
First Lamé parameter	λ	3.78×10^{10}
Second Lamé parameter	μ	4.2×10^{9}
Permeability	$\boldsymbol{K}$	7.89×10^{-13}
Young's modulus	E	1.53×10^{10}
Mass storativity	c_0	5×10^{-10}
Biot-Willis constant	α	0.85
Tangential permeability in fracture	$\boldsymbol{K}_{tc}$	1×10^{-7}
Normal permeability in fracture	$\boldsymbol{K}_{nc}$	1×10^{-15}
Final time	t_f	1000000
Time-step	Δt	10000

Similar to Simulation 1, we assumed the body force f_1 and the source term f_2 to be zero. The initial conditions for displacement was set to zero, while the pressure had an initial condition of 20.0×10^6. Furthermore, the boundary conditions of Simulation 2 are listed in Table 7.7.

Table 7.7: Boundary conditions for Simulation 2

Boundary condition	Boundaries
$p = 15 \times 10^6$	Γ_2
$p = 30 \times 10^8 + 15 \times 10^6$	Γ_4
$u = (0, 0)^T$	$\Gamma_1 \cup \Gamma_2 \cup \Gamma_4$
$q \cdot n = 0$	$\Gamma_1 \cup \Gamma_3$
$\sigma n = (0, -22.0 \times 10^6)^T$	Γ_3

The two-dimensional grid, illustrated in Figure 7.7, consists of 32 fractures embedded within the reservoir matrix. Notably, each fracture intersects with another fracture, forming pairs. Unlike Simulation 1, in this case the mesh size was homogeneous throughout the domain. To simplify the simulation analysis, we prevented the fractures from intersecting with the boundaries of the domain.

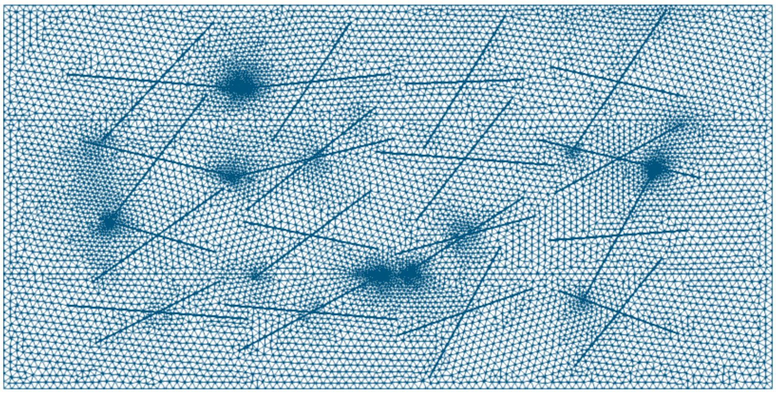

Figure 7.7: The 2-dimensional grid with 32 fractures embedded

In the analysis of the domain with multiple fractures, similar to Simulation 1, we examined both the pressure and displacement fields. Figure 7.8 presents the pressure distribution in the domain at both the first and final time-step. It is worth noting that in this simulation there is a significant difference between the tangential and normal permeability within the fractures, where the permeability in the normal direction is much smaller than in the tangential direction. This difference has a significant impact on the pressure distribution within the reservoir matrix. As a result, a non-continuous distribution of pressure is observed, with clear edges and distinct pressure values along the fractures.

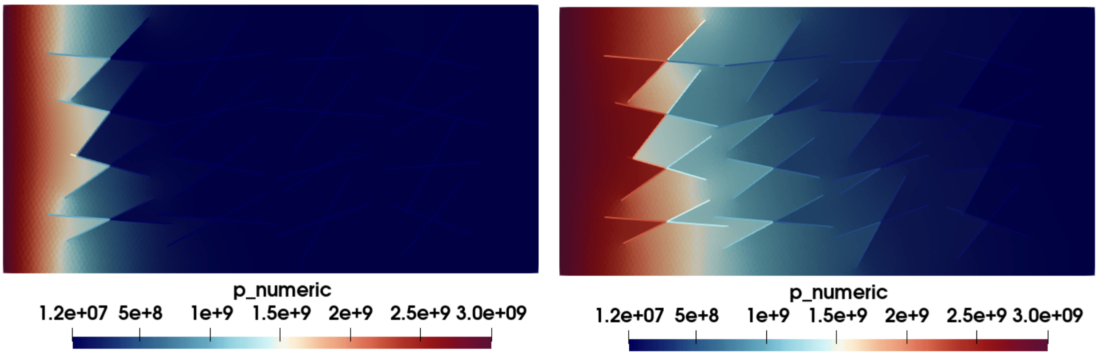

(a) First time-step

(b) Final time-step

Figure 7.8: (a) Pressure at the first time-step. (b) Pressure at the final time-step

To analyze the displacement, we have once again employed the WarpByVector filter, this time using a scale factor of 0.120396. In Figure 7.9, the black rectangle represents the original domain prior to the displacement. At the first time-step the displacement distribution is nearly uniform across the domain, with small openings observed at the fractures. However, at the final time-step there is a notable increase in displacement magnitude, particularly in the upper-left region. Additionally, the openings in the fractures appear wider in the normal direction. These observations may be attributed to a combination of factors. Firstly, the higher permeability in the tangential direction compared to the normal direction within the fractures contributes to the formation of larger openings. Additionally, the difference in permeability between the tangential direction in the fracture and the permeability in the reservoir matrix plays a role in the displacement behavior. These differences in permeability affect the flow patterns and pressure distribution, which in turn influence the displacement and opening behavior of the fractures. Furthermore, the boundary conditions imposed in the simulation also have an impact on the displacement behavior. Specifically, at the boundary Γ_4, a pressure of $30 \times 10^8 + 15 \times 10^6$ was applied, while at the boundary Γ_3, a normal stress of $(0, -22.0 \times 10^6)^T$ was imposed. These factors collectively contributes to the observed wider openings of the fractures and the displacement behavior in the domain.

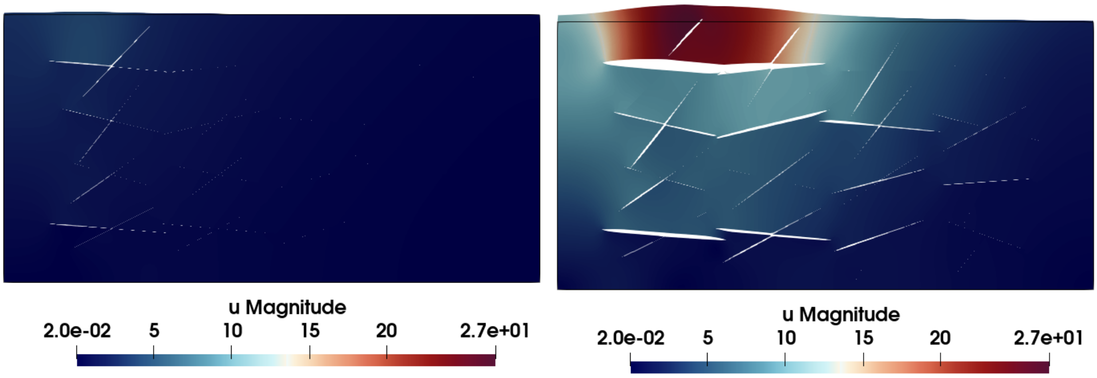

(a) First time-step (b) Final time-step

Figure 7.9: (a) Displacement at the first time-step. (b) Displacement at the final time-step

From Figure 7.8 and Figure 7.9, it is evident that the presence of fractures within the domain, along with their associated parameters, has a significant impact on both the pressure distribution and displacement. The differences in the normal and tangential permeability within the fractures influence both the pressure distribution and the displacement.

Example 3: Fractures in a layered media

In the third and final simulation, we investigated fractures in a layered poroelastic medium. Due to the varying permeability values in the layered medium, appropriate values for the Lamé parameters and the Biot-Willis coefficient corresponding to the local permeability values were necessary. In this simulation, we utilized the same rectangular domain as for Simulation 2. However, the domain now consisted of three distinct layers composed of two different materials. The first layer spanned the range of $y \in [0, 15]$, the second layer occupied the interval $y \in (15, 35)$, and the final layer covered $y \in [35, 50]$. The simulation parameters for this case are provided in Table 7.8. Material 1 corresponded to charcoal granite, while material 2 represented Boise sandstone. Both materials were compiled from [Detournay and Cheng, 1993]. Notably, material 2 used in this simulation was identical to the material employed in simulation 2. The values of the permeabilities were converted to m^2, and the first Lamé parameter and Young's modulus were calculated based on the given information.

Table 7.8: Parameters for Simulation 3: Fractures in a layered media

Parameter	Symbol	Material 1	Material 2
Solid bulk modulus	K_s	4.5×10^{10}	4.2×10^{10}
First Lamé parameter	λ	2.6×10^{10}	3.78×10^{10}
Second Lamé parameter	μ	1.9×10^{10}	4.2×10^{9}
Permeability	$\boldsymbol{K}$	9.86×10^{-20}	7.89×10^{-13}
Biot-Willis constant	α	0.27	0.85
Young's modulus	E	5.34×10^{10}	1.53×10^{10}

Parameter	Symbol	Value
Mass storativity	c_0	5×10^{-10}
Tangential permeability in fracture	$\boldsymbol{K}_{tc}$	1×10^{-7}
Normal permeability in fracture	$\boldsymbol{K}_{nc}$	1×10^{-15}
Final time	t_f	1000000
Time-step	Δt	10000

The initial and boundary conditions employed in this simulation remain consistent with those used in Simulation 2, allowing us to compare and analyze the influence of the layered medium in contrast to the results obtained in Simulation 2. For specific details regarding the boundary and interface conditions, kindly refer to Table 7.7. In this study of layered media, we considered three different cases. In the first case, material 2, which has the lowest stiffness, represents the net pay, and the fracture has a small normal permeability. In the second case, material 2 is still the net pay, but both the normal and tangential permeabilities of the fractures are equal. Finally, in the third case, the net pay has a higher stiffness than the outer layers.

Example 3.1: Net pay being the softer material

In the first example the net pay corresponds to material 2, as indicated in Table 7.8. The outer layers of the layered media represent material 1. Figure 7.10 illustrates the pressure and displacement profiles at the final time for this configuration. The original domain is still represented by the black rectangle.

The pressure distribution clearly reveals distinct layers within the material, with material 2 exhibiting significantly higher pressure compared to the outer layers. This strong contrast is caused by the substantial difference in permeability values, as the outer layers consist of a nearly impermeable material, leading to a lower pressure. Furthermore, it is evident that fluid escapes into the material with lower permeability at the fracture locations, as the fractures have higher permeability in both the tangential and normal directions compared to material 1.

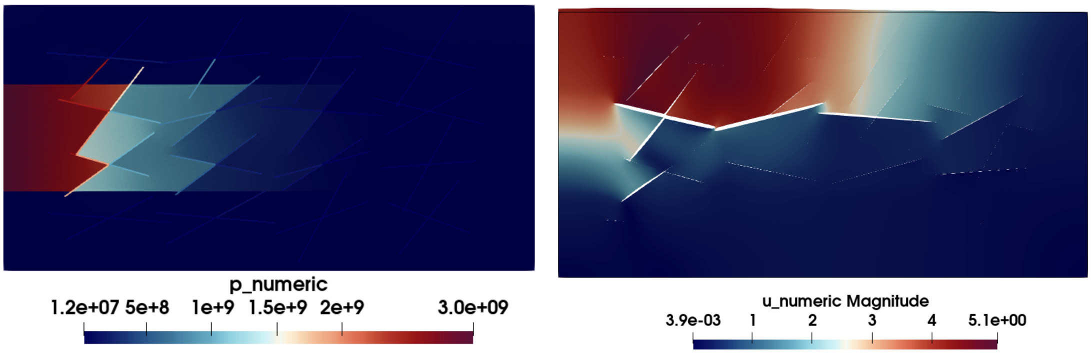

(a) Pressure at final time-step

(b) Displacement at final time-step

Figure 7.10: Net pay being equal to material 2. (a) Pressure at final time. (b) Displacement at final time

In this example, a scaling factor of 0.180576 was applied to the displacement. The displacement at the first time-step closely resembles the one presented in Simulation 2, as shown in Figure 7.9a. However, in contrast to Simulation 2, where fractures were open throughout the domain at the final time-step, particularly in the fractures of the upper-left region, the current scenario exhibits the most significant opening of fractures in the net pay. This can be observed in Figure 7.10b. This difference can be attributed to the lower stiffness of the net pay in comparison to the outer layer, as the net pay possesses the lowest Young's modulus.

Example 3.2: Equal normal and tangential permeability

In the second example of the layered media we maintain the same materials and layers as in the previous example, with the only difference being an increase in the normal permeability. Specifically, the normal permeability now matches the tangential permeability, both set to 1×10^{-7}. All other parameters remain unchanged and are listed in Table 7.8.

By comparing Figure 7.10a and Figure 7.11a, it is evident that distinct layers are still clearly visible, with higher pressure values observed in the net pay. However, in contrast to Example 3.1, the pressure distribution in the net pay now exhibits a more continuous pattern, with less pronounced differences at the fractures. This change is primarily attributed to the higher normal permeability, which enables easier fluid flow through the fractures in the normal direction compared to the previous example.

Furthermore, we can observe that the fractures located at the bottom left in both examples do not significantly affect the pressure distribution, as these fractures do not intersect with the net pay. Additionally, it is worth noting that the pressure within the remaining fractures of the outer layers are significantly higher than in the previous example, as a consequence of the increased normal permeability. These observations highlight the significant impact of normal permeability variations on the pressure distribution within the medium.

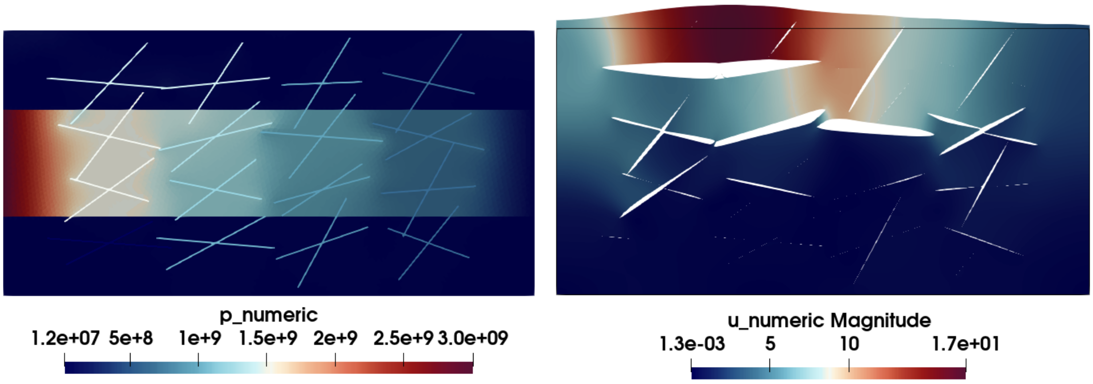

(a) Pressure at final time-step

(b) Displacement at final time-step

Figure 7.11: Net pay being equal to material 2. The normal permeability and tangential permeability in the fracture are equal to each other. (a) Pressure at final time. (b) Displacement at final time

For the displacement in this example, a scale of 0.251576 has been applied. Similar to Example 3.1, we still observe distinct openings in the net pay, which has a lower stiffness compared to the outer layers. However, in contrast to Example 3.1, we now observe clear openings of the fractures in the upper-left region, similar to the displacement pattern observed in Simulation 2. This behavior can be attributed to the higher pressure within the layer due to the increased normal permeability, as well as the utilization of boundary conditions identical to those employed in Simulation 2.

Example 3.3: Net pay being the stiffer material

In the third and final example, we have examined a scenario where the net pay represents the stiffer material. In this case, we have utilized the same parameters as in Example 3.1, with the only difference being the reversal of the Lamé parameters for the materials. It should be noted that the normal permeability remains the same as listed in Table 7.8.

By comparing the pressure distribution in Figure 7.12a to Figure 7.10a, we observe an almost identical pressure distribution in both cases, with slightly higher pressure values found in fractures that intersect the net pay. These similarities indicate that the material's stiffness has a minimal impact on the pressure distribution, whereas the permeability value demonstrates a stronger correlation.

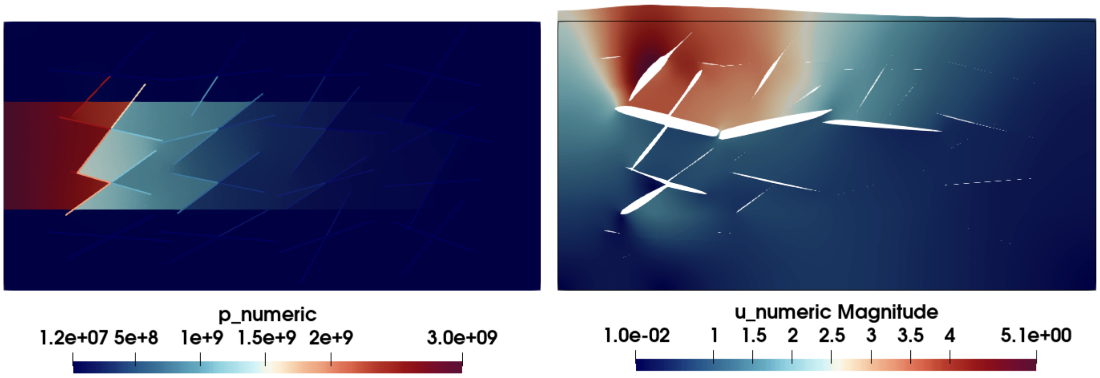

(a) Pressure at final time-step

(b) Displacement at final time-step

Figure 7.12: Net pay being the stiffer material. (a) Pressure at final time. (b) Displacement at final time

In this example a scale factor equal to 0.742465 was utilized on the displacement. When examining the displacement of the stiffer material within the net pay, it remains evident that fracture openings occur within the net pay zone. This observation highlights that the opening of fractures is influenced, not only by the material's stiffness, but also by the pressure within the layer. In contrast to Figure 7.10b, we now observe fracture openings in the upper left region as well. The presence of these openings can be attributed to the boundary conditions of the medium, combined with the lower stiffness value of this particular material.

In conclusion, based on the three different examples in Simulation 3, we can observe that the pressure and displacement are influenced by the distinct layers within the system. In the first example, we observed that fluid escaped into fractures that intersected the net pay, which had higher permeability than the two other layers. Additionally, the displacement was affected by the material with the lowest stiffness, resulting in fractures opening within the net pay.

In the second example we noticed that higher normal permeability in the fractures allowed fluid to escape more easily into the outer material, resulting in an increased pressure. Combined with the boundary conditions this led to the opening of the fractures in the upper-left region. In the last example, we observed that the material's stiffness had minimal impact on the pressure distribution, while permeability exhibited a strong influence. Furthermore, we discussed how the opening of fractures was not solely dependent on a material's stiffness, but also affected by the pressure within the medium.

Chapter 8

Summary

In this thesis, we have presented research that developed and analysed a coupled MSMFE-MFMFE method for the Biot system of poroelasticity in the reservoir matrix, along with a MFMFE method for the fracture flow. We began by providing a brief introduction to the theory of flow in porous media, including properties of the medium and fluid, Darcy's law, and conservation of mass, before defining a fracture in the medium. Introduction to theory of the finite element method and the mixed finite element method were given in Chapter 2. A short introduction to the MPFA and MPSA finite volume methods were given at the end of Chapter 2 as the MFMFE and MSMFE methods are closely related to the MPFA and MPSA methods, respectively. Chapter 3 focused on the different model equations used in our fracture domain and presented the strong form of our problem.

In our research we studied the mixed variational formulation of our strong problem outlined in Problem 1. Chapter 4 began by giving an introduction of the notation and spaces used during the analysis. The test functions were introduced, the variational formulation derived, and the different functional spaces were stated. At the end of the chapter we presented a stability analysis for the mixed variational formulation, resulting in the continuous problem being stable.

In Chapter 5, we presented the semi-discrete scheme, which is based on the mixed finite element method for elasticity and Darcy flow, coupled with a mixed finite element method for the flow within the fracture. In the reservoir matrix we employed the lowest order Brezzi-Douglas-Marini spaces for both the stress and the Darcy flow. We utilized piecewise constant displacement, rotation, and pressure within the reservoir matrix. In the fracture, we ensured that the element spaces for fracture pressure and the flux were compatible pairs. We proved both existence and uniqueness of the semi-discrete scheme and presented a stability analysis, which indicated that the semi-discrete scheme was stable.

Chapter 6 presented the fully-discrete scheme, which is based on the backward Euler in time method. We provided a brief introduction to the backward Euler method before introducing the fully-discrete scheme. Additionally, we presented the results of an existence and uniqueness analysis that demonstrated that a unique solution exists for the fully-discrete scheme.

In the final chapter, Chapter 7, we presented code verification and performed three distinct simulations. We conducted a study to analyze the influence of fractures and different parameter values on pressure distribution and displacement. Example 3.2 demonstrated that equal normal and tangential permeability resulted in a greater fluid escape into the outer layers compared to Example 3.1. This resulted in higher pressure in the outer layers and subsequently caused openings in the fractures. Furthermore, the final example, Example 3.3, examined how the openings of the fractures were not only influenced by the material stiffness, but also affected by the pressure within the medium.

8.1 Future work

In future studies, it would be valuable to conduct an error analysis of our method and compare the results with those obtained in Section 7.1. In addition, for the fully-discrete method, it would be interesting to investigate whether the algebraic system at each time step can be reduced to a positive-definite cell-centered system. This will demonstrate the increased efficiency of the method compared to traditional MFE methods, as reducing the fully-mixed method to a positive-definite cell-centered system will decrease the computational cost.

Moreover, several assumptions were made throughout this research, including the inf-sup conditions for the pressure, displacement, and rotation within the reservoir matrix, as well as the bound for the mortar displacement. Performing an analysis without these assumptions and with different bounds could provide valuable insights into their impact on the results. Furthermore, this study neglected gravity and friction, and exploring the effects of these forces in future work could be valuable. So far, this thesis has focused primarily on spatial discretization, with a simple temporal discretization. However, it would be interesting to expand the study and incorporate more advanced temporal discretization techniques, such as space-time discretization using multi-rate schemes. These schemes involve employing different time steps for different physics, specifically for flow and mechanics.

In the research the robustness of our method with respect to the model parameters has not been verified. For instance, we have not examined the behavior of our method in the incompressible limits, such as when the first Lamé parameter λ tends towards infinity or when the storage coefficient c_0 approaches zero. Additionally, our current approach assumes fractures to be static geometric objects, and we have not explored the extension of our method to cases where fractures are growing.

Within the larger framework of thermal-hydraulic-chemical (THC) processes, this research focuses on the coupling of hydro and mechanic problems, while the thermal and chemical aspects have not been investigated. Within the hydro-mechanic coupling framework, we have utilized a simplified interface condition by assuming equal pressures. However, a more comprehensive treatment of interface conditions, as demonstrated in [Martin et al., 2005b] and [Berre et al., 2019], should be incorporated. This can be achieved through minor modifications of the exercises conducted in this thesis, as the key factors in both models are the coercivity and continuity of the bilinear form. The incorporation of thermal and chemical processes presents additional challenges, as the model equations are expected to become inherently nonlinear. However, in the simplified scenario of linear models, we expect the same arguments or procedures to hold.

Bibliography

[Aarnes et al., 2007] Aarnes, J. E., Gimse, T., and Lie, K. (2007). *An Introduction to the Numerics of Flow in Porous Media using Matlab*, pages 265–306. Springer Berlin Heidelberg, Berlin, Heidelberg.

[Aavatsmark, 2002] Aavatsmark, I. (2002). An introduction to multipoint flux approximations for quadrilateral grids. *Computational Geosciences*, 6.

[Adams and Fournier, 2003] Adams, R. and Fournier, J. (2003). *Sobolev spaces*. Pure and Applied Mathematics. Academic Press, 2 edition.

[Ahrens et al., 2005] Ahrens, J., Geveci, B., and Law, C. (2005). Paraview: An end-user tool for large data visualization. *Visualization Handbook*.

[Almani and Kumar, 2022] Almani, T. and Kumar, K. (2022). Convergence of single rate and multirate undrained split iterative schemes for a fractured biot model. *Computational Geosciences*, 26(4):975–994.

[Almani et al., 2016] Almani, T., Kumar, K., Dogru, A., Singh, G., and Wheeler, M. (2016). Convergence analysis of multirate fixed-stress split iterative schemes for coupling flow with geomechanics. 311:180–207.

[Almani et al., 2021] Almani, T., Kumar, K., and Manea, A. (2021). On the convergence of flow and mechanics iterative coupling schemes in fractured heterogeneous poro-elastic media. In *Numerical mathematics and advanced applications—ENUMATH 2019*, volume 139 of *Lecture Notes Computational Science and Engineering.*, pages 53–62. Springer, Cham.

[Almani et al., 2019] Almani, T., Kumar, K., Singh, G., and Wheeler, M. (2019). Stability of multirate explicit coupling of geomechanics with flow in a poroelastic medium. *Computers and Mathematics with Applications*, 78(8):2682–2699.

[Almani et al., 2017] Almani, T., Kumar, K., and Wheeler, M. (2017). Convergence and error analysis of fully discrete iterative coupling schemes for coupling flow with geomechanics. *Computational Geosciences*, 21(5-6):1157–1172.

[Almani et al., 2020] Almani, T., Manea, A., Kumar, K., and Dogru, A. (2020). Convergence of the undrained split iterative scheme for coupling flow with geomechanics in heterogeneous poroelastic media. *Computational Geosciences*, 24(2):551–569.

[Ambartsumyan et al., 2020a] Ambartsumyan, I., Khattatov, E., Nordbotten, J. M., and Yotov, I. (2020a). A multipoint stress mixed finite element method for elasticity on simplicial grids. *SIAM Journal on Numerical Analysis*, 58(1):630–656.

[Ambartsumyan et al., 2021] Ambartsumyan, I., Khattatov, E., Nordbotten, J. M., and Yotov, I. (2021). A multipoint stress mixed finite element method for elasticity on quadrilateral grids. *Numerical Methods for Partial Differential Equations*, 37(3):1886–1915.

[Ambartsumyan et al., 2020b] Ambartsumyan, I., Khattatov, E., and Yotov, I. (2020b). A coupled multipoint stress–multipoint flux mixed finite element method for the biot system of poroelasticity. *Computer Methods in Applied Mechanics and Engineering*, 372:113407.

[Arrarás and Portero, 2019] Arrarás, A. and Portero, L. (2019). Multipoint flux mixed finite element methods for slightly compressible flow in porous media. *Computers & Mathematics with Applications*, 77(6):1437–1452. 7th International Conference on Advanced Computational Methods in Engineering (ACOMEN 2017).

[Atkinson et al., 2009] Atkinson, K., Han, W., and Stewart, D. (2009). *Numerical solution of ordinary differential equations.* JohnWiley & Sons.

[Bear, 1988] Bear, J. (1988). *Dynamics of fluids in porous media.* Dover Publications.

[Berre et al., 2019] Berre, I., Doster, F., and Keilegavlen, E. (2019). Flow in fractured porous media: A review of conceptual models and discretization approaches. *Transport in Porous Media*, 130:215–236.

[Biot, 1972] Biot, M. (1972). Theory of finite deformations of pourous solids. *Indiana University Mathematics Journal*, 21:597–620.

[Biot, 1941] Biot, M. A. (1941). General theory of three-dimensional consolidation. *Journal of Applied Physics*, 12:155–164.

[Birkholzer et al., 2009] Birkholzer, J., Zhou, Q., and Tsang, C. (2009). Large-scale impact of co2 storage in deep saline aquifers: A sensitivity study on pressure response in stratified systems. *International journal of greenhouse gas control*, 3:181–194.

[Borregales et al., 2019] Borregales, M., Kumar, K., Radu, F., Rodrigo, C., and Gaspar, F. (2019). A partially parallel-in-time fixed-stress splitting method for biots consolidation model. *Computers & Mathematics with Applications*, 77:1466–1478.

[Both et al., 2022] Both, J., Barnafi, N., Radu, F., Zunino, P., and Quarteroni, A. (2022). Iterative splitting schemes for a soft material poromechanics model. *Computational Methods in Applied Mechanicws Engineering*, 388:Paper No. 114183, 29.

[Both et al., 2019a] Both, J., Kumar, K., Nordbotten, J., and Radu, F. (2019a). Anderson accelerated fixed-stress splitting schemes for consolidation of unsaturated porous media. *Computers & Mathematics with Applications*, 77:1479–1502.

[Both et al., 2019b] Both, J., Kumar, K., Nordbotten, J., and Radu, F. (2019b). The gradient flow structures of thermo-poro-visco-elastic processes in porous media.

[Brenan et al., 1987] Brenan, K. E., Campbell, S. L., and Petzold, L. R. (1987). *Numerical Solution of Initial-Value Problems in Differential-Algebraic Equations*. Classics in Applied Mathematics. Society for Industrial Mathematics, 2 edition.

[Brorson, 202] Brorson, S. (202). *Numerically solving ordinary differential equations*. Northeastern University.

[Cappa, 2011] Cappa, F. (2011). Influence of hydromechanical heterogeneities of fault zones on earthquake ruptures. *Geophysical Journal International*, 185:1049–1058.

[Castonguay et al., 2013] Castonguay, S., Mear, M., Dean, R., and Schmidt, J. (2013). Predictions of the growth of multiple interacting hydraulic fractures in three dimensions. *Society of Petroleum Engineers*, pages 1049–1058.

[Cheney, 2001] Cheney, W. (2001). *Analysis for Applied Mathematics*. Springer, New York, 1 edition.

[da Vinci, 1510] da Vinci, L. (1506-1510). *Codex Leicester*.

[de Hoop et al., 2020] de Hoop, M., Kumar, K., and Ye, R. (2020). Analysis of dynamic ruptures generating seismic waves in a self-gravitating planet: an iterative coupling scheme and well-posedness. *Quarterly of Applied Mathematics*, 78:485–511.

[Detournay and Cheng, 1993] Detournay, E. and Cheng, A. (1993). 5 - fundamentals of poroelasticity. In Fairhurst, C., editor, *Analysis and Design Methods*, pages 113–171. Pergamon, Oxford.

[Dieudonné, 1960] Dieudonné, J. (1960). *Foundations of Modern Analysis.* Academic Press, 6 edition.

[Ervik, 2020] Ervik, H. (2020). Simulation of injection-induced deformation for a stimulation experiment at the grimsel underground laboratory. Master's thesis, University of Bergen.

[Formaggia et al., 2014] Formaggia, L., Fumagalli, A., Scotti, A., and Ruffo, P. (2014). A reduced model for darcy's problem in networks of fractures. *ESAIM: Mathematical Modelling and Numerical Analysis*, 48:1089–1116.

[Franceschini et al., 2020] Franceschini, A., Castelletto, N., White, J., and Tchelepi, H. (2020). Algebraically stabilized lagrange multiplier method for frictional contact mechanics with hydraulically active fractures. *Computer Methods in Applied Mechanics and Engineering*, 368:113–161.

[Friedlingstein et al., 2022] Friedlingstein, P., Jones, M., O'Sullivan, M., Andrew, R., Bakker, D., and et al. (2022). Global carbon budget 2021. 14:1917–2005.

[Fumagalli and Scotti, 2013] Fumagalli, A. and Scotti, A. (2013). A numerical method for two-phase flow in fractured porous media with non-matching grids. *Advances in Water Resources*, 62:454–464.

[Gaspar et al., 2003] Gaspar, F., Lisbona, F., and Vabishchevich, P. (2003). A finite difference analysis of biot's consolidation model. *Applied Numerical Mathematics*, 44:487–506.

[Gaspar and Rodrigo, 2017] Gaspar, F. and Rodrigo, C. (2017). On the fixed-stress split scheme as smoother in multigrid methods for coupling flow and geomechanics. *Computer Methods in Applied Mechanics and Engineering*, 326:526–540.

[Girault et al., 2016] Girault, V., Kumar, K., and Wheeler, M. F. (2016). Convergence of iterative coupling of geomechanics with flow in a fractured poroelastic medium. *Computational Geosciences*, 20:997–1011.

[Girault et al., 2015] Girault, V., Wheeler, M. F., Ganis, B., and Mear, M. E. (2015). A lubrication fracture model in a poro-elastic medium. *Mathematical Models and Methods in Applied Sciences*, 25(4):587–645.

[Girault et al., 2018] Girault, V., Wheeler, M. F., Kumar, K., and Singh, G. (2018). Mixed formulation of a linearized lubrication fracture model in a poro-elastic medium. *Computational Methods in Applied Sciences*, 47:171–219.

[Hu et al., 2017] Hu, X., Rodrigo, C., Gaspar, F. J., and Zikatanov, L. T. (2017). A nonconforming finite element method for the biot's consolidation model in poroelasticity. *Journal of Computational and Applied Mathematics*, 310:143–154. Numerical Algorithms for Scientific and Engineering Applications.

[Huinink, 2016] Huinink, H. (2016). *Fluids in Porous Media.* 2053-2571. Morgan and Claypool Publishers.

[Jacobsen, 2022] Jacobsen, I. K. (2022). Simulation of 3d hydrothermal circulation and application to faulted oceanic ridge systems. Master's thesis, University of Bergen.

[Jennings et al., 1997] Jennings, W., Mittlefehldt, E., and Stremple, P. (1997). *Analytical Gas Chromatography.* Academic Press, 2 edition.

[Jha and Juanes, 2014] Jha, B. and Juanes, R. (2014). Coupled multiphase flow and poromechanics: A computational model of pore pressure effects on fault slip and earthquake triggering. *Water Resources Research*, 50:3776–3808.

[Keilegavlen et al., 2021] Keilegavlen, E., Berge, R., Fumagalli, A., Starnoni, M., Stefansson, I., Varela, J., and Berre, I. (2021). Porepy: an open-source software for simulation of multiphysics processes in fractured porous media. *Computational Geosciences*, 25:243–265.

[Kim et al., 2011a] Kim, J., Tchelepi, H., and Juanes, R. (2011a). Stability and convergence of sequential methods for coupled flow and geomechanics: drained and undrained splits. *Computer methods in Applied Mechanics and Engineering*, 200:2094–2116.

[Kim et al., 2011b] Kim, J., Tchelepi, H., and Juanes, R. (2011b). Stability and convergence of sequential methods for coupled flow and geomechanics: Fixed-stress and fixed-strain splits. *Computer methods in Applied Mechanics and Engineering*, 200:1591–1606.

[Knabner and Angermann, 2003] Knabner, P. and Angermann, L. (2003). *Numerical Methods for Elliptic and Parabolic Partial Differential Euations.* Springer, New York, 1 edition.

[Kumar et al., 2016] Kumar, K., Almani, T., Singh, G., and Wheeler, M. (2016). Multirate undrained splitting for coupled flow and geomechanics in porous media. In *Numerical mathematics and advanced applications—ENUMATH 2015*, volume 112 of *Lect. Notes Comput. Sci. Eng.*, pages 431–440. Springer, [Cham].

[Kumar et al., 2020] Kumar, K., List, F., Pop, I., and Radu, F. (2020). Formal upscaling and numerical validation of unsaturated flow models in fractured porous media. *Journal of Computational Physics*, 407:109–138.

[List et al., 2020] List, F., Kumar, K., Pop, I., and Radu, F. (2020). Rigorous upscaling of unsaturated flow in fractured porous media. *SIAM journal on mathematical analysis*, 52(1):239–276.

[Martin et al., 2005a] Martin, V., Jaffré, J., and Roberts, J. (2005a). Modeling fractures and barriers as interfaces for flow in porous media. *SIAM Journal on Scientific Computing*, 26:1667–1691.

[Martin et al., 2005b] Martin, V., Jaffré, J., and Roberts, J. E. (2005b). Modeling fractures and barriers as interfaces for flow in porous media. *SIAM Journal on Scientific Computing*, 26(5):1667–1691.

[Mehrabia and Abousleiman, 2014] Mehrabia, A. and Abousleiman, Y. (2014). Generalized biot's theory and mandel's problem of multiple-porosity and multiple-permeability poroelasticity. *Journal of Geophysical Research: Solid Earth*, 119(4):2745–2763.

[Mikelić and Wheeler, 2006] Mikelić, A. and Wheeler, M. (2006). Convergence of iterative coupling for coupled flow and mechanics. *Computer and Geosciences*, 29:455–461.

[Moholt, 2021] Moholt, T. (2021). MPFA methods for Richard's equation. Master's thesis, University of Bergen.

[Murad and Loula, 1992] Murad, M. A. and Loula, A. F. (1992). Improved accuracy in finite element analysis of biot's consolidation problem. *Computer Methods in Applied Mechanics and Engineering*, 95(3):359–382.

[Nilsen et al., 2018] Nilsen, H. M., Nordbotten, J. M., and Raynaud, X. (2018). Comparison between cell-centered and nodal-based discretization schemes for linear elasticity. *Computational Geosciences*, 22.

[Nishiyama and Yokoyama, 2017] Nishiyama, N. and Yokoyama, T. (2017). Permeability of porous media: Roleof the critical pore size. *Journal of Geophysical Research: Solid Earth*, 122:6955–6971.

[NOAA, 2023] NOAA, N. C. F. E. I. (2023). Monthly global climate report for annual 2022.

[Nordbotten and Keilegavlen, 2021] Nordbotten, J. and Keilegavlen, E. (2021). *An Introduction to Multi-point Flux (MPFA) and Stress (MPSA) Finite Volume Methods for Thermo-poroelasticity*, pages 119–158. Springer International Publishing, Cham.

[Nordbotten, 2016] Nordbotten, J. M. (2016). Stable cell-centered finite volume discretization for biot equations. *SIAM Journal on Numerical Analysis*, 54(2):942–968.

[Nordbotten and Celia, 2012] Nordbotten, J. M. and Celia, M. A. (2012). *Geological Storage of CO2: Modeling Approaches for Large-Scale Simulation.* John Wiley & Sons.

[Phillips and Wheeler, 2007] Phillips, P. and Wheeler, M. (2007). A coupling of mixed and continuous galerkin finite element methods for poroelasticity i: The continuous in time case. *Computational Geosciences*, 11:131–144.

[Phillips and Wheeler, 2008] Phillips, P. and Wheeler, M. (2008). A coupling of mixed and discontinuous galerkin finite-element methods for poroelasticity. *Computational Geosciences*, 12:417–435.

[Radu, 2021] Radu, F. A. (2021). Lecture notes in porous media.

[Radu, 2022] Radu, F. A. (2022). Lecture notes in functional analysis.

[Reichenberger et al., 2006] Reichenberger, V., Jakobs, H., Bastian, P., and Helmig, R. (2006). A mixed-dimensional finite volume method for two-phase flow in fractured porous media. *Advances in Water Resources*, 29:1020–1036.

[Settari and Mourits, 1994] Settari, A. and Mourits, F. (1994). Coupling of geomechanics and reservoir simulation models. *Advances in computer methods and geomechanics*, pages 2151–2158.

[Skoglund, 2019] Skoglund, N. (2019). Simulations og Flow and Mechanics in the brain. Master's thesis, University of Bergen.

[Stefansson et al., 2020] Stefansson, I., Keilegavlen, E., Halldórsdóttir, S., and Berre, I. (2020). Numerical modelling of convection-driven cooling, deformation and fracturing of thermo-poroelastic media. *Transport in Porous Media*, 140:371–394.

[Storvik, 2018] Storvik, E. (2018). On the optimization of iterative schemes for solving non-linear and/or coupled PDEs. Master's thesis, University of Bergen.

[Storvik, 2022] Storvik, E. (2022). *Development of robust and efficient solution strategies for coupled problems.* PhD dissertation, University of Bergen.

[Storvik et al., 2021] Storvik, E., Both, J., Nordbotten, J., and Radu, F. (2021). The fixed-stress splitting scheme for Biot's equations as a modified Richardson iteration: implications for optimal convergence. In *Numerical mathematics and advanced applications—ENUMATH 2019*, volume 139 of *Lecture Notes in Computational Science and Engineering*, pages 909–917. Springer, Cham.

[Storvik et al., 2019] Storvik, E., Both, J. W., Kumar, K., Nordbotten, J., and Radu, F. (2019). On the optimization of the fixed-stress splitting for biot's equations. *International Journal for Numerical Methods in Engineering*, 120:179–194.

[Terzaghi and Peck, 1948] Terzaghi, K. and Peck, R. (1948). Soil mechanics. *Engineering Practice.*

[Thomée, 1984] Thomée, V. (1984). *Galerkin Finite Element Methods for Parabolic Problems.* Springer-Verlag.

[Varela et al., 2022] Varela, J., Ahmed, E., Keilegavlen, E., Nordbotten, J. M., and Radu., F. A. (2022). A posteriori error estimates for hierarchical mixed-dimensional elliptic equations. *Journal of Numerical Mathematics*, 0(0).

[Wheeler et al., 2012] Wheeler, M., Xue, G., and Yotov, I. (2012). Accurate Cell-Centered Discretizations for Modeling Multiphase Flow in Porous Media on General Hexahedral and Simplicial Grids. *SPE Journal*, 17(03):779–793.

[Wheeler and Yotov, 2006] Wheeler, M. F. and Yotov, I. (2006). A multipoint flux mixed finite element method. *SIAM Journal on Numerical Analysis*, 44(5):2082–2106.

[White et al., 2016] White, J., Castelletto, N., and Tchelepi, H. (2016). Block-partitioned solvers for coupled poromechanics: A unified framework. *Computer Methods in Applied Mechanics and Engineering*, 303:55–74.

[Ye et al., 2020] Ye, R., Kumar, K., de Hoop, M. V., and Campillo, M. (2020). A multi-rate iterative coupling scheme for simulating dynamic ruptures and seismic waves generation in the prestressed earth. *Journal of Computational Physics*, 405:109098.

[Yi, 2014] Yi, S. (2014). Convergence analysis of a new mixed finite element method for biot's consolidation model. *Numerical Methods for Partial Differential Equations*, 30.

[Yi, 2017] Yi, S. (2017). A study of two modes of locking in poroelasticity. *SIAM Journal on Numerical Analysis*, 55(4):1915–1936.